WASHINGTON UNIVERSITY

Department of Physics

Dissertation Committee:

Willem H. Dickhoff, Chairperson

John W. Clark

Lee G. Sobotka

SELF-CONSISTENT GREEN'S FUNCTIONS IN NUCLEAR MATTER

By

Elizabeth P. Roth

A DISSERTATION PRESENTED TO THE

GRADUATE SCHOOL OF ARTS AND SCIENCES

OF WASHINGTON UNIVERSITY IN

PARTIAL FULFILLMENT OF THE

REQUIREMENTS FOR THE DEGREE

OF DOCTOR OF PHILOSOPHY

September 2000

Saint Louis, Missouri

Acknowledgements

My greatest thanks go to Wim Dickhoff. My exploration of this topic has been achieved with his guidance along a long series of small steps. For his intuition, patience and support, I am especially grateful. I have valued the opportunities he has supplied me in collaborations and conferences which have provided a doorway into the professional community with confidence and excitement. I would also like to extend my thanks to Lee Sobotka, John Clark, and Demetrios Sarantites for the questions and encouragements they offered me while serving as my committee during this work.

I would also like to thank my department for the community and friendship it has offered. The company of faculty, staff, and fellow graduate students has made my days especially pleasant.

I am very grateful to Angels Ramos and Arturo Polls for their hospitality during my enlightening and fruitful visits to their beautiful city of Barcelona. I also owe much gratitude to Arne Schnell for his collaboration in the finite-temperature study.

To my family, I thank you for your endless emotional support, generosity, and laughter. I thank my Uncle Jack for inspiring my interest in physics with a single word: Why?

And finally, I can not thank Dean enough. To me, his computer administration has been helpful, but his company has been invaluable.

Contents

List of Tables

List of Figures

Chapter 1

Introduction

1.1 Motivation

The microscopic derivation of properties of nuclei remains a compelling goal of quantum many-body theory. Which many-body method to use and which interaction to use therein are questions that are still actively pursued. For the purpose of deciding these basic features of the microscopic calculation, a proving ground which separates the chosen method or interaction from each other is necessary. In this regard, the opportunity to isolate the nuclear force from the many-body calculation scheme is provided by considering infinite nuclear matter [1].

Some properties of heavy nuclei saturate to A-independent quantities. For instance, in this large-A limit, neglecting Coulomb forces and assuming equal numbers of protons and neutrons, the only remaining term in the semiempirical mass formula [2],[3] requires a binding energy of about 16 MeV per nucleon. Also, the central density in large nuclei saturates at a value of about 0.17 fm^{-3} [3]. A more modern value obtained from electron scattering experiments on ^{208}Pb is 0.16 fm^{-3} [4]. For large-A systems, these saturation properties prove to be good tests for many-body methods and theoretical models of the nuclear interaction. The hypothetical system of infinite nuclear matter is then defined by taking $A \Rightarrow \infty$, neglecting Coulomb forces, and setting the number of protons equal to that of neutrons. This choice suggests that the appropriate single-particle (sp) states are plane waves due to translational invariance, whereas for finite nuclei, the choice of sp basis must be addressed separately for each nucleus.

Clearly, solving for a many-body wavefunction of a system containing an infinite

number of particles is impossible. It is useful to recall that all information in a sp wavefunction is contained in a propagator, and all sp information about a system of particles can be contained in the behavior of an "average" single particle [5], or, technically, the single-particle Green's function or propagator. To determine this critical function, approaches are generally based on the notion that atomic nuclei and nuclear matter can be modeled as a non-relativistic system of fermions which interact via two-body forces determined by nuclear scattering experiments. Several methods exist for solving this system and deriving characteristics of nuclear matter and finite nuclei including variational (correlated-basis functions) solutions [6], Brueckner theory's hole-line expansion [7]-[10], and exp S methods [11]. None have had success at this level of approximation in predicting both the binding energy and density simultaneously, and the results of the variational and Brueckner two-hole-line methods were seen to produce differing results, with variational calculations predicting more binding at saturation than the Brueckner scheme in lowest order (Brueckner-Hartree-Fock). This discrepancy called attention to two distinct issues to be addressed by nuclear many-body theory [12].

Firstly, at issue is which is the best method for calculation of saturation properties with this model of the nucleus. The Brueckner-Bethe-Goldstone (BBG) method is an expansion in the number of hole-lines. In lowest order, including two hole-line terms, the results lay on a band in the binding energy vs. density plane known as the Coester band [13]. For a chosen nucleon-nucleon (NN) potential, a calculated saturation density that agrees with the empirical value will have a binding energy (BE) which is too low, and when the correct BE is predicted, the calculated saturation density is too high. The BBG method could be extended to next order in the hole-line expansion to three-hole-line terms. This inclusion offered improvement over the two-hole-line calculation shifting saturation energy per particle from -10 MeV to near -16 MeV and saturation density to a range of Fermi momenta from 1.45 fm^{-1} to over 1.50 fm^{-1} for the Reid soft-core interaction [14]. While this did not bring saturation properties to agree with the empirical values, it did move results off the Coester

band and agreed with advanced variational calculations [15]. The fact that results calculated with two different methods agreed did appear to resolve the conflict of method within the field to a degree. However, both methods produced results which could not describe nuclear saturation properties.

Secondly, at issue is which are the most important physical aspects of the system that must be included in any accurate calculation of its saturation properties. In an attempt to understand saturation values, the possibility that three-body interactions may play an important role was explored using a phenomenological three-body force in nuclear matter to yield a theoretical description of the known nuclear saturation [16]. Meanwhile, Dirac-Brueckner theory was developed to extend the model to include possible relativistic effects [17],[18], and this also yielded a satisfactory agreement with empirical saturation properties. These saturation values for various potentials lay on a new band in the BE vs. density plane which included the empirical value, and the extension of the calculation beyond two-body correlations need not be considered. This perplexing and contradictory state of affairs continues to fuel many-body theory's pursuit of an understanding of nuclear saturation. In the case of the spin-orbit splitting in ^{16}O, it is possible to argue that relativity and three-body forces may be different ways of describing the same physics [19].

The results of BHF calculations depend on the choice of the sp potential, $U(k)$. In the "standard" choice, $U = 0$ for $k > k_F$, and U is the self-consistent Brueckner-Hartree-Fock potential for $k < k_F$. The alternative "continuous" choice has been proposed in Ref. [20] for which U is again the self-consistent BHF potential, but it extends to $k > k_F$. BBG calculations are in principle independent of the choice of U. Including the three hole-line contribution, using both choices of U as a starting point, Ref. [21] has recently demonstrated this independence. This is due to the fact that the three hole-line contribution for the continuous potential is much smaller than that with the standard choice which implies that a BHF calculation with the continuous U may already include higher-order correlations [22].

The present approximation to the propagator in infinite nuclear matter yields a

set of Feynman diagrams well suited to considering short-range correlations (SRC) which are studied in this thesis. However, a realistic NN interaction contains not only short-range repulsion, but also longer range forces which are more attractive. Calculations which include the diagrams for long-range correlations (LRC) suggest that the Δ-isobar excitations can not be neglected in calculating the contribution of these diagrams to binding [23]. The resulting contribution to the binding energy (calculated in the independent-particle model) is unreasonably high. These considerations also lead to the prediction of pion condensation which is not observed in nuclei. The relevance of these terms in describing finite nuclei is questionable, due to the q-dependence of the potential and the fact that nucleon wavefunctions in finite nuclei will sample both repulsive and attractive regions, whereas, in nuclear matter, the attractive part can be amplified at $q \sim k_F$ due to momentum conservation. For the purpose of describing nuclear matter as an approximation to the interior of heavy nuclei, the study of LRC will not be attempted in the present work.

It is in this context that one may consider the issue which is the object of this work: To what extent can nuclear saturation be understood taking the nuclear medium as a nonrelativistic, low-density system of particles interacting via a realistic two-body NN interaction? The calculations of the type discussed above employ an independent-particle model (IPM) which assumes that sp states of a given momentum have a sp energy determined by a momentum-dependent mean field due to the presence of the nuclear medium. Before considering three-body forces or relativity, one may observe that these calculations have thus far not been performed including SRC self-consistently. For example, Brueckner methods have been used to calculate the effect of interactions using as a starting point a system of noninteracting, independent particles in a mean field such that all states with $k < k_F$ are fully occupied and all those with $k > k_F$ are empty. Meanwhile, experiment has shown that the $3s_{1/2}$ orbital of ^{208}Pb is only 75% occupied [24], a feature which can not be explained using an IPM. A realistic nuclear interaction contains strong short-range repulsion, which necessarily implies that interacting nucleons can admix high-momentum states

according to the Heisenberg uncertainty principle. In order for a calculation to include effects of SRC, it must allow particles to exist off the mass shell [25], and must go beyond the mean-field IPM. To what extent one can understand nuclear saturation utilizing the chosen basic physical model of the nuclear medium, while investing added complexity to the computational method to include SRC beyond the IPM, has not been fully determined. The difficulty in pursuing this method is the computational expense and difficulty of its implementation with iterative methods.

In this thesis, the nuclear medium is considered as a nonrelativistic, low-density Fermi gas of nucleons at zero-temperature in which interactions are very repulsive at short-range. In this limit, the Brueckner G-matrix approximation has been used to describe the effective interaction in the IPM with only forward going propagators included in the calculation of the effective interaction. This is not the approximation we will use, however, since the corresponding input spectral functions in this approximation are δ-functions on mass-shell and the outputs are continuous spectral functions in energy, fragmenting the strength of a particle with a fixed momentum over all energies and depleting its occupation. Thus, the resulting sp states are partially occupied. A particle can be added in sp states that had been considered fully occupied and inaccessible due to Pauli blocking in the IPM ($k < k_F$), and a particle can be removed from an sp state that had been considered empty ($k > k_F$). Thus, the need arises to treat hh and pp propagation in the effective interaction on equal footing [26],[27], as is done with the Galitskii-Feynman effective interaction. Coupling this with the Dyson equation creates a nonlinear iteration scheme which will serve as the basis of self-consistent Green's function (SCGF) studied in nuclear matter. In the present work, computational tools have been generated to perform this calculation, allowing one to assess to what degree such a treatment explains the discrepancy between theoretical and experimental saturation properties

The solution of the considered scheme contains an inherent nonlinearity. This is because the motion of a particle in the interacting medium must be a function of the

motion of all the other particles with which it interacts. As a result, the medium-modified sp propagator is dependent on itself. To solve this problem, the in-medium sp propagator must be expressed as a function of the interaction and the in-medium sp propagator which allows an iterative solution. This nonlinearity is conveniently contained in the SCGF method as the effective potential determines the propagator in medium and the sp propagator is required to calculate the effective interaction. Since a full solution of this problem can only be found by iteration of these quantities, the question addressed by solving for the SCGF is: To what degree does the full solution differs from previous work starting with the IPM approximation?

Treating the nonlinearity on the Hartree-Fock level results in a self-consistent mean field (MF) due to the average effect of the presence of the medium. This yields the shell model (SM) which has had many successes. But this picture cannot contain the observed effects of the more complicated structure of the nuclear force. The structure of sp states in nuclei have been elucidated by (e,e′p) knockout experiments [28],[29]. Investigated states exhibit greater width of the spectral peak for states farther from the Fermi energy, such that the sp states are not localized in energy and therefore do not have infinite lifetimes as in the IPM. These observed peaks are also depleted such that they contain significantly less than all the sp strength. A description of sp states which goes beyond the MF to contain effects of the strong interaction is the Landau-Fermi-liquid description for an infinite system [30]-[33]. Single-particle states in the Fermi-liquid picture will have a finite width around an on-shell quasiparticle energy, and the width increases for states farther from the Fermi surface, as observed in experimental spectra. Another characteristic of sp states inferred from theoretical calculations include a strongly fragmented background which appears far from a quasiparticle peak [26],[34]-[36].

The difficulty in calculating the effect of SRC is that one cannot start from an approximation like the SM and apply the interaction as a perturbation, since the contribution of the short-range interaction diverges at every order. Only an infinite sum can be used as was formulated by Brueckner. Brueckner's G-matrix generates an

imaginary self-energy at energies greater than the Fermi energy but does not generate fragmentation of the sp strength below the Fermi energy. It is therefore necessary to include hole-hole propagation as in the Galitskii-Feynman interaction which leads to a complex self-energy both above and below the Fermi energy. This feature allows for fragmentation of the sp strength both above and below the Fermi energy. A self-consistent determination of the propagator guarantees conservation of particle number [37].

The present work builds on the work of previous efforts [38]-[43], striving to achieve a self-consistent solution. Due to the fact that the key ingredients in a Brueckner-type infinite sum are the propagators and the interaction, the SCGF framework is well suited to the task as it has the key quantity of the sp Green's function, or propagator. The treatment of hole-hole propagation in nuclear matter, which allows the calculation of spectral functions with a semi-realistic interaction, was developed by Ramos [26],[38]. This work was extended to include the full Reid potential including the treatment of pairing instabilities by Vonderfecht [39],[40]. Gearhart followed by considering the parametrization of the spectral function and calculated the scattering of dressed particles in nuclear matter [41],[42],[43]. In the present work, the spectral functions generated by Vonderfecht are used as an ansatz for the single-particle propagator. A functional form of the self-energy has been used, from which the spectral function can be simply obtained. The choice to parametrize the imaginary part of the self-energy is numerically easier to handle than Gearhart's parametrization of the sp spectral function. This method of obtaining the spectral function has the built-in feature of fulfilling the sp strength sum rule and energy weighted sum exactly[44].

In this way, the full propagator is used at every step of the calculation, and the iteration is converged when the output of including the effect of the interacting medium in the sp propagator, with the effective interaction, results in little change according to criteria discussed in Chapter 3. The goal of the SCGF solution is to determine numerically reliable spectral functions which can be used to evaluate the expectation value of any one-body operator and can be used for comparison with

(e,e′p) knockout experiments. While it will not be explored in detail in this thesis, the interacting two-particle propagator is also calculated in this scheme, from which all 2p expectation values can be obtained and which can be used in comparison with (e,e′2p) experiments [45]. The foremost goal of this work is to study the saturation properties of nuclear matter and to explore the properties of the sp SCGF to gain further insight.

The change in treatment of SRC with SCGF provides a mechanism for the sp properties to move away from their IPM values by propagating particles with respect to the correlated ground state [46]. This is the case since the primary effect of self-consistency is the loss of a lower limit in energy for the spectral function. Since the binding energy is found from the sp spectral function by integrating over all phase space the hole spectral function weighted with $(\omega + \frac{k^2}{2m})$, one may wonder whether this might be expected to increase binding significantly. Still, at high momenta ($k >$ 7 fm^{-1}), the hole spectral function consists of a well-defined 2h1p peak at $\omega \cong -\frac{k^2}{2m}$. These high momenta therefore do not contribute to the binding energy resulting in finite and physically reasonable results.

The density dependence of SCGF solutions must be explored in order to define the saturation density predicted by such considerations. Because each density requires iteration to convergence, only two densities are considered, the empirical density (ρ_0), corresponding to $k_F = 1.36$ fm^{-1}, and a slightly higher density corresponding to $k_F = 1.45$ fm^{-1}.

As an additional application of the method developed, finite temperature nuclear matter is studied at $T = 5$ MeV. The same ansatz is used as in the zero temperature case. Some modification of the SCGF framework is required to describe the finite-temperature statistical ensemble of states which uses Matsubara Green's functions [47],[48], but a satisfactory result for $\rho = \rho_0$ is achieved. This method can be applied to determine thermodynamic properties of nuclear matter when short-range correlations dominate.

In this work, the Reid potential [49] is used since it contains a very strong repulsive

core. This implies that the more recent, softer potentials will also be amenable to a SCGF solution once one has solved the technical issues encountered in implementing the SCGF solution for the Reid potential.

1.2 Outline

In Chapter 2, the formal framework of the solution for SCGFs including SRC via the Galitskii-Feynman effective interaction is introduced. The propagator is introduced, and its expansion as an infinite set of Feynman diagrams is developed. The form of the effective interaction for the low-density limit is the gamma matrix which contains the effect of SRC in a sum of all ladder diagrams. This effective interaction will include dressed interacting nucleons and both the particle-particle (pp) and the hole-hole (hh) terms in the ladder equation. Then the self-energy is constructed from the gamma matrix and sp propagator, both of which contain medium modifications. Finally, the Dyson equation is used to yield propagators in terms of the self-energy, or effective potential, with the nonlinearity of the solution again evident.

In Chapter 3, the computational tools used in our calculations are presented. A functional form for the imaginary part of the self-energy is presented and employed. The real part of the self-energy is determined using a dispersion relation, and the Hartree-Fock term is obtained directly from the potential and the momentum distribution. Next the gamma matrix is found by a matrix inversion, and the imaginary part of the self-energy is found from a convolution of the effective interaction and the sp spectral function. The imaginary part of the new self-energy is represented in a functional form whose parameters can be monitored for convergence. The process of iteration to convergence is displayed in Chapter 4, and the key quantities are outlined in their final forms.

In Chapter 5, the SCGF formalism is redeveloped using Matsubara Green's functions for the finite temperature case with results presented in Chapter 6. Finally, some conclusions and future directions are discussed in Chapter 7.

Chapter 2

Zero-Temperature Formalism

The self-consistent treatment of a system of identical interacting fermions is introduced in this chapter. The present formulation is geared toward the study of infinite nuclear matter. A more general and complete introduction to second quantization and many-body methods can be found in Refs. [50]-[54]. Sections 2.1 and 2.2 provide an introduction to the sp propagator and its particular efficacy for describing a many-body system. In Section 2.3, the sp propagator is related to the self-energy, which contains the effect of interparticle interactions, through the Dyson equation. As the approximation of the self-energy in nuclear matter, which includes the influence of SRC, the ladder approximation is introduced in Section 2.4. The resulting set of equations yield a cyclic set of relations requiring a nonlinear solution scheme, as discussed in Section 2.5.

2.1 Background

The meaning of the sp propagator in many-body applications is similar to that in one-particle wave mechanics. In the latter case, for a time-independent Hamiltonian, the time evolution of the wave function is determined as follows (setting $\hbar = 1$)

$$\begin{aligned} \langle \mathbf{r}|\alpha, t_0; t\rangle &= \langle \mathbf{r}|\, U(t-t_0)\, |\alpha, t_0\rangle \\ &= \langle \mathbf{r}|\, e^{-iH(t-t_0)}\, |\alpha, t_0\rangle \\ &= \int d^3r'\ \langle \mathbf{r}|\, e^{-iH(t-t_0)}\, |\mathbf{r}'\rangle \langle \mathbf{r}'|\alpha, t_0\rangle \qquad\qquad t > t_0. \end{aligned} \tag{2.1}$$

where the initial state at t_0 is represented by $|\alpha, t_0\rangle$, and $U(t-t_0)$ represents the time-evolution operator. This result can be rewritten as:

$$\psi(\mathbf{r},t) = i\int d^3r'\; g(\mathbf{r},\mathbf{r}';t-t_0)\psi(\mathbf{r}',t_0) \tag{2.2}$$

showing that the time-evolved state is completely determined by the initial state and the Green's function, g. The propagator can be expressed as:

$$\begin{aligned} g(\mathbf{r},\mathbf{r}';t-t_0) &= -i\left\langle \mathbf{r}\right| e^{-iH(t-t_0)}\left|\mathbf{r}'\right\rangle \\ &= -i\sum_n \langle \mathbf{r}\left|n\right\rangle \left\langle n\right|\mathbf{r}'\rangle\, e^{-iE_n(t-t_0)}. \end{aligned} \tag{2.3}$$

The propagator can be interpreted as the wavefunction at $(\mathbf{r},t)$ of a time evolved state which had been localized at $\mathbf{r}'$ at some initial time t_0. To express this important object, one must recall that the wave function above obeys the Schrödinger wave equation,

$$\begin{aligned} -i\left\langle \mathbf{r}\right| H\left|\Psi(t)\right\rangle &= \frac{\partial}{\partial t}\left\langle \mathbf{r}\right|\Psi(t)\rangle \\ &= \frac{\partial}{\partial t}\left\langle \mathbf{r}\right| U(t-t_0)\left|\Psi(t_0)\right\rangle \\ &= i\int d^3r'\;\frac{\partial}{\partial t} g(\mathbf{r},\mathbf{r}';t-t_0)\left\langle \mathbf{r}'\right|\Psi(t_0)\rangle \end{aligned} \tag{2.4}$$

This differential equation for the time evolution operator is the starting point of its perturbation series, or Born expansion. Likewise, the differential equation for the sp propagator in the many-body problem serves as the source of the Dyson series.

In this chapter the general definition and relations of Green's function theory will be sketched and tailored to infinite nuclear matter. In infinite nuclear matter, translational and rotational invariance dictate the choice of sp basis states to be used. For an infinite medium, the discrete momentum spectrum merges to a continuum with excitation energies becoming continuous, allowing integral and analytic tools to be applied. The many-body methods introduced here are applied to the infinite nuclear matter system by taking advantage of these properties where possible.

2.2 The Single-Particle Propagator in a Many-Body System

For many-particle systems, the propagator will necessarily be a more complicated object than it is for the one-body system, but the same physical interpretations apply. The propagator relates many-body states, and its definition requires the tools of second quantization. The many-body environment requires consideration not only of states where a particle is added to the initial many-body state but also of states where a particle is removed. The propagator therefore contains two terms.

$$\begin{aligned} g(\mathbf{k},\mathbf{k}';t-t_0) &= -i\left\langle \Psi_0^N \right| a_{\mathbf{k}}(t) a^\dagger_{\mathbf{k}'}(t_0) \left| \Psi_0^N \right\rangle \theta(t-t_0) \\ &+ i\left\langle \Psi_0^N \right| a^\dagger_{\mathbf{k}'}(t_0) a_{\mathbf{k}}(t) \left| \Psi_0^N \right\rangle \theta(t_0-t) \end{aligned} \tag{2.5}$$

For notational simplicity in this expression, $\mathbf{k}$ represents momentum as well as spin and isospin quantum numbers. The first term describes the transition amplitude in the $(N+1)$-particle system, from a state which can be described as the N-particle ground state with a particle added in the $\mathbf{k}'$ state, into a final state which can be described as the N-particle ground state with an additional particle in the state $\mathbf{k}$ some time $(t-t_0)$ later. This term can clearly be interpreted as a particle propagating on top of the N-particle ground state and describes the corresponding sp transitions in the many-particle setting. A particle can also first be removed from the system leaving a "bubble" to propagate in the many-body system, and these hole transition amplitudes must also be contained in the sp propagator.

Fourier transforming Eq. (2.5) yields:

$$\begin{aligned} g(\mathbf{k},\mathbf{k}';\omega) &= \left\langle \Psi_0^N \right| a_{\mathbf{k}} \frac{1}{\omega - (\hat{H} - E_0^N) + i\eta} a^\dagger_{\mathbf{k}'} \left| \Psi_0^N \right\rangle \\ &+ \left\langle \Psi_0^N \right| a^\dagger_{\mathbf{k}'} \frac{1}{\omega - (E_0^N - \hat{H}) - i\eta} a_{\mathbf{k}} \left| \Psi_0^N \right\rangle \qquad (2.6) \\ &= \sum_n \frac{\left\langle \Psi_0^N \right| a_{\mathbf{k}} \left| \Psi_n^{N+1} \right\rangle \left\langle \Psi_n^{N+1} \right| a^\dagger_{\mathbf{k}'} \left| \Psi_0^N \right\rangle}{\omega - (E_n^{N+1} - E_0^N) + i\eta} \\ &+ \sum_m \frac{\left\langle \Psi_0^N \right| a^\dagger_{\mathbf{k}'} \left| \Psi_m^{N-1} \right\rangle \left\langle \Psi_m^{N-1} \right| a_{\mathbf{k}} \left| \Psi_0^N \right\rangle}{\omega - (E_0^N - E_m^{N-1}) - i\eta}, \qquad (2.7) \end{aligned}$$

where $\hat{H}$ is the Hamiltonian and E_0^N is its eigenvalue in the ground state. A complete set of states for the $(N+1)$ and $(N-1)$ system has been inserted in the last equality, yielding the Lehmann representation [55] of the sp propagator, g. This representation is especially useful since its poles represent *sp* excitation energies with respect to the ground state. The numerator contains the probability amplitudes to reach these states. The energy required to add a particle to the ground state, $\left|\Psi_0^N\right\rangle$, while reaching the ground state of the $(N+1)$ system, $\left|\Psi_0^{N+1}\right\rangle$, defines the Fermi energy, $\varepsilon_F = E_0^{N+1} - E_0^N$. No particles can be added to the system at an energy less than the Fermi energy. Likewise, a hole state can be created only with energies less than ε_F.

In the infinite nuclear matter system, Eq. (2.7) can be further simplified. Because the ground state of this system has zero total momentum, the addition of a particle with some $\mathbf{k}$ to the ground state also requires the removal of a particle with the same momentum, $\mathbf{k}$. Therefore, in this special case, $\mathbf{k} = \mathbf{k}'$. Dependence on the direction of $\mathbf{k}$ is not possible due to rotational invariance and reflection symmetry. The propagator can finally be written as,

$$g(k,\omega) = \int_{\epsilon_F}^{\infty} d\omega' \frac{S_p(k,\omega')}{\omega - \omega' + i\eta} + \int_{-\infty}^{\epsilon_F} d\omega' \frac{S_h(k,\omega')}{\omega - \omega' - i\eta}, \tag{2.8}$$

where

$$S_p(k,\omega) = \left\langle \Psi_0^N \right| a_{\mathbf{k}} \left| \Psi_n^{N+1} \right\rangle \left\langle \Psi_n^{N+1} \right| a_{\mathbf{k}}^\dagger \left| \Psi_0^N \right\rangle \frac{dn}{d\omega} \tag{2.9}$$

$$S_h(k,\omega) = \left\langle \Psi_0^N \right| a_{\mathbf{k}}^\dagger \left| \Psi_m^{N-1} \right\rangle \left\langle \Psi_m^{N-1} \right| a_{\mathbf{k}} \left| \Psi_0^N \right\rangle \frac{dm}{d\omega} \tag{2.10}$$

are the sp spectral functions which represent the probability of a particle's addition (or removal) at some (k,ω). In this expression, $\frac{dn}{d\omega}$ and $\frac{dm}{d\omega}$ represent the relevant density of states as a function of energy. The denominator in Eq. (2.8) contains the energy of the state reached by adding or removing such a particle. It is important to note that this form of the Green's function is not analytic in either the upper or lower half of the ω-plane. The Green's function contains two contributions, $g^<$ and $g^>$, which are analytic on their respective halves of the ω-plane. Therefore, any required contour integration will be performed on each term separately. The Green's

function has a branch cut along the real axis due to the infinite medium, in which case discrete poles form a continuous line, above the real axis (represented by $>$) for holes and below it ($<$) for particle excitations. In the limiting case of $\omega \to$ real, the propagator can be separated into its real and imaginary parts using the integral relation:

$$\frac{1}{x \pm i\eta} = P\frac{1}{x} \mp i\pi\delta(x) \tag{2.11}$$

where P represents a Cauchy principal value integral. Using Eq. (2.11) in the above form of the Green's function yields

$$\begin{aligned} \text{Im } g(k,\omega) &= -\pi S_p(k,\omega) \qquad\qquad \omega > \epsilon_F \\ &= +\pi S_h(k,\omega) \qquad\qquad \omega < \epsilon_F \qquad (2.12) \\ \text{Re } g(k,\omega) &= P\frac{1}{\pi}\int_{-\infty}^{\epsilon_F} d\omega' \frac{S_h(k,\omega')}{\omega - \omega'} - P\frac{1}{\pi}\int_{\epsilon_F}^{\infty} d\omega' \frac{S_p(k,\omega')}{\omega - \omega'}. \qquad (2.13) \end{aligned}$$

All the information of the sp propagator in infinite nuclear matter is therefore contained in the spectral functions. Knowing how the sp strength with momentum k is distributed in energy therefore yields all relevant information for the sp propagator. The propagator contains crucial information about the sp excitation spectrum in the medium, and we will see that many features of the medium can be determined from this object when evaluating expectation values of relevant operators. Solving for the sp propagator in a many-body system yields sp wave functions in the medium, and any sp information of interest must therefore follow from it.

The expectation value of the kinetic energy can be obtained as follows

$$\langle \hat{T} \rangle = \frac{4V}{(2\pi)^3}\int d^3k \int_{-\infty}^{\varepsilon_F} d\omega \frac{k^2}{2m} S_h(k,\omega) \tag{2.14}$$

where the k index represents momentum, and the factor of four arises from the spin and isospin degeneracy. Since the kinetic energy operator is of one-body type, $\langle \hat{T} \rangle$ is a calculable quantity from the sp propagator. However, if particles interact through a two-body interaction, it would seem that $\langle \hat{V} \rangle$ cannot be found from the sp propagator. Instead, its direct calculation would require the ground state expectation value of

four field operators, which is governed by the two-particle propagator, which will be introduced in the next section. However, the sp propagator is determined through a solution of the Schrödinger equation which includes the potential energy, and, as a result, the potential energy can be obtained from the sp propagator. One can show that [52]

$$\oint \frac{d\omega}{2\pi i}\omega g(k,\omega) = \left\langle \Psi_0^N \right| a_k^\dagger \left[a_k, \hat{H}\right] \left| \Psi_0^N \right\rangle . \tag{2.15}$$

Evaluating the sum of this expression over all *sp* states for the case of a Hamiltonian which is restricted to two-body interactions, one finds:

$$\sum_k \oint \frac{d\omega}{2\pi i}\omega g(k,\omega) = \langle \hat{T} \rangle + 2\langle \hat{V} \rangle \tag{2.16}$$

giving forms of the following expectation values which are dependent only on the single-particle propagator [56],[57]:

$$\langle \hat{T} \rangle = \frac{4V}{(2\pi)^3} \int d^3k \int_{-\infty}^{\varepsilon_F} d\omega S_h(k,\omega) \frac{k^2}{2m} \tag{2.17}$$

$$\langle \hat{V} \rangle = \frac{1}{2}\frac{4V}{(2\pi)^3} \int d^3k \int_{-\infty}^{\varepsilon_F} d\omega S_h(k,\omega)(\omega - \frac{k^2}{2m}) \tag{2.18}$$

$$\langle \hat{H} \rangle = \frac{1}{2}\frac{4V}{(2\pi)^3} \int d^3k \int_{-\infty}^{\varepsilon_F} d\omega S_h(k,\omega)(\omega + \frac{k^2}{2m}) \tag{2.19}$$

The two-particle (2p) propagator allows calculation of expectation values of all two-particle operators for the many-body system. Clearly, for the sake of comparison with experimentally accessible characteristics of nuclei, including saturation properties and $1N$ and $2N$ removal cross sections, the sp and 2p propagators can be considered to contain most information of interest about the system. Therefore, finding the interacting propagators can also be viewed as one of the goals of this microscopic study.

2.3 Dyson Equation

The sp propagator in an interacting medium will be modified with respect to that in free space and take on a much more complicated structure. This modified sp propagator must also describe the particles in the medium with which the single particle

interacts. This results in a nonlinearity which is conveniently treated with SCGF theory. In this section, perturbation theory is applied to the sp propagator to derive its relation to the non-interacting sp propagator and the interparticle interaction.

First, the assumption of only two-body forces yields a Hamiltonian of the following form:

$$\begin{aligned} \hat{H} &= \hat{H}_0 + \hat{H}_1 && (2.20) \\ &= \sum_{\alpha\beta} \langle\alpha| H_0 |\beta\rangle a^\dagger_\alpha a_\beta + \frac{1}{4} \sum_{\alpha\beta\gamma\delta} \langle\alpha\beta| H_1 |\gamma\delta\rangle a^\dagger_\alpha a^\dagger_\beta a_\delta a_\gamma, && (2.21) \end{aligned}$$

using a general sp basis $|\alpha\rangle$, where α describes a complete set of quantum numbers. In the case of nuclear matter, $\hat{H}_1$ represents the Hamiltonian's dependence on two-body operators due to nucleon-nucleon (NN) interactions. The necessary expansion of the sp propagator comes straight from application of t-dependent perturbation theory [52]. Using the differential equation for the time-evolution operator in the interaction picture,

$$i \frac{\partial}{\partial t} U(t, t_0) = \hat{H}_1 U(t, t_0) \tag{2.22}$$

and integrating and iterating, one obtains,

$$\begin{aligned} U(t, t_0) &= 1 - i \int_{t_0}^{t} dt' \hat{H}_1(t') U(t', t_0) \\ &= 1 - i \int_{t_0}^{t} dt_1 \hat{H}_1(t_1) + i^2 \int_{t_0}^{t} dt_1 \int_{t_0}^{t_1} dt_2 \hat{H}_1(t_1) \hat{H}_1(t_2) + \cdots \\ &= \sum_{n=0}^{\infty} \frac{(-i)^n}{n!} \int_{t_0}^{t} dt_1 \cdots \int_{t_0}^{t} dt_n T[\hat{H}_1(t_1) \cdots \hat{H}_1(t_n)] && (2.23) \end{aligned}$$

Noting that $\hat{H}_1(t_1)$ and $\hat{H}_1(t_2)$ may not commute, a general expression for the n^{th} term in this expansion was formulated by Dyson [58] using the time-ordering operator, T. T arranges the operators in brackets such that time arguments decrease from left to right and includes a term of (-1) for each required interchange of two fermion field operators in the ordering. Using this result, one obtains for the propagator in a general sp basis,

$$g(\alpha, \beta; t - t') = -i \sum_{n=0}^{\infty} \int_{-\infty}^{\infty} dt_1 \int_{-\infty}^{\infty} dt_2 \cdots \int_{-\infty}^{\infty} dt_n$$

element from Wick's theorem	factor in Green's function	diagrammatic element
pair of contracted field operators	$ig_0(\alpha,\beta;\omega)$	line with arrow
interaction matrix element	$-i\langle\alpha\beta\|V\|\gamma\delta\rangle$	dashed horizontal line

Table 2.1: Guide to translating Feynman diagrams into mathematical expressions which can be evaluated by integrating over all internal variables.

$$\langle\Phi_0|\, T[\hat{H}_1(t_1)\cdots\hat{H}_1(t_n)a_{\alpha_I}(t)a^\dagger_{\beta_I}(t')]\,|\Phi_0\rangle\,, \tag{2.24}$$

where only the connected contributions need be considered [52]. The field operators are used in the interaction picture as is indicated by the subscript I. Wick's theorem simplifies the expansion and allows each term in the sum to be depicted by a Feynman diagram. It also states that the expectation value of any second quantized operator, like the sp propagator, is represented by the sum over all possible fully contracted products of field operators involved. Performing this sum corresponds to summing all Feynman diagrams which begin and end with free particle noninteracting propagators, whose time dependence is governed by H_0. Each diagram contains a distinct arrangement of n interactions for each order n and contains terms represented in Table 2.1. The contribution of each term represents a probability amplitude as calculated from Eq. (2.24), but now we can associate a picture with each term and use a dictionary to translate from diagrammatical to mathematical expressions, which must be evaluated by integrating over all internal variables. One can also see that all possible diagrams one can assemble with the given elements from a particular term in Eq. (2.24) will correspond to all possible contractions at each order.

Useful expressions can be attained if, instead of the previous sum, one considers the sum of those terms with the external propagators clipped off. The sum defines the reducible self-energy, Σ^R. The sum of only those terms which cannot be separated into two unconnected diagrams by clipping a single propagator yields the proper self-energy, Σ. In this way, the reducible self-energy consists of all orders of the irreducible self-energy connected by noninteracting propagators. This is illustrated in Fig. 2.1.

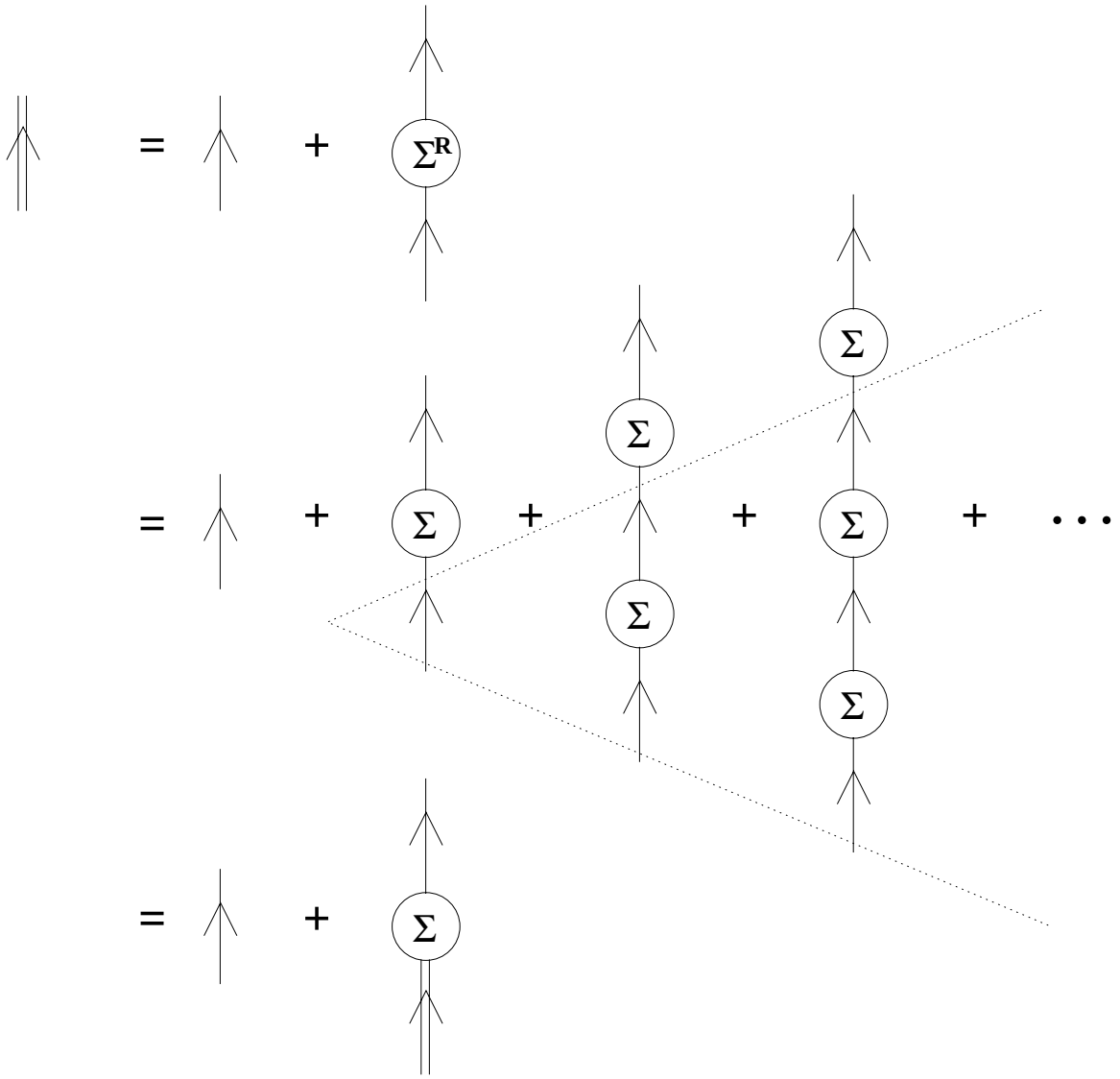

Figure 2.1: Several equivalent forms of Dyson's equation. The last equality allows the solution of the interacting sp propagator from the noninteracting propagator and the effective potential, represented by the irreducible self-energy, Σ.

The last equality in Fig. 2.1 represents Dyson's equation which relates the noninteracting sp propagator and the interacting propagator, represented by double-lines, via the self-energy, Σ. Any approximation for the proper self-energy generates an approximate series of infinite order for the Green's function through Dyson's equation. Choosing an important class of perturbation terms to approximate Σ, one obtains the corresponding sp Green's function from

$$\begin{aligned} g(k,\omega) &= g_0(k,\omega) + g_0(k,\omega)\Sigma(k,\omega)g(k,\omega) \\ &= \frac{1}{g_0(k,\omega)^{-1} - \Sigma(k,\omega)} \\ &= \frac{1}{\omega - \epsilon(k) - \Sigma(k,\omega)}, \end{aligned} \tag{2.25}$$

for the case of nuclear matter. The irreducible self-energy contains the effect of all possible excitations due to the interaction with other particles in the medium, and it acts as a complex, energy-dependent sp potential. Clearly, Σ is the sum of an infinite series characterized by an infinite graphical summation. When this is the case, it can be more convenient to represent the diagrammatic expression in terms of a two-body effective interaction, or vertex function, Γ. The equation of motion of the single-particle propagator relates the sp propagator to the 2p propagator [59],[60]. Likewise, the 2p propagator is related to the 3p propagator, etc.. For two-particle interactions, the differential equation relating the sp and 2p propagators must be considered, and we will assume three-body effects and higher to be negligible.

2.4 The Ladder Approximation

In the present discussion, the problem of microscopically calculating properties of nuclear matter amounts to solving for the generalized effective potential, or proper self-energy, of a particle in the nuclear medium. However, for any such calculation of a self-energy to be implemented, one cannot include all classes of diagrams in the sum. Instead, one must decide which are most important. It is useful to recall that the interaction between two nucleons is quite localized, consisting of a short-range

repulsion (of range, $a \cong .5$ fm) and attraction at slightly larger distance. Therefore, in the case that the interparticle separation (r_0) is much greater than the short-range part of the interaction, $\frac{a}{r_0} \ll 1$, low-density considerations will be of the greatest importance. Considering that the saturation density of nuclear matter is about $\rho \cong .17$ fm^{-3}, corresponding to an interparticle separation of $r_0 \cong 1.8$ fm, we can see that nuclear matter at saturation density can be approximately considered a low density interacting Fermi gas.

One may expect that two-body collisions in a dilute medium will bear some resemblance to two-body scattering in free space, in which case the scattered ($|\psi\rangle$)and free wave functions ($|\phi\rangle$) are related by the Lippmann-Schwinger equation, as follows

$$|\psi\rangle = |\phi\rangle + \frac{1}{E - H_0 + i\eta} V|\psi\rangle. \tag{2.26}$$

Defining a transition matrix, T , such that $V|\psi\rangle = T|\phi\rangle$,

$$V|\psi\rangle = V|\phi\rangle + V\frac{1}{E - H_0 + i\eta} V|\psi\rangle \tag{2.27}$$

$$T|\phi\rangle = V|\phi\rangle + V\frac{1}{E - H_0 + i\eta} T|\phi\rangle \tag{2.28}$$

yields the equation for T in terms of the scattering potential [61]:

$$\begin{aligned} T &= V + V\frac{1}{E - H_0 + i\eta} T \\ &= V + V\frac{1}{E - H_0 + i\eta} V + V\frac{1}{E - H_0 + i\eta} V \frac{1}{E - H_0 + i\eta} V + ... \end{aligned} \tag{2.29}$$

In the last equality, the first term corresponds to a single scattering, the second to double scattering, the third to triple scattering, etc. These multiple scattering terms are the only ones required in describing relative motion of two particles in free space. In the case of interacting nucleons, this series cannot be truncated by only considering terms up to some chosen order, since the hard-core nature of the interaction makes every term divergent. As a result, an infinite sum must be calculated to compute the transition matrix and thereby determine the exact effect of the interaction on a wave function.

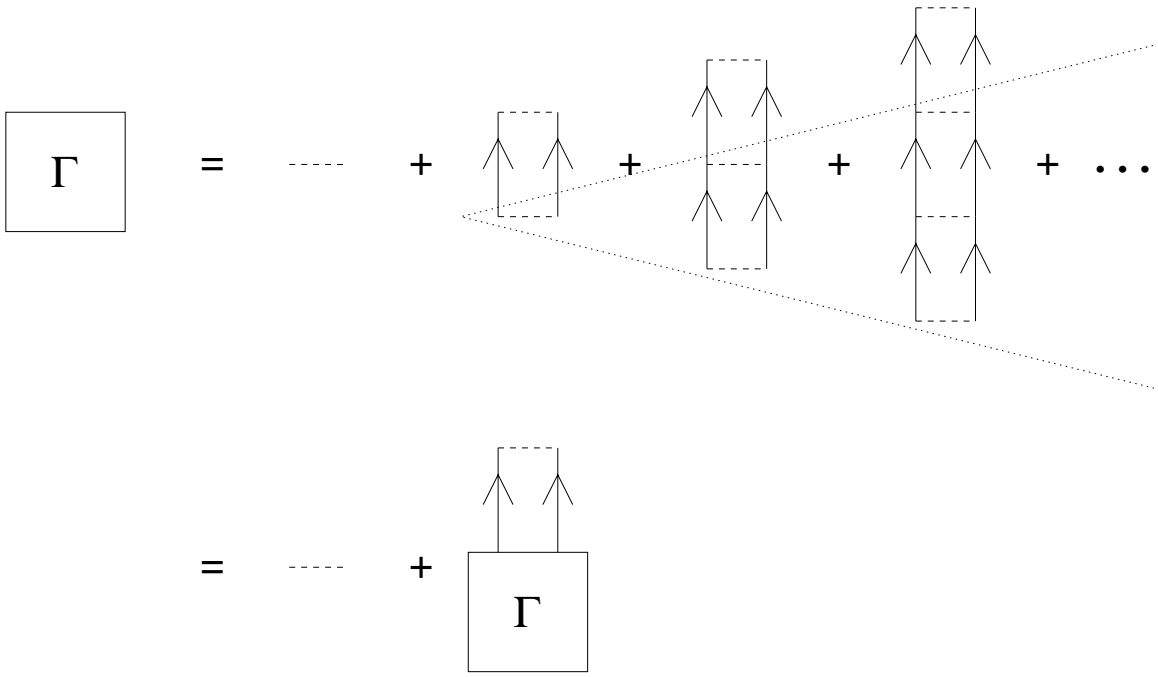

Figure 2.2: Summing ladder diagrams to all orders for the effective interaction, Γ, yields the Bethe-Salpeter equation in the second equality.

This consideration suggests that in the low-density limit, the effective interaction, Γ, will be dominated by two-body scattering to all orders. This implies that all ladder diagrams should be included in any calculation for nuclear matter. In considering the mathematical basis of such an approximation, one observes that the effective interaction contains terms multiplied by a phase space factor of $(\frac{a}{r_0})$ for each event in which a particle and hole interact [62]. All ladder diagrams have such a phase space factor in common. Other diagrams including an additional hole-line contain an extra factor of $(\frac{a}{r_0})$ and can be discarded.

In the Brueckner scheme, only ladder diagrams involving repeated particle-particle scattering are used in the calculation of the effective interaction. Our in-medium approximation for Γ also includes the terms with hole-hole (hh) propagation. The diagrams in Fig. 2.2 represent Feynman diagrams, and not Goldstone diagrams, meaning that time ordering from bottom to top is not implied and all time orderings

are included. This approximation includes the hh scattering terms which are important for particle number conservation. Without hh terms, the imaginary part of the resulting self-energy would have a continuum of values above the Fermi energy and vanish for energies less than the Fermi energy. The inclusion of hh-scattering terms is also mandated by the experimentally observed fragmentation of sp strength in the (e,e′p) reaction. Without an imaginary part of the self-energy below the Fermi energy due to the presence of hh scattering, this fragmentation does not occur.

The sp propagator can be expressed in terms of the 2p propagator. This result can be obtained not only through the manipulation of diagrams in the ladder approximation, but also by considering the time derivative of the sp propagator, written in a general sp basis,

$$\begin{aligned} i\frac{\partial}{\partial t}g(\alpha,\beta,t-t') &= \delta(t-t')\delta_{\alpha\beta} + \epsilon_\alpha g(\alpha,\beta,t-t') \\ &+ \frac{1}{2}\sum_{\eta\gamma\zeta}\langle\alpha\eta|\,V\,|\gamma\zeta\rangle\, g^{II}(\gamma t,\zeta t,\eta t,\beta t'), \end{aligned} \tag{2.30}$$

where the 2p propagator is defined by

$$g^{II}(\gamma t,\zeta t,\eta t,\beta t') = (-i)\,\langle\Psi_0|\,T[a^\dagger_\eta(t)a_\zeta(t)a_\gamma(t)a^\dagger_\beta(t')]\,|\Psi_0\rangle\,. \tag{2.31}$$

Fourier transforming Eq. (2.30) yields:

$$\begin{aligned} g(\alpha,\beta,\omega) &= g^0(\alpha,\beta,\omega) + \sum_{\gamma\delta} g^0(\alpha,\gamma,\omega)\,\Big[\,(-i)\oint\frac{d\omega'}{2\pi}\sum_{\mu\nu}\langle\gamma\mu|\,V\,|\delta\nu\rangle\, g(\nu,\mu,\omega') \\ &+ \frac{1}{2}\oint\frac{d\omega_1}{2\pi}\oint\frac{d\omega_2}{2\pi}\sum_{\xi\mu\nu}\sum_{\eta\rho\sigma}\langle\gamma\mu|\,V\,|\xi\nu\rangle\, g(\xi,\eta,\omega_1)g(\nu,\rho,\omega_2) \\ &\quad g(\sigma,\mu,\omega_1+\omega_2-\omega)\,\langle\eta\rho|\,\Gamma(\omega_1,\omega_2,\omega_1+\omega_2-\omega)\,|\delta\sigma\rangle\,\Big]\;\; g(\delta,\beta,\omega) \end{aligned} \tag{2.32}$$

This represents an alternative form of the Dyson equation, identifying the quantity in square brackets as the self-energy. This equivalence is diagrammatically represented in Fig. 2.3. To obtain this result, one employs the relation between the 2p propagator and effective interaction shown in Fig. 2.4.

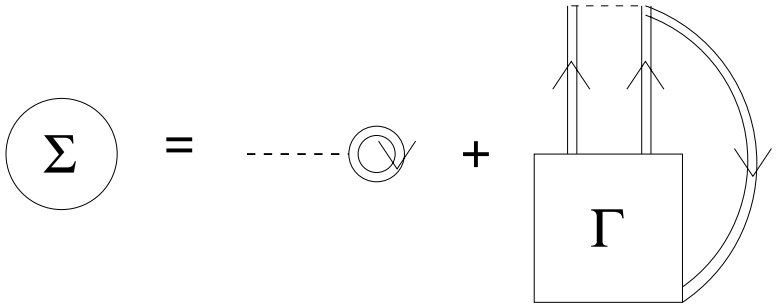

Figure 2.3: The diagrammatic expression for the self-energy in the ladder approximation relating Σ to the NN interaction, the effective interaction, the noninteracting dressed 2p propagator, and the sp propagator.

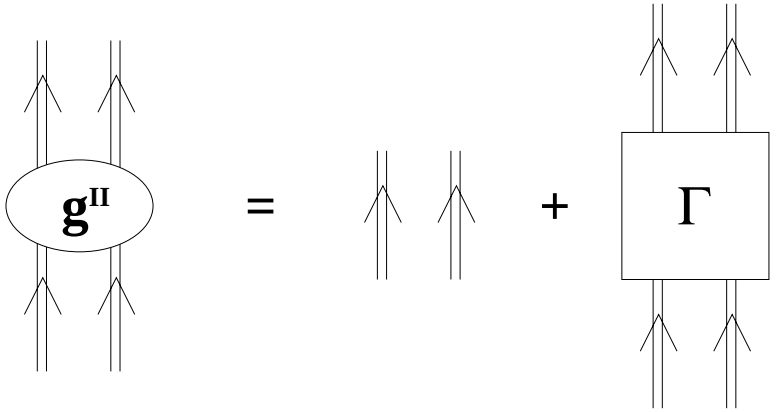

Figure 2.4: The diagrammatic representation of the relation between the interacting 2p propagator, the noninteracting dressed 2p propagator, and the effective interaction in the ladder approximation.

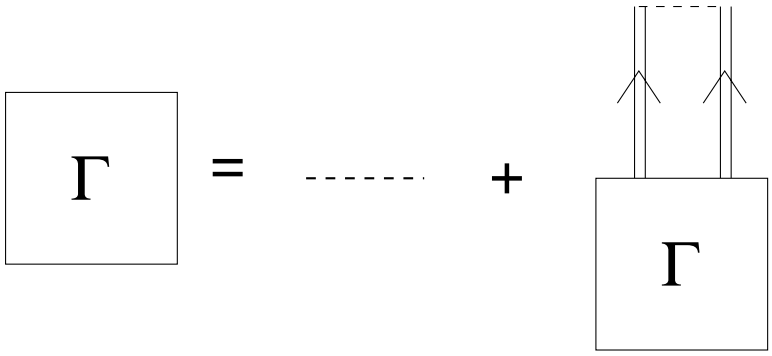

Figure 2.5: Diagrammatic expression of the Bethe-Salpeter equation, Eq. (2.33), for the effective interaction.

2.5 Self-Consistent Green's Functions

One can illustrate the procedure for solving for the interacting sp propagator in nuclear matter by considering the following steps:

1. Calculate the effective interaction from the NN interaction as shown diagrammatically in Fig. 2.5 using an ansatz for the interacting propagator.

The actual solution is obtained in an angular-momentum-coupled partial-wave basis in momentum space

$$\begin{aligned}\langle k_r|\Gamma^{JST}_{LL'}(P,\Omega)|k'_r\rangle &= \langle k_r|V^{JST}_{LL'}|k'_r\rangle \\ &+ \frac{1}{2}\frac{1}{(2\pi)^3}\sum_{L''}\int dq\, q^2\langle k_r|V^{JST}_{LL''}|q\rangle g^{II}_f(q,P,\Omega)\langle q|\Gamma^{JST}_{L''L'}(P,\Omega)|k'_r\rangle.\end{aligned} \tag{2.33}$$

This result is obtained by averaging the noninteracting 2p propagator over all angles as follows

$$g^{II}_f(q,P,\Omega) = \frac{i}{2\pi}\langle\int d\omega g(\overrightarrow{P}+\overrightarrow{q},\frac{\Omega}{2}+\omega)g(\overrightarrow{P}-\overrightarrow{q},\frac{\Omega}{2}-\omega)\rangle_\theta \tag{2.34}$$

$$\begin{aligned}&= \langle -\int_{-\infty}^{\varepsilon_F}\int_{-\infty}^{\varepsilon_F} d\omega d\omega' \frac{S_h(\overrightarrow{P}+\overrightarrow{q},\omega)S_h(\overrightarrow{P}-\overrightarrow{q},\omega')}{\Omega-\omega-\omega'-i\eta} \\ &+ \int_{\varepsilon_F}^{\infty}\int_{\varepsilon_F}^{\infty} d\omega d\omega' \frac{S_p(\overrightarrow{P}+\overrightarrow{q},\omega)S_p(\overrightarrow{P}-\overrightarrow{q},\omega')}{\Omega-\omega-\omega'+i\eta}\rangle_\theta,\end{aligned} \tag{2.35}$$

where the angular brackets denote angle-averaged quantities.

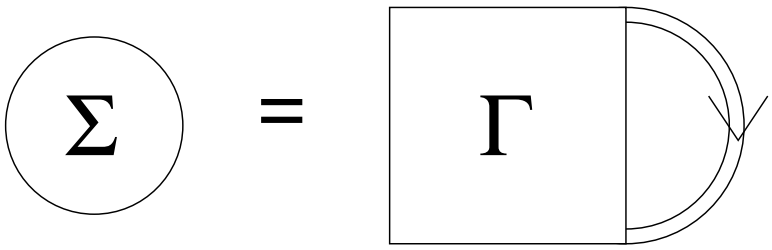

Figure 2.6: Diagrammatic expression of Eq. (2.36) relating the self-energy to the effective interaction and dressed sp propagator.

2. Using the diagonal elements of Γ, calculate the self-energy according to Fig. 2.6. This is mathematically expressed in the following way

$$\Sigma(k,\omega) = -\frac{i}{(2\pi)^4}\int d^3q \int d\omega' \langle k,q|\Gamma(P,\Omega)|k,q\rangle g(q,\omega'). \tag{2.36}$$

The actual evaluation of this result is performed in the partial wave basis. This leads to a summation over partial wave channels and two integrations involving q (the magnitude of sp momentum) and ω' (which explores the off-shell nature of the propagator).

3. Determine the new sp propagator from the Dyson equation which can be expressed as illustrated in Fig. 2.7 in the following way:

$$\begin{aligned} g(k,\omega) &= g_0(k,\omega) + g_0(k,\omega)\Sigma(k,\omega)g(k,\omega) && (2.37)\\ &= \frac{1}{\omega - \frac{k^2}{2m} - \Sigma(k,\omega)} && (2.38) \end{aligned}$$

There are three primary differences between the sp propagator in calculations in which only the sp energy is modified by the medium and the sp propagator obtained with the scheme outlined above.

1. The sp energies, $\varepsilon_k = \frac{k^2}{2m} + U(k)$, where $U(k)$ represents the average potential due to the interaction, instead become quasiparticle energies, ε_{qp} , identifying the center of the peak in the strength distribution.

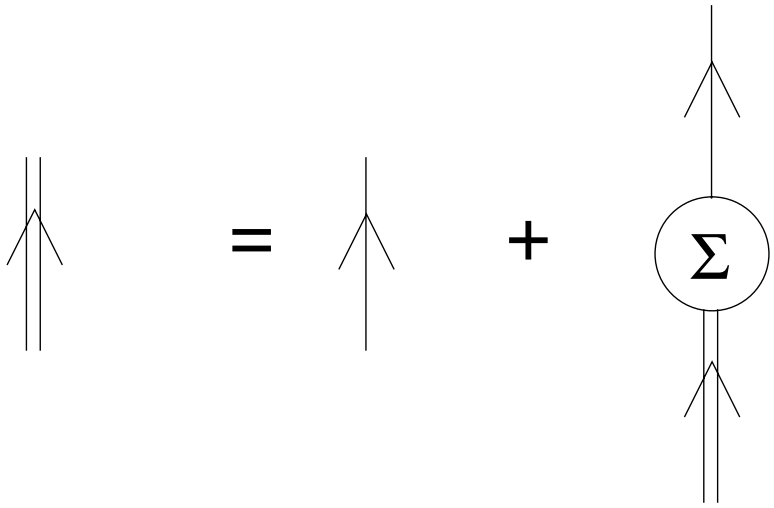

Figure 2.7: Diagrammatic expression of the Dyson equation, Eq. (2.37) from the sp propagator in terms of the self-energy and the noninteracting sp propagator.

2. There is no longer a δ-function peak for sp excitations, but rather a continuous strength distribution which, near to the quasiparticle peak, is represented by a lorentzian with a finite width, except at k_F.

3. Away from the quasiparticle peak, a k-independent high-energy contribution is obtained and, at low energy, a k-dependent distribution arises on account of the coupling to 2h-1p excitations.

Beginning with mean-field propagators, Vonderfecht has performed a first solution of the scheme outlined above starting with mean-field propagators, producing a dressed propagator and corresponding self-energy. The next step would clearly be to repeat the above outlined set of equations with the new, dressed sp propagator. The above set of equations must be iterated until it is self-consistent, stated as the following condition:

$$[\text{input sp propagator}] = [\text{output sp propagator}]$$

A more detailed description of convergence conditions will be given in the following chapter.

Chapter 3

Computational Scheme

3.1 Representation of Single-Particle Quantities

The solution of the scheme outlined in Chapter 2 with fully dressed propagation between interactions has not been completely implemented so far. An advanced approximation has been made by Bożek [64] with an emphasis on pairing properties using a semi-realistic, separable interaction. Other steps toward a complete solution have been presented in Refs. [33],[65],[66], and [63]. Nevertheless, a complete solution of this iteration scheme with the full propagator and a realistic interaction has not been presented. A reason for this may be the computational difficulty. Straightforward calculation with enough points to be useful requires a great amount of computer time and memory.

Parametrization of the sp spectral functions at each step to speed up the iteration process was proposed by Gearhart [41]. While this may be the best option for speeding up the calculation, it has presented some complications. For instance, the spectral function and self-energy should contain equivalent information, and the self-energy is a smooth function while the spectral functions have sharp peaks and broad backgrounds. Thus, fitting the spectral function with a parametrization requires the sum of at least two functions, one sharp (modified lorentzian) peak and one broad background [67]. The resulting self-energy can be obtained from the spectral function by inverting the Dyson equation:

$$\text{Im } \Sigma(k,\omega) = \frac{\text{Im } g(k,\omega)}{(\omega - \frac{k^2}{2m} - \text{Re } g(k,\omega))^2 + (\text{Im } g(k,\omega))^2}, \tag{3.1}$$

where Im $g(k,\omega)$ represents the spectral function up to a constant. The change in

derivative of the spectral function, where one function ceases to dominate and the other takes over, creates nonphysical structures in the imaginary part of the self energy. For this reason, a parametrization of the smoother self-energy has been chosen for this work yielding both well-behaved self-energies and spectral functions.

We will now illustrate that the sp spectral function is completely determined from a set of parameters which describe Im Σ. The spectral function can be written in terms of the self-energy as,

$$S(k,\omega) = \frac{1}{\pi} \frac{\text{Im } \Sigma(k,\omega)}{[\omega - \frac{k^2}{2m} - \text{Re } \Sigma(k,\omega)]^2 + [\text{Im } \Sigma(k,\omega)]^2}, \tag{3.2}$$

where Re $\Sigma(k,\omega) = \Sigma^{\text{HF}}(k) + \text{Re } \Sigma^{\Delta}(k,\omega)$. Therefore, the spectral function can be completely expressed in terms of Im $\Sigma(k,\omega)$, Re $\Sigma^{\Delta}(k,\omega)$, and $\Sigma^{\text{HF}}(k)$. The Re $\Sigma^{\Delta}(k,\omega)$ is constructed from the imaginary part of the self-energy as follows

$$\begin{aligned} \text{Re } \Sigma^{\Delta}(k,\omega) &= P\int_{-\infty}^{\epsilon_F} d\omega' \frac{\text{Im } \Sigma(k,\omega')}{\omega - \omega'} - P\int_{\epsilon_F}^{\infty} d\omega' \frac{\text{Im } \Sigma(k,\omega')}{\omega - \omega'} & (3.3) \\ &= \text{Re } \Sigma^{\Delta >}(k,\omega) + \text{Re } \Sigma^{\Delta <}(k,\omega). & (3.4) \end{aligned}$$

The correlated Hartree-Fock (HF) contribution, $\Sigma^{\text{HF}}(k)$, in a given iteration step is determined as follows. The quasi-particle (qp) spectrum identifies the location of the peak of the spectral function and is determined by

$$\varepsilon_{qp} = \frac{k^2}{2m} + \text{Re } \Sigma(k, \varepsilon_{qp}). \tag{3.5}$$

The qp spectrum from a previous iteration, $(i-1)$, can be used to determine the correlated Hartree-Fock term, $\Sigma_i^{\text{HF}}(k)$ as follows. From

$$\Sigma_{\text{trial}}^{\text{HF}}(k) = \varepsilon_{i-1,qp}(k) - \frac{k^2}{2m} - \text{Re } \Sigma_i^{\Delta}(k, \varepsilon_{i-1,qp}(k)), \tag{3.6}$$

one has all of the ingredients to calculate a spectral function, $S_{\text{trial}}(k,\omega)$ to be used in a calculation of the distribution function, $n_{\text{trial}}(k)$, which is an ingredient in the new correlated HF self-energy (i),

$$\Sigma_i^{\text{HF}}(k) = \int d^3k'\, V(k,k')\, n_{\text{trial}}(k'), \tag{3.7}$$

where $V(k,k') = \langle kk'| V |kk'\rangle$. This completes the construction of a new qp spectrum, but most important for the next iteration, it yields a new Fermi energy by finding the solution of the following equation for $k = k_F$.

$$\omega = \varepsilon_k - \frac{k^2}{2m} - \text{Re } \Sigma(k,\omega) \tag{3.8}$$

The qp spectrum experiences only minor changes from step to step, but we calculate the spectrum explicitly at each step to monitor convergence. This is also done with the parameters used to describe Im Σ.

After determining that the SCGF iteration scheme can be performed by parametrizing the imaginary part of the self-energy, we now turn to the choice of functional form for Im $\Sigma(\omega)$. The imaginary part of the self-energy requires the use of two different energy scales for an an adequate fit: a linear scale for ω near ϵ_F, and a scale governed by $\log(\omega - \epsilon_F)$ for ω far from ϵ_F. Original results of Vonderfecht and the parametrized fit used in the present work are shown in Figs. 3.1 to 3.4. While the imaginary part of the self-energy is smooth in ω, it also varies smoothly in momentum, as can be seen in the Vonderfecht values shown in Figs. 3.2 and 3.4. This illustrates that the imaginary part of the self-energy is a particularly suitable choice for a parametrization since a functional form in ω will depend on parameters which will also be continuous in k. The analytical form best suited to the results of Vonderfecht for energies far from ε_F is constructed using Gaussians of the following form,

$$G_i = P_i \exp\{-\frac{(\log|\omega - \varepsilon_F| - C_i)^2}{2W_i^2}\}, \tag{3.9}$$

yielding the following representation of the imaginary part of the self-energy

$$\text{Im } \Sigma(k,\omega) = \sum_{i=1}^{4} G_i. \tag{3.10}$$

The fit is generated using the functional form for the imaginary part of the self-energy which employs the sum of two Gaussians on either side of ε_F. On the particle side of the Fermi energy, at high energy we will employ a Gaussian according to Eq.

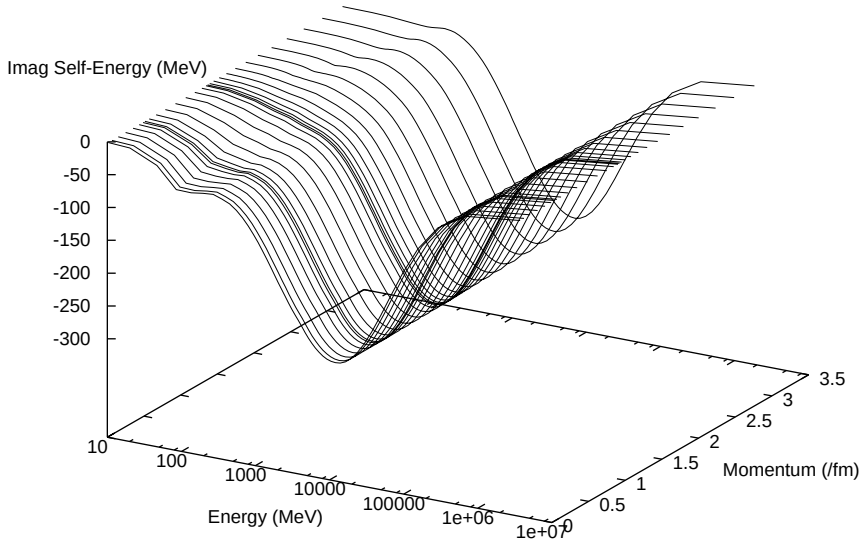

Figure 3.1: Original results for the imaginary part of the self-energy, Im $\Sigma(k, \omega - \varepsilon_F)$, calculated by Vonderfecht using a starting point of mean-field propagators for energies greater than the Fermi energy.

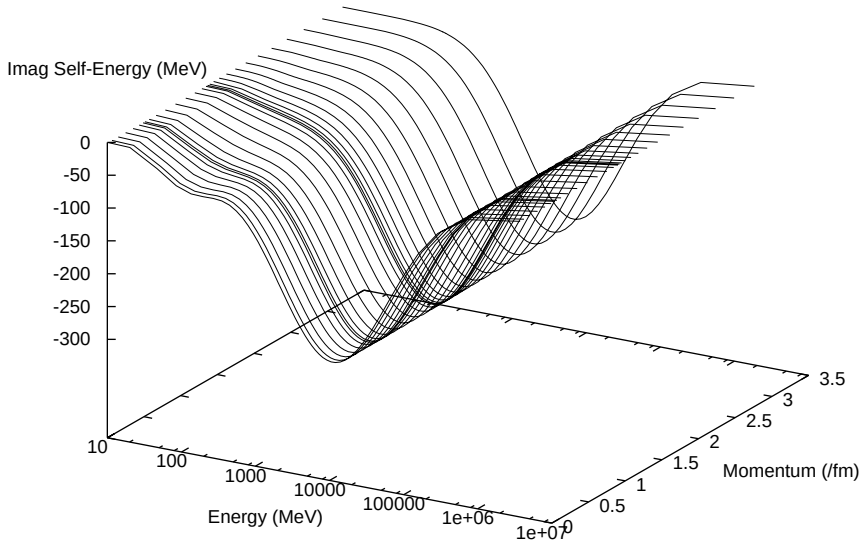

Figure 3.2: Parametrization of the imaginary part of the self-energy for energies greater than the Fermi energy using the functional form discussed in the text.

(3.9) which will be referred to as G_1. This structure reflects the effects of short-range correlations and is nearly momentum independent at a given density. At low energy on the particle side, G_2 contains the effects of the tensor correlations and low-lying excitations. To properly describe the behavior near the Fermi energy, at energies below its peak, a linear scale for G_2 is employed. The width is determined by the condition that the value at half the distance between the peak and the Fermi energy is half of the maximum. To ensure quadratic behavior at the Fermi energy while keeping the function and its first derivative continuous, the following reduction factor is applied,

$$f_{kill}(\omega) = \{\frac{\omega - \varepsilon_F}{C_i - \varepsilon_F}\}^x, \tag{3.11}$$

where x varies linearly in ω from zero at $\omega = C_i$ to two at $\omega = \varepsilon_F$. On the hole side of the Fermi energy, at low energy, G_3 is employed. Its functional form mirrors that of G_2. At even lower energy is the fourth Gaussian structure, G_4, which is important

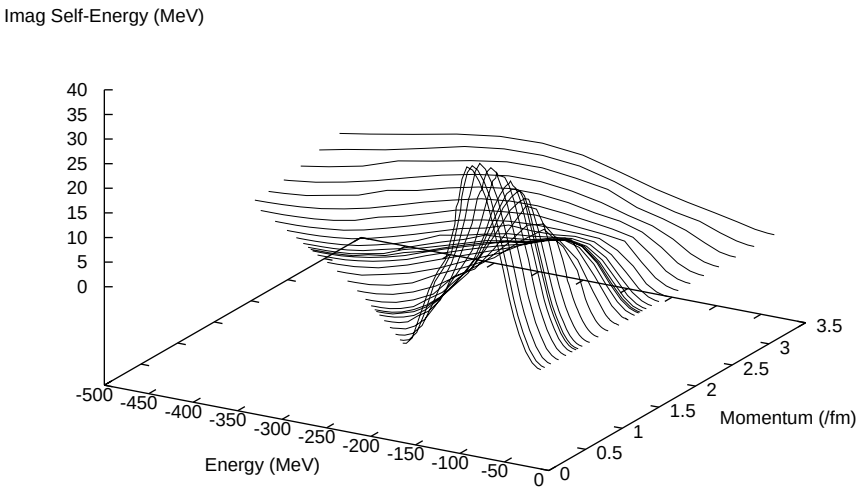

Figure 3.3: Original results for the imaginary part of the self-energy calculated by Vonderfecht using a starting point of mean-field propagators for energies less than the Fermi energy.

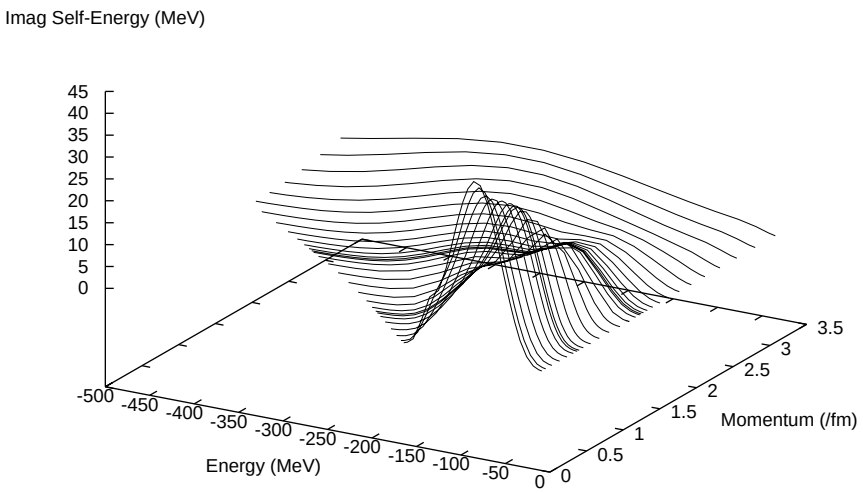

Figure 3.4: Parametrization of the imaginary part of the self-energy for energies less than the Fermi energy using the functional form discussed in the text.

for the description of high-momentum components. At high momentum, $k > k_F$, its peak location has a $(-\frac{k^2}{2m})$ dependence.

Given a good fit to a realistic Im Σ guarantees a good fit of the corresponding spectral functions. Another important property of this approximation is that the parameters determining these self-energies vary smoothly with k such that they can be interpolated to arbitrary sp momenta. The initial values for these parameters are displayed in Fig. 3.5. Note again that the high-energy Gaussian parameters have only weak k-dependence, if any. This is the source of the k-independent high-energy tail in the spectral functions expected in any description of short-range correlations [68]. Figs. 3.1 and 3.3 illustrate that the use of these Gaussians allows an accurate fit and generates appropriate spectral functions while maintaining a manageable form. A more direct comparison of numerical results and their analytical fit is illustrated in Figs. 3.6 to 3.7. The parametrized {Im Σ} plays a key role in the present iteration scheme. The twelve parameters used to describe it are displayed in Fig. 3.5.

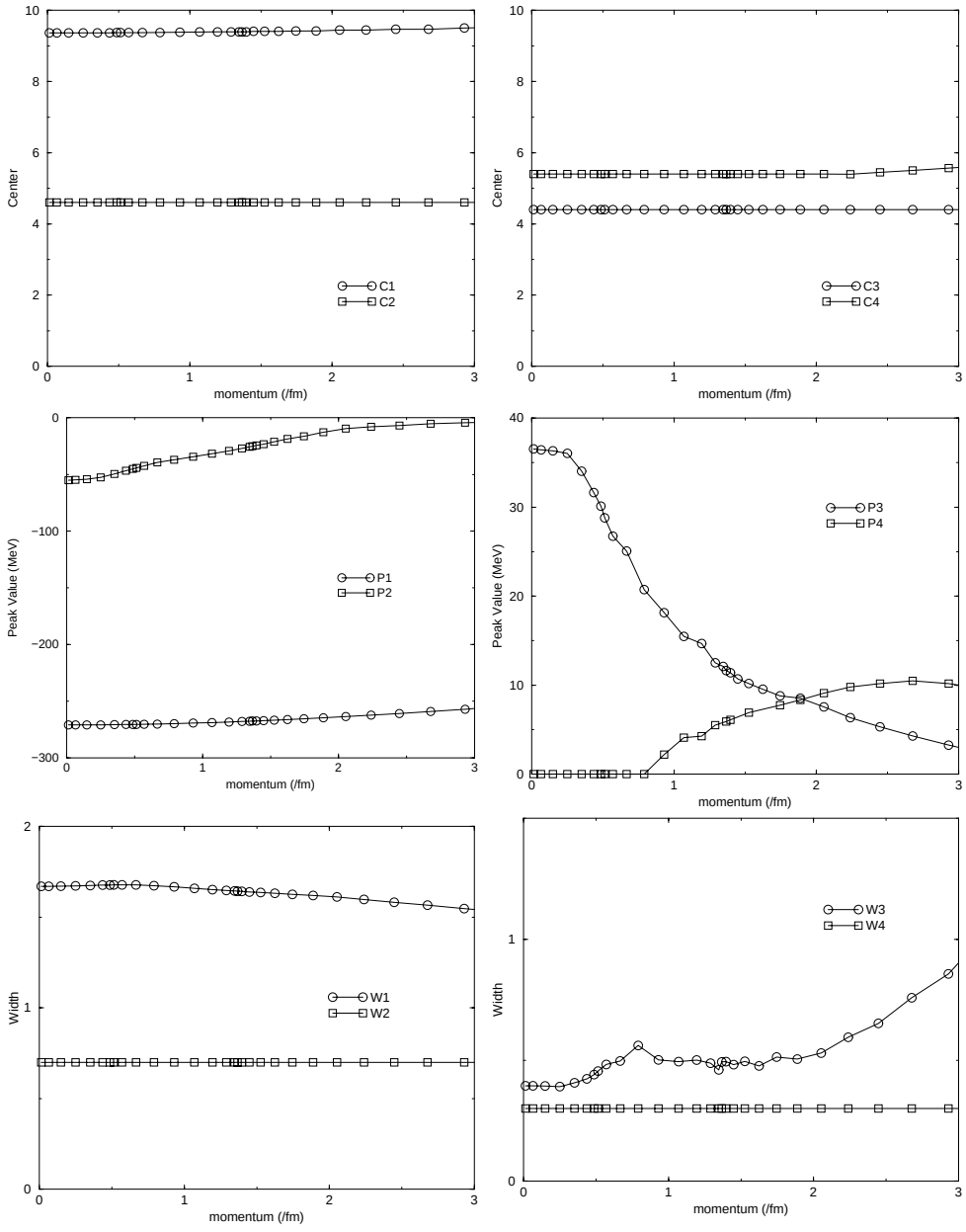

Figure 3.5: Parameters used to describe the Im $\Sigma(\omega)$ ansatz with the form presented in the text.

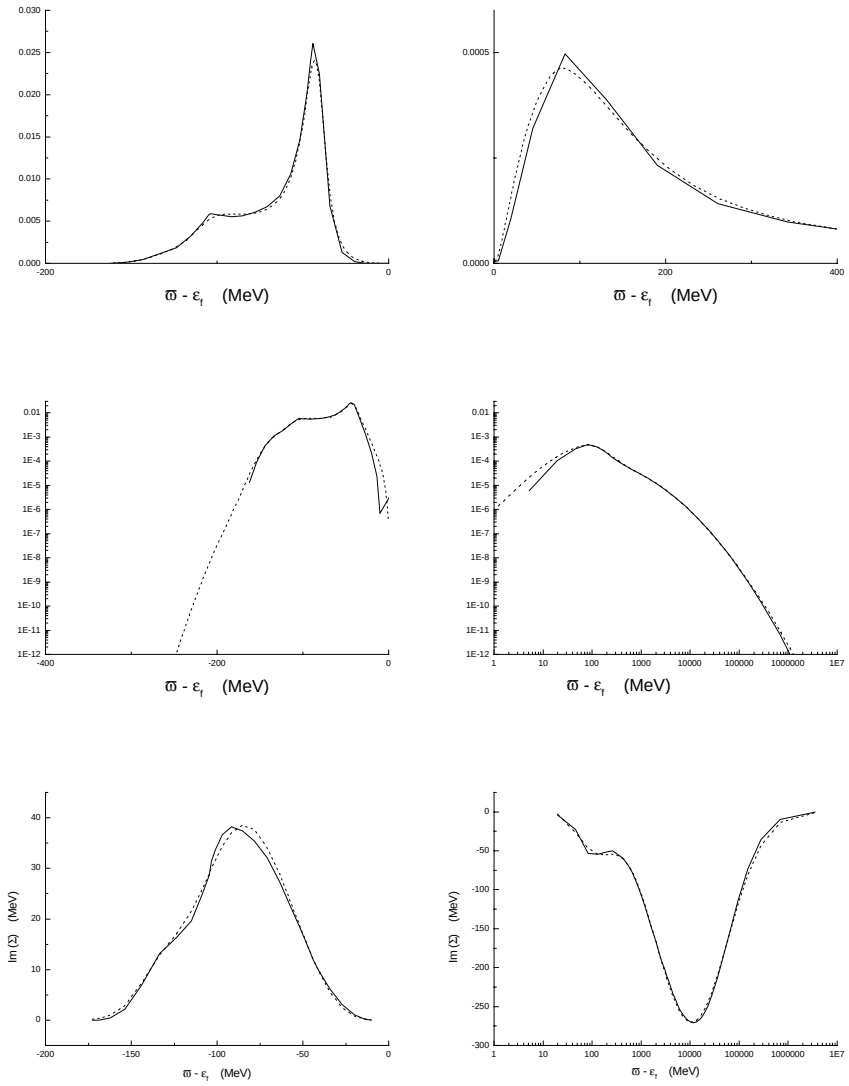

Figure 3.6: Comparison of original results of Vonderfecht (solid lines) and their parametrized representation (dashed lines) for $k = 0$. The top and middle plots display the spectral function and the bottom plots show the corresponding Im $\Sigma(\omega - \varepsilon_F)$.

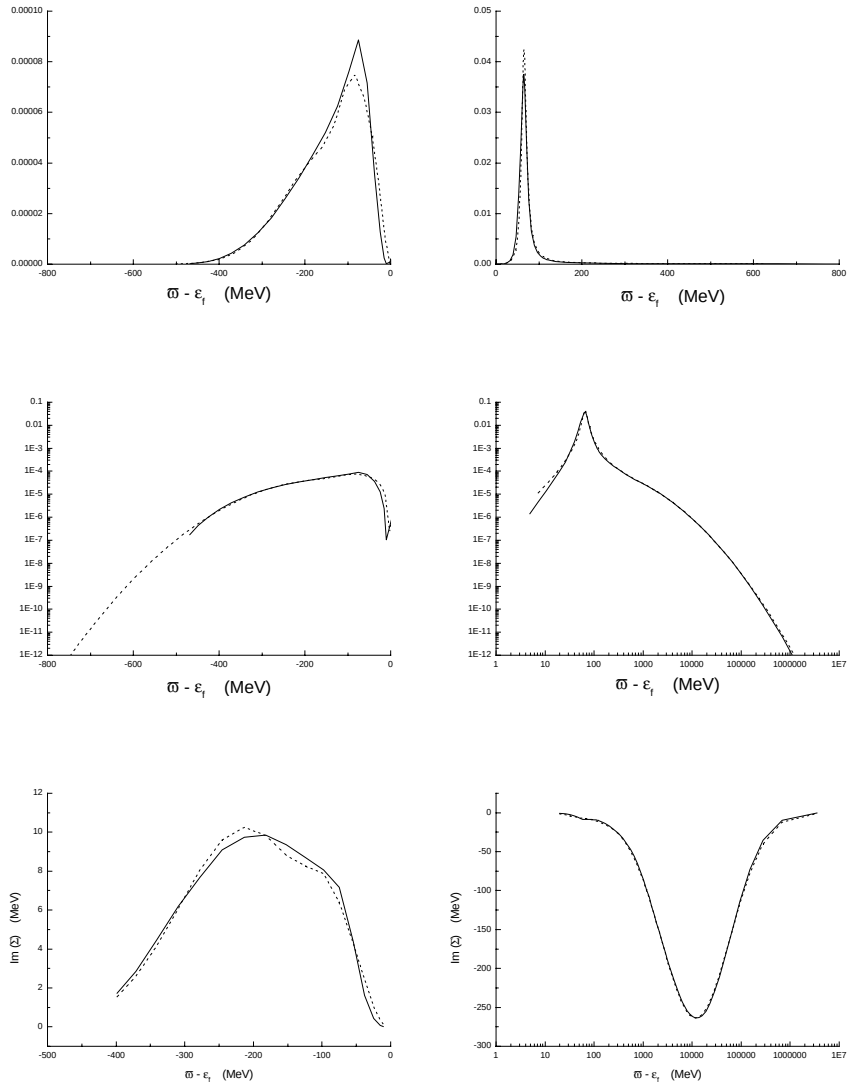

Figure 3.7: Comparison of original results of Vonderfecht (solid lines) and their parametrized representation (dashed lines) for $k = 2.2\ \mathrm{fm}^{-1}$. The top and middle plots display the spectral function and the bottom plots show the corresponding Im $\Sigma(\omega - \varepsilon_F)$.

An important property of this fit is that the sp strength sum rule is met automatically due to the fact that Im $\Sigma \to 0$ for $\omega \to \pm\infty$. Then, the fit is also constrained separately to describe the momentum distribution. Additionally, the first moment of the sp strength is also constrained automatically by the fit. This has the advantage of constraining the binding energy obtained by the fit.

The values of the parameters along with Fermi energy, particle density, and binding energy will be used to gauge the level of self-consistency. A nontrivial property of a self-consistent solution is that the calculated particle density obtained from the momentum distribution exactly corresponds with the Fermi momentum [14] according to $\rho = 2k_F^3/3\pi^2$.

3.2 Noninteracting Two-Particle Propagator

With the description of the sp propagator complete, the next step in the iteration scheme is the computation of the noninteracting 2p propagator. For a self-consistent solution, the sp propagator must be used to determine the dressed but noninteracting 2p propagator, g_f^{II},

$$g_f^{II}(k_1, k_2, \Omega) = \frac{i}{2\pi} \int d\omega \, g(k_1, \omega) \, g(k_2, \Omega - \omega), \tag{3.12}$$

which is used in the calculation of the effective interaction. Inserting the spectral representation of the propagator, Eq. (2.8), this expression corresponds to the energy convolution of the two sp propagators. The terms with both poles on the same side of the real axis can be evaluated with a contour in the other half of the plane and will not contribute, leaving only hh and pp propagation:

$$\begin{aligned} g_f^{II}(k_1, k_2, \Omega) &= -\int d\omega \int d\omega' \, \frac{S_h(k_1, \omega) S_h(k_2, \omega')}{\Omega - \omega - \omega' - i\eta} \\ &+ \int d\omega \int d\omega' \, \frac{S_p(k_1, \omega) S_p(k_2, \omega')}{\Omega - \omega - \omega' + i\eta}. \end{aligned} \tag{3.13}$$

To calculate this quantity, we will consider the sp spectral function as the sum of two functions: a Lorentzian peak (P) near ε_{qp} and a smooth background ($B = S - P$).

For the calculation of the $g_f^{II}(k_1, k_2, \Omega)$, a Lorentzian is a good approximation around the peak of the spectral function, in which case,

$$P(k,\omega) = \frac{1}{\pi} \frac{z(k)^2 |I(k)|}{(\omega - \varepsilon_{qp}(k))^2 + z(k)^2 I(k)^2}, \tag{3.14}$$

where $z = 1/(1 - R')$, I is the on-shell value of the imaginary part of the self-energy, and R' is the on-shell value of the derivative with respect to energy of the real part of the self-energy. Since this approximation is only applicable near the peak, it is multiplied by a modifying function so that it tends quadratically to zero at a distance of $|\omega - \varepsilon_{qp}| = |10I|$. As a result, the background is a more smoothly varying object,

$$B(k,\omega) = S(k,\omega) - P(k,\omega) \tag{3.15}$$

that can be handled numerically.

The imaginary part of the hh-term of the noninteracting 2p propagator [69] is given by

$$\begin{aligned}
\text{Im } g_f^{II>}(k_1, k_2, \Omega) &= -\pi \int_{\Omega-\varepsilon_F}^{\varepsilon_F} d\omega \, S_h(k_1, \omega) \, S_h(k_2, \Omega - \omega) \\
&= -\pi \int_{\Omega-\varepsilon_F}^{\varepsilon_F} d\omega \, [P(k_1, \omega) + B(k_1, \omega)] \, [P(k_2, \Omega - \omega) + B(k_2, \Omega - \omega)] \\
&= -\pi \int_{\Omega-\varepsilon_F}^{\varepsilon_F} d\omega \, [P_1(\omega) P_2(\Omega - \omega) + P_1(\omega) B_2(\Omega - \omega) \\
&+ B_1(\omega) P_2(\Omega - \omega) + B_1(\omega) B_2(\Omega - \omega)]
\end{aligned} \tag{3.16}$$

which presents four terms to be integrated separately. The first term will only contribute in the case of $k_1 < k_F$, $\Omega - \varepsilon_F < \varepsilon_{qp}(k_1) + |10I_1|$, $k_2 < k_F$, and $\Omega - \varepsilon_F < \varepsilon_{qp}(k_2) + |10I_2|$. When these conditions are met, there will be a peak-peak contribution in the integrand to consider, and any integration required over it can be performed analytically. Since the background is not as strongly varying in energy as the peaks, the second and third term can be evaluated by approximating the background as a constant over the width of the peak and analytically integrating over the lorentzian peak. The fourth term can be evaluated numerically as a convolution of two well-behaved functions. This procedure allows a quick evaluation while still employing the complete $S(k, \omega)$.

Eq. (3.13) implies that the real and imaginary parts of g_f^{II} obey a dispersion relation. For the calculation of the effective interaction, Γ, both the real and imaginary part of the noninteracting 2p propagator are required. The real part, Re g_f^{II}, is therefore calculated via the appropriate dispersion relation:

$$\begin{aligned} \text{Re } g_f^{II}(k_1,k_2,\Omega) &= \frac{1}{\pi}P\int_{-\infty}^{2\varepsilon_F} d\Omega' \frac{\text{Im } g_f^{II}(k_1,k_2,\Omega')}{\Omega-\Omega'} \\ &- \frac{1}{\pi}P\int_{2\varepsilon_F}^{\infty} d\Omega' \frac{\text{Im } g_f^{II}(k_1,k_2,\Omega')}{\Omega-\Omega'}. \end{aligned} \tag{3.17}$$

This information is then stored on a three-dimensional grid of (k_1,k_2,Ω) to be interpolated for use in the calculation of the effective interaction. Interpolation will not be accurate near the peak of Im g_f^{II} for sp momenta near k_F. In this case, a 2p Lorentzian approximation is employed [69],

$$\text{Im } g_f^{II}(k_1,k_2,\Omega) = \frac{z^{II}}{\pi}\frac{|A^{II}|}{(\Omega-\Omega_0)^2+(A^{II})^2} \tag{3.18}$$

$$\text{Re } g_f^{II}(k_1,k_2,\Omega) = \frac{z^{II}}{\pi}\frac{(\Omega-\Omega_0)}{(\Omega-\Omega_0)^2+(A^{II})^2}. \tag{3.19}$$

where $z^{II}=z_1z_2$, $A^{II}=z^{II}(I_1+I_2)$, and $\Omega_0=\varepsilon_{qp}(k_1)+\varepsilon_{qp}(k_2)$. As a result, g_f^{II} can be evaluated in terms of (Ω,k_1,k_2).

3.3 Solution for the Effective Interaction

Referring to the previous diagrammatic form of the Bethe-Salpeter equation, Fig. 2.5, one observes that if g_f^{II} and V are known, the only unknown in the equation is the Γ-matrix. A noninteracting 2p propagator is calculated on a discrete set of sp momenta, k_1 and k_2, for use in solving the Bethe-Salpeter equation. This solution requires the use of the center of mass and relative momenta, where the relationship of the variables is illustrated in Fig. 3.8 such that

$$k_1 = \sqrt{\frac{P^2}{4}+q^2+Pq\cos\theta} \tag{3.20}$$

$$k_2 = \sqrt{\frac{P^2}{4}+q^2-Pq\cos\theta}, \tag{3.21}$$

where P is the total momentum of the 2p system and q is the relative momentum. To obtain a θ-independent function, an integral over θ is required for each (P, q, Ω) according to 2.34, using a prescription proposed by Brueckner and Gammel [70]. The results of Ref. [71],[72],[73] have demonstrated that exact treatment of the angular dependence has a minor effect on binding energies and does not change the saturation with respect to an angle-averaged treatment. For certain P and q, angles exist for which k_1 and k_2 are on opposite sides of the Fermi momentum, and Pauli effects prevent hh and pp propagation in the IPM for which there is no contribution to g_f^{II}. Using dressed sp propagators for these momenta, all angles contribute to both pp and hh terms since their spectral functions extend to all energies. The resulting $g_f^{II}(k_1, k_2)$ still contains strong Pauli signatures instead of complete Pauli blocking.

After the calculation of g_f^{II}, the Galitskii integral equation can be solved according to [41],

$$\begin{aligned}\Gamma^{JST}_{LL'}(P,\Omega)(q_i,q_j) &= V^{JST}_{LL'}(q_i,q_j) \\ &+ \frac{1}{2}\frac{1}{(2\pi)^3}\sum_{L''}\int dq_k q_k^2 V^{JST}_{LL''}(q_i,q_k) g_f^{II}(q_k,P,\Omega)\Gamma^{JST}_{L''L'}(P,\Omega)(q_k,q_j),\end{aligned} \tag{3.22}$$

which is equivalent to Eq. (2.33) using a slightly different notation. In order to numerically evaluate the integral, one can use the method of Gaussian quadratures to create a mesh of momenta $\{q_k\}$ and weights $\{w_k\}$ [38],[68],

$$\Gamma^{JST}_{LL'}(P,\Omega)(q_i,q_j) = V^{JST}_{LL'}(q_i,q_j) + \sum_{L''k} w_k q_k^2 V^{JST}_{LL''}(q_i,q_k) g_f^{II}(q_k,P,\Omega)\Gamma^{JST}_{L''L'}(P,\Omega)(q_k,q_j). \tag{3.23}$$

Therefore, the integral equation has been replaced with a matrix equation. One can rewrite the matrix equation for each partial wave with quantum numbers (JST) and each (P, Ω) as

$$\sum_{L''k}[\delta_{LL''}\delta_{ik} - w_k q_k^2 V_{LL''}(q_i,q_k) g_f^{II}(q_k)]\Gamma_{L''L'}(q_i,q_j) = V_{LL'}(q_i,q_j). \tag{3.24}$$

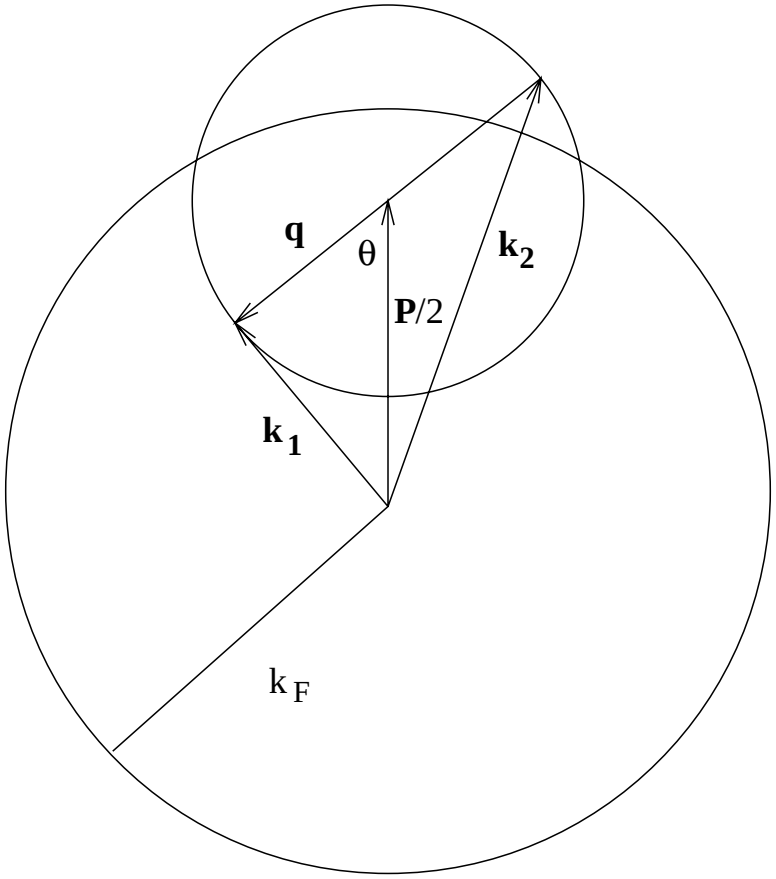

Figure 3.8: An illustration of the change of variables from $\{k_1, k_2|$ to $\{P, q, \theta\}$. The noninteracting 2p propagator must be integrated over the θ variable (angle-averaged) for use in the solution for the effective interaction in a partial-wave expansion.

The resulting matrix equation,

$$A \cdot \Gamma = V, \tag{3.25}$$

uses

$$A_{ij} = [\delta_{LL'}\delta_{ij} - w_j q_j^2 V_{LL'}(q_i, q_j) g_f^{II}(q_j)].$$

Eq. (3.25) can be solved via a matrix inversion to yield the effective interaction according to

$$\Gamma = A^{-1} \cdot V. \tag{3.26}$$

The accuracy of the effective interaction resulting from the matrix inversion is dependent on the choice of relative momentum mesh chosen for each (P, Ω). Any mesh $\{q_k\}$ which will yield a correct A^{-1}, and therefore produce a reliable Γ-matrix, must properly contain the structure of the 2p propagation between interactions. A good test of the validity of a $\{q_k\}$ mesh is the accuracy of the noninteracting 2p density of states, $\rho_f^{II}(P, \Omega)$, where [43]

$$\rho_f^{II}(P, \Omega) = -\frac{1}{\pi} \int dq\, q^2 \,\mathrm{Im}\; g_f^{II}(q, P, \Omega). \tag{3.27}$$

A $g_f^{II}(P, \Omega, q_k)$ which yields a physically reasonable ρ_f^{II} is required to generate a reliable effective interaction from the inverted matrix, A^{-1}. More experience is available with grids that deal with the real part in Ref. [38]. The grids employed in this work take into account the structures of both the real and imaginary parts of $g_f^{II}(P, \Omega, q_k)$.

In this work, the S, P, and D partial waves of the effective interaction are calculated explicitly. The S-waves make the greatest contribution to the imaginary part of the self-energy at normal density, and the contribution of the P-waves is approximately an order of magnitude less [40]. Since the D-waves are yet another order of magnitude weaker than the P-waves, higher waves are expected to have a negligible effect on the imaginary part of the self-energy. The effective interaction is only explicitly solved for these sets of waves. This is consistent with the conclusion of Ref. [68] that contributions to the effective interaction of partial waves with $J > 2$ are

well approximated by the bare interaction. The higher partial waves are therefore included in the bare interaction contributing to the Hartree-Fock term as in [14].

At the empirical saturation density, no pairing instability is observed when dressed propagators are used. This is in stark contrast to the pairing instability obtained when mean-field propagators are used [43]. It is therefore reasonable to expect that no pairing instabilities will be encountered at higher densities either [74]. Since the sp states near k_F have the greatest mean-field character, these are the states that contribute most to bound-pair states. An important effect of the inclusion of off-shell propagation is the depletion of the $k = k_F$ state, such that its quasiparticle peak contains only $\sim$70% of the sp strength in the ansatz propagator. Correspondingly, for the 2p state near $2\varepsilon_F$, a $\sim$50% reduction in strength is obtained, accounting for the disappearance of the pairing instabilities at this density. The absence of pairing can also be seen in the NN cross-sections and phase shifts in Ref. [43]. At lower densities, one expects the instability to occur since deuterons must form in the limit of zero density.

3.4 Single-Particle Self-Energy

Lastly, to solve for the imaginary part of the next iteration's self-energy, we need only the imaginary part of the diagonal elements of the effective interaction. This is the case in nuclear matter because the self-energy is a function of a single sp momentum. Since a single hole- or particle-line closes the effective interaction to determine this self-energy, only diagonal elements will be required and the same initial and final 2p states are probed. These diagonal elements can be separated schematically in three terms as follows,

$$\Gamma = V + \Delta\Gamma^{<} + \Delta\Gamma^{>}. \tag{3.28}$$

The first and second terms must be closed with a hole line and the third term is closed with a particle line. The first term yields the Hartree-Fock contribution. The remaining terms are contained in the following expression, given in a partial wave

basis,

$$\Sigma^{\Delta}(k,\omega) = -\frac{i}{16\pi(2\pi)^4}\sum_{LSTJ}(2T{+}1)(2J{+}1)\int d^3q\int d\omega'\,\Delta\Gamma_{LJST}(K,k_r,\omega{+}\omega')\,g(q,\omega'). \tag{3.29}$$

To evaluate the imaginary part of the self-energy, only the $\Delta\Gamma$ terms need to be considered explicitly, suppressing quantities related to the partial wave basis:

$$\begin{aligned}\text{Im }\Gamma(k_r,K,\Omega) &= \text{Im }\Delta\Gamma^{>}(k_r,K,\Omega),\ \text{for }\Omega < 2\varepsilon_F \\ &= \text{Im }\Delta\Gamma^{<}(k_r,K,\Omega),\ \text{for }\Omega > 2\varepsilon_F. \end{aligned}\tag{3.30}$$

The effective interaction has already been shown to obey a dispersion relation which can be written:

$$\Delta\Gamma^{>}(k_r,K,\Omega) = \frac{1}{\pi}\int_{-\infty}^{2\varepsilon_F} d\Omega'\frac{\text{Im }\Delta\Gamma^{>}(k_r,K,\Omega')}{\Omega-\Omega'-i\eta} \tag{3.31}$$

$$\Delta\Gamma^{<}(k_r,K,\Omega) = \frac{1}{\pi}\int_{2\varepsilon_F}^{\infty} d\Omega'\frac{\text{Im }\Delta\Gamma^{<}(k_r,K,\Omega')}{\Omega-\Omega'+i\eta} \tag{3.32}$$

For the evaluation of the self-energy, it will be useful to employ this separation of $\Delta\Gamma(k_r,K,\Omega)$. Using Eqs. (3.30) to (3.32) in Eq. (3.29), only terms with poles on opposite sides of the real axis of the complex ω'-plane will contribute. One can express the two resulting contributions to the imaginary part of the self-energy in the following form:

$$\text{Im }\Sigma^{\Delta<}(k,\omega) = -\frac{1}{(2\pi)^3}\int d^3q\int_{\varepsilon_F}^{2\varepsilon_F-\omega} d\omega'\,\text{Im }\Gamma^{>}(K,k_r,\omega+\omega')S_p(q,\omega') \tag{3.33}$$

$$\text{Im }\Sigma^{\Delta>}(k,\omega) = -\frac{1}{(2\pi)^3}\int d^3q\int_{2\varepsilon_F-\omega}^{\varepsilon_F} d\omega'\,\text{Im }\Gamma^{<}(K,k_r,\omega+\omega')S_h(q,\omega'). \tag{3.34}$$

The real part of Σ^{Δ} can be found via a dispersion relation, Eq. (3.4), and the Hartree-Fock term is obtained from Eq. (3.7). The self-energy is now fully determined,

$$\Sigma(k,\omega) = \Sigma^{HF}(k) + \Sigma^{\Delta}(k,\omega). \tag{3.35}$$

In the evaluation of Eqs. (3.33) and (3.34), one can save computational time by making a change of variables, $q \to K$ [41]. In this case, as illustrated in Fig. 3.9,

$$K = \frac{|\mathrm{k} + \mathrm{q}|}{2} \tag{3.36}$$

$$k_r = \frac{|\mathrm{k} - \mathrm{q}|}{2} \tag{3.37}$$

and the change of variables can be performed noting that

$$|\mathrm{q}| = |2\mathrm{K} - \mathrm{k}| = \sqrt{4K^2 + k^2 - 4Kk\cos\theta}. \tag{3.38}$$

The q-dependence of the effective interaction is replaced by a $\{K, \theta\}$ dependence. The integration over all internal variables will now be performed over these variables numerically. To do so, one must consider which key points to use to build an integration mesh with gaussian quadrature. Of great concern in such a calculation are Pauli effects, and detailed information on building a suitable grid can be found in Ref. [38].

For each K, the θ-value for which $q = k_F$ signals a discontinuity in $S(q, \omega)$, so this angle will be a key point in building the appropriate mesh. However, such a critical angle does not exist for $K < k - k_F$ or for $K > k + k_F$. These two conditions yield key points to consider in the construction of the K mesh and represent Pauli effects.

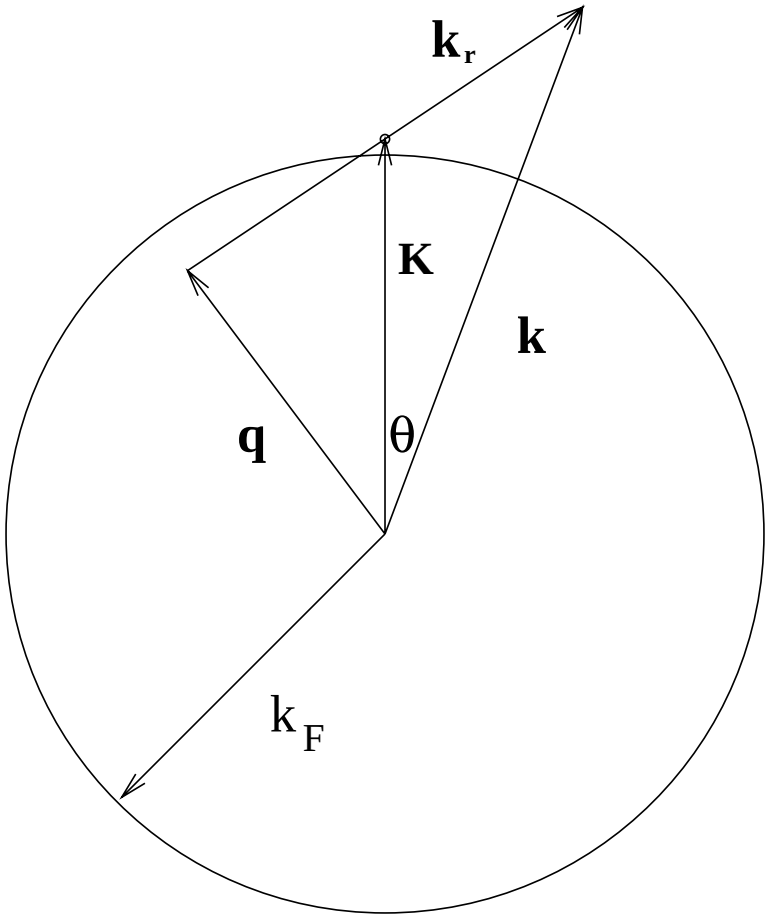

Figure 3.9: An illustration of the change of variables from (k, q) to (K, k_r, θ), used for easier numerical evaluation of the imaginary part of the self-energy.

Chapter 4

Results and Applications

In this chapter, results of the iteration scheme for self-consistent propagators will be presented. The solution at saturation density is shown in detail including results related to the effective interaction in Section 4.2, the self-energy in Section 4.3, and the sp propagator in Section 4.4. The first section discusses the process of iterating to a self-consistent solution of the Dyson equation as coupled to the ladder equation for the effective interaction. To explore saturation properties of the present scheme, another density corresponding to $k_F = 1.45$ fm^{-1} is considered in Section 4.5.

4.1 Iteration of the Single-Particle Propagator

To iterate to a self-consistent solution to the Dyson equation, the imaginary part of Σ is parametrized at each step. The stability of these parameters will be monitored to establish the convergence properties. Furthermore, the Fermi energy, particle density, kinetic energy, potential energy, and binding energy will be of primary importance in assessing self-consistency. The convergence process requires several iterations including the dominant S waves and, in a final step, the inclusion of the P and D waves. The results for the last three steps are discussed in detail.

As an example of the convergence properties of the parameters, consider the value of the peaks of the gaussians representing the imaginary part of the self-energy. The gaussian representing the high-energy peak is very stable during iterations. However, G_2 and G_3, describing contributions of excitations near the Fermi energy, are more sensitive. After several iterations, they settle to final values shown in Figs. 4.1 and 4.2. Because these peaks are located within a few hundred MeV of the Fermi energy,

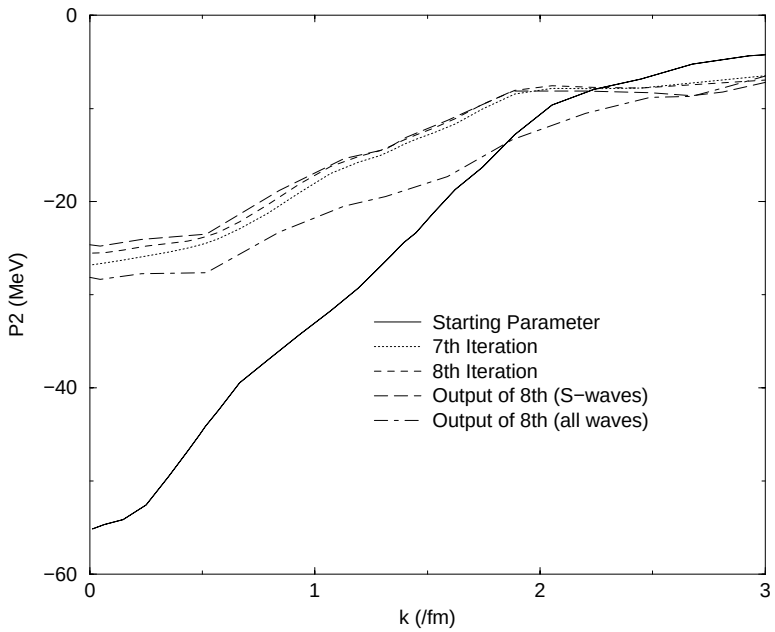

Figure 4.1: Parameters for the peak value of G_2, which describes the imaginary part of the self-energy in the particle domain near the Fermi energy.

the values have a considerable dependence on k and reflect the influence of the tensor force to admix low-lying states [40]. The ansatz solution given by the full line in Figs. 4.1 and 4.2 yields much larger magnitudes than the iterated solution for values at low-k. The values of these parameters determine the number of iterations needed to reach the level of self-consistency obtained in the present work. The corresponding gaussians are the source of fragmentation and depletion of the quasiparticle states at momenta near the Fermi momentum and below. Since these peaks occur in the qp energy domain for these momenta, they can have an important effect on the structure of the spectral function. Their magnitude is over-estimated when calculated starting with independent particles, as shown in Figs. 4.1 and 4.2. This illustrates a general numerical point of this SCGF scheme. Since the ansatz Im Σ was calculated using the IPM, it tends to overestimate the correction to the IPM.

In Table 4.1, we consider the iterative behavior of the Fermi energy, energy per particle, potential energy and kinetic energy. All energies in this table are expressed

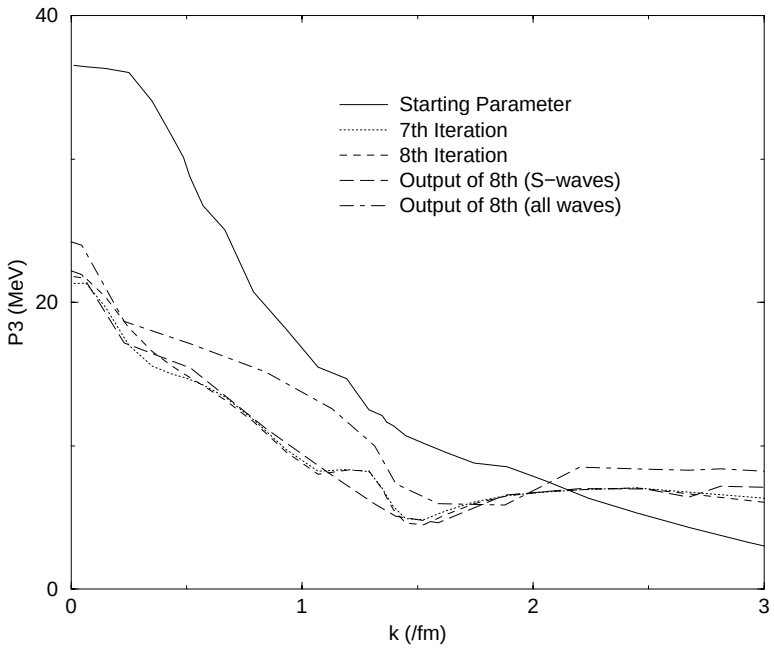

Figure 4.2: Parameters for the peak value of G_3, which describes the imaginary part of the self-energy in the hole domain near the Fermi energy.

in MeV. This table contains the results of the last three iterations using only S wave contributions to the effective interaction and corresponding self-energy. The SCGF scheme was iterated until these results displayed a reasonable level of self-consistency. Then, the S wave solution to the sp propagator was used to calculate the contributions of P and D waves. The corresponding result is given in the second to last line of the table. The inclusion of higher waves yields a larger contribution as compared to BHF calculations using the standard choice of the sp spectrum [68],[14]. The present scheme involving four gaussians, which accurately described the S wave contribution to the imaginary part of the self-energy, may have to be extended to account for the contribution of the higher waves self-consistently. To estimate the self-consistent solution including all waves, the last line in the table displays values obtained from an imaginary part of the self-energy calculated from the average of the parameters corresponding to the previous two lines of the table. The table is included here to illustrate the approach to self-consistency of the results. More discussion of these

iteration	ε_F	E/A	KE/A	PE/A	$\rho(\mathrm{fm}^{-3})$
7	-8.78	-10.62	48.50	-59.11	.167
8	-8.11	-10.89	47.74	-58.73	.168
9 S waves	-7.64	-11.20	48.56	-59.83	.167
all waves	-14.26	-16.51	52.85	-68.80	.169
average result	-11.94	-14.76	53.91	-68.67	.168

Table 4.1: The Fermi energy, energy per particle, kinetic energy, potential energy and particle density calculated for the iterations described in the text.

results can be found in Section 4.4. For any real Fermi fluid, the binding energy is equal to the Fermi energy [75], and this condition may also be a gauge of the literal physical value of our results [20] as shown in Table 4.1.

In the results including only S waves, one notices that the binding energy is more stable from iteration to iteration than the potential or kinetic energies separately. Changes of potential and kinetic energies with iteration tend to cancel one another. This is due to the sampling of the sp hole-strength with k^2 in these quantities which can amplify small changes from iteration at high-k. Since these contributions are concentrated at energies that vary as $-\frac{k^2}{2m}$, the net contribution to the binding tends to cancel, as in Eq. (2.19). The Fermi energy is a more sensitive quantity, but shows reasonable self-consistency at the end of the S wave iterations. This sensitivity is related to the properties of G_2 and G_3 which have a strong effect on the location of the Fermi energy. This location is obtained as the solution for the pole of the on-shell energy condition, Eq. (3.5), for k_F. The small shifts in the peak values of G_2 and G_3 during iteration can move the Fermi energy accordingly.

The behavior of the momentum distribution through the iteration process also displays an interesting convergence behavior. The results from Ref. [40], where the momentum distribution was calculated starting from mean-field propagators, yield an occupation at low momentum of 0.83, which should be compared to the mean-field value of 1. This result represents an overestimate of the self-consistent result of 0.873 if only S waves are considered and 0.865 if S, P, and D waves are included. Fig.4.3

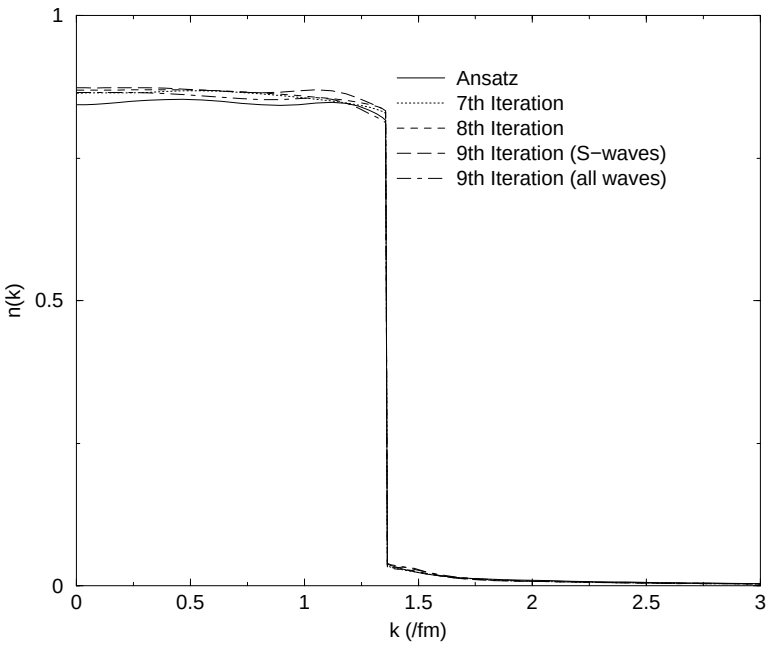

Figure 4.3: The momentum distribution, $n(k)$, for several iterations. The ninth iteration values are found by averaging the eighth iteration output and input.

shows the behavior of the occupation for the iterations shown in Table 4.1.

The behavior of other on-shell characteristics with iteration is illustrated, for the same iteration steps as discussed above, in Figs. 4.4 to 4.7. These values gauge the change in the character of the spectral function near the qp energy and give an intuitive picture of some effects of the steps leading to self-consistency. The sp spectrum and corresponding sp potential are shown in Figs. 4.4 and 4.5, respectively, where

$$U(k) = \varepsilon_{qp}(k) - \frac{k^2}{2m}. \tag{4.1}$$

The S wave solutions show self-consistency, but a significant change in these values is obtained when higher waves are included. This influence of higher waves is greater at higher momenta, and their inclusion has only minor effect at low momentum.

Figure 4.6 displays the qp strength, $z(k)$, as used in Eq. (3.14). The final values are bounded between the values in the IPM and those of the ansatz propagator [40]. At k_F the qp strength represents the jump in the occupation number. The value for

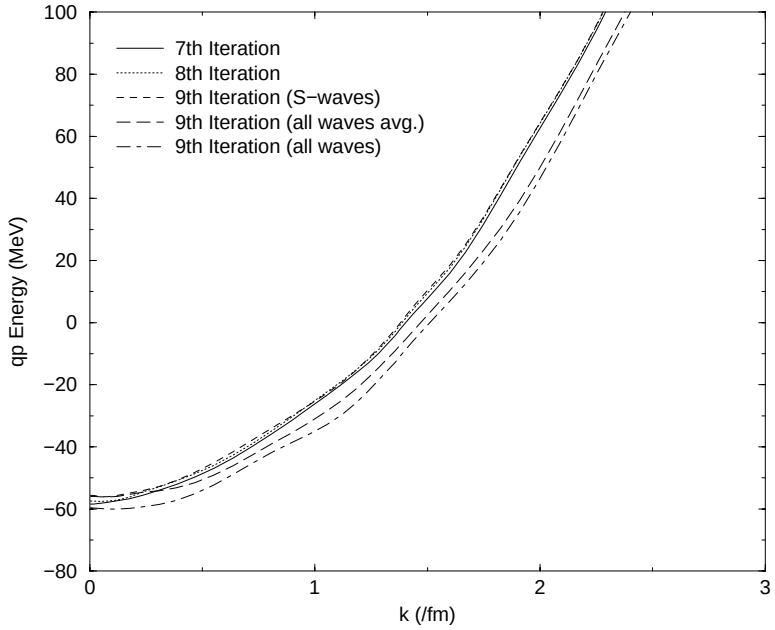

Figure 4.4: The quasiparticle energy, found as the solution to Eq. (3.5), for the same set of iterations as in Table 4.1.

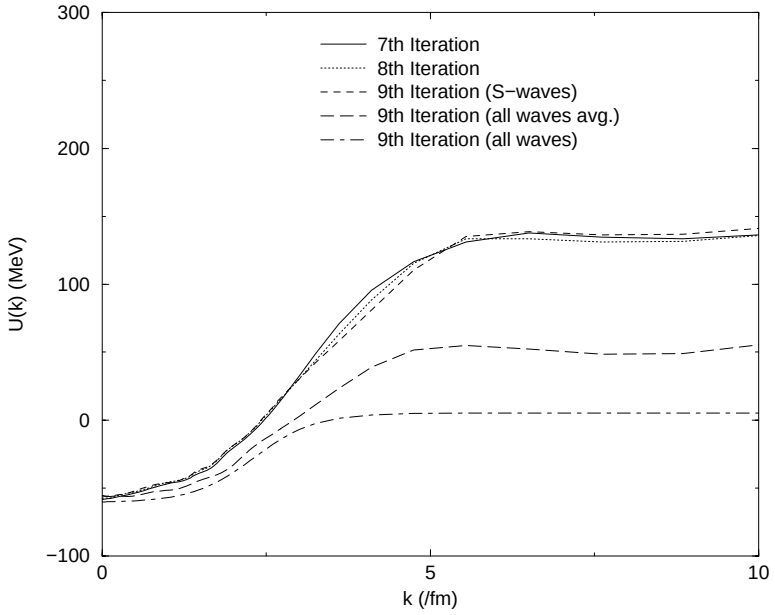

Figure 4.5: The sp potential, determined as $U(k) = \varepsilon_{qp}(k) - \frac{k^2}{2m}$, for the iteration discussed in Table 4.1.

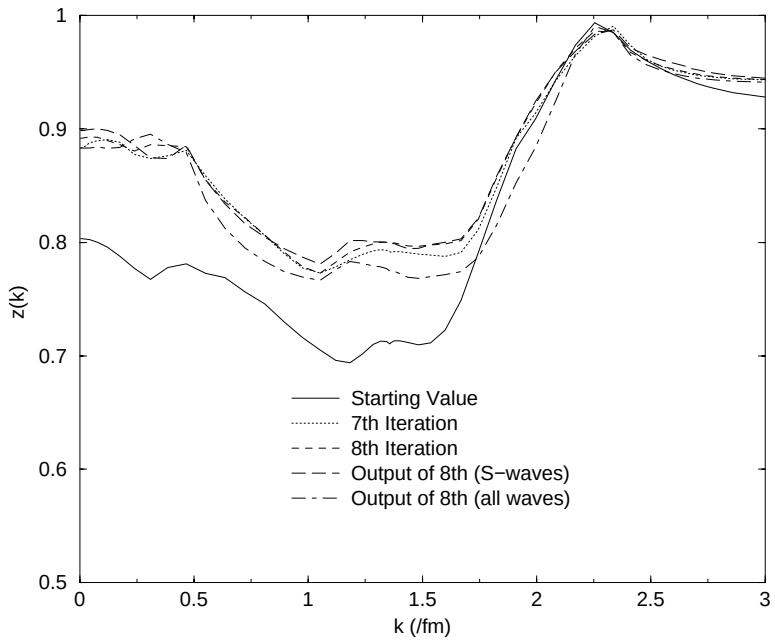

Figure 4.6: The quasiparticle strength as determined from the real part of the self-energy for the same set of iterations as Fig. 4.3.

the ansatz is $z(k_F) = 0.72$ while the present results yields $z(k_F) \simeq 0.80$, as shown in Fig. 4.6. This illustrates again that the self-consistent result is less correlated than the solution starting from mean-field propagators. This is also reflected in the on-shell value of the imaginary part of the self-energy, $I(k)$, which can be interpreted as the width of the qp distribution. For low momenta, $k < 2$ fm^{-1}, subsequent iteration results in lower values of $I(k)$, as seen in Fig. 4.7. For higher momenta, where $I(k)$ is dominated by G_2 this is not the case in accordance with Fig. 4.1. At these momenta, self-consistent propagators mix more strongly with 2p1h states than propagators calculated by starting from the mean field.

The imaginary part of the self-energy for $k = k_F$ is shown for iteration steps leading to self-consistent functions. The self-energy at low and high energy is illustrated in Figs. 4.8 and 4.9, respectively. These confirm the discussion above, showing that each of the four gaussians approaches self-consistency. In the self-consistent solution, a non-negligible low-energy tail is present. These low-energy contributions provide

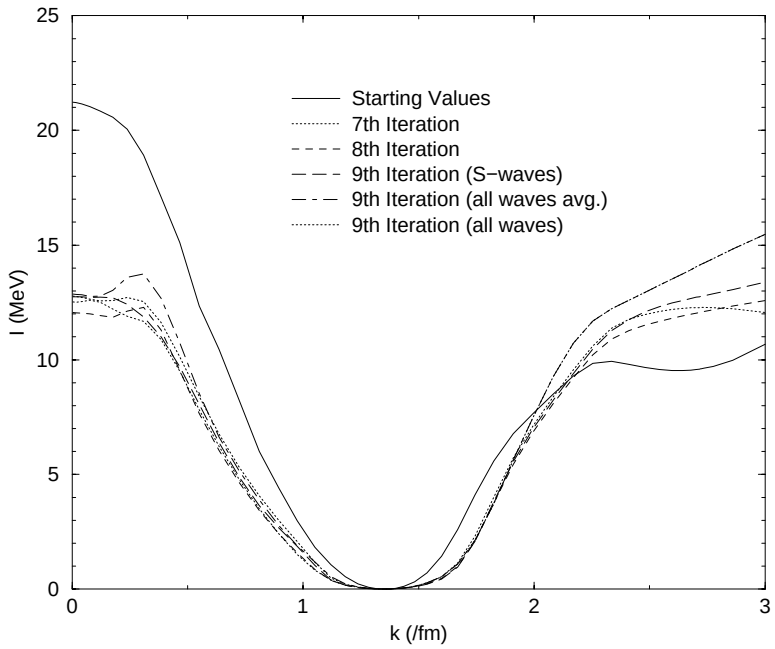

Figure 4.7: The value of the imaginary part of the self-energy at the quasiparticle energy. This value is a gauge of the width of the quasiparticle peak.

binding in a region that is below the threshold present in calculations starting from mean-field propagators. The sp strength in this region contributes to binding in a non-negligible way and is critical to obtain accurate values. These components provide a strong argument for the importance of self-consistency in calculating the effects of short-range correlations.

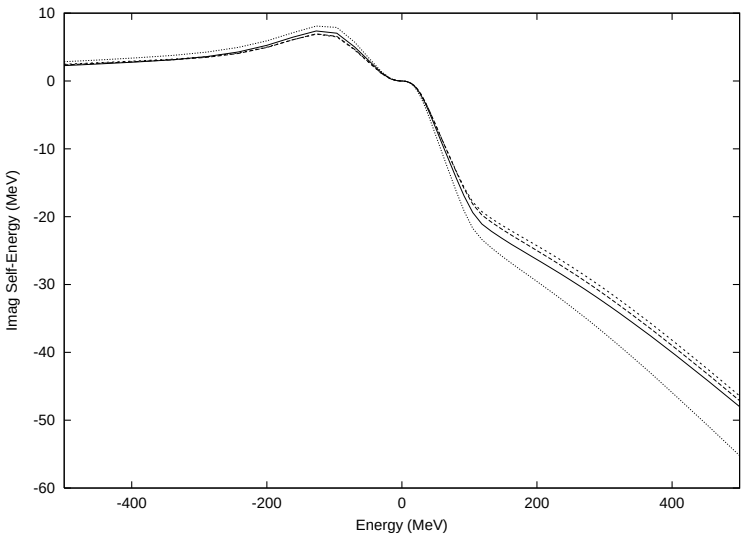

Figure 4.8: The imaginary part of the self-energy in the region near the Fermi energy for the iterations discussed in Table 4.1. The solid, dashed, and short-dashed represent the seventh, eighth, and ninth S wave iterations and the dotted represents the averaged inclusion of all waves discussed in the text.

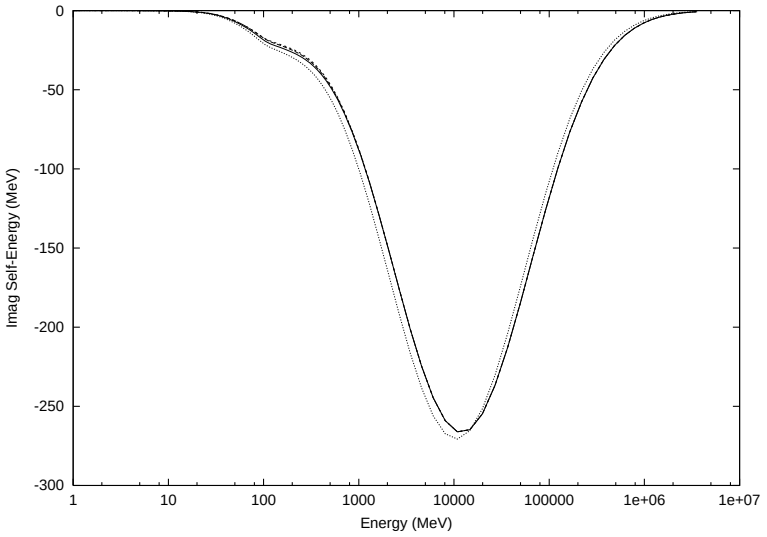

Figure 4.9: The high-energy behavior of the imaginary part of the self-energy for the iterations discussed in Fig. 4.8.

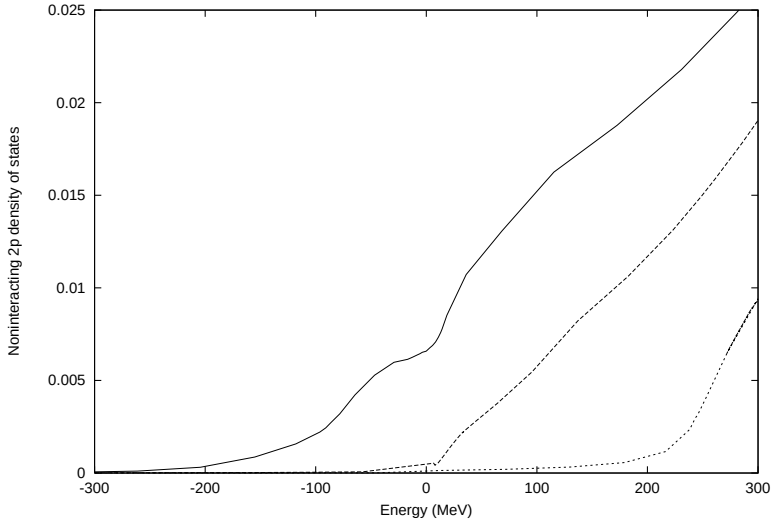

Figure 4.10: The dressed but noninteracting 2p density of states in MeV^{-1} as a function of $\Omega - 2\varepsilon_F$, which serves as an important numerical tool in designing the relative momentum mesh for the matrix inversion for the effective interaction.

4.2 Effective Interaction

A primary ingredient in the iteration scheme is the matrix inversion, required to yield the effective interaction. The choice of the q-mesh is critical to the accuracy of the effective interaction when using realistic sp propagators, as discussed in Section 3.3. When an appropriate mesh is chosen, it yields an accurate non-interacting 2p density of states $\{\rho_f^{II}\}$, and therefore can be expected to give the appropriate effective interaction. The ρ_f^{II} calculated with the q-mesh chosen in this work is shown in Fig.4.10 for center of mass momenta, $P = 0$ (full line), $2k_F$(dashed line), and 4.4 fm^{-1} (dotted line). In the case of zero center of mass momentum, the density of states at the Fermi momentum is proportional to $z^2(k_F)$. In the case of higher center of mass momenta, Pauli effects dominate near $2\varepsilon_F$, with a resulting sharp minimum. When the numerically calculated ρ_f^{II} contains all of these features in a reliable form, one can expect to obtain an accurate imaginary part of the effective interaction from the matrix inversion.

In Fig 4.11, the imaginary part of the diagonal elements of effective interaction

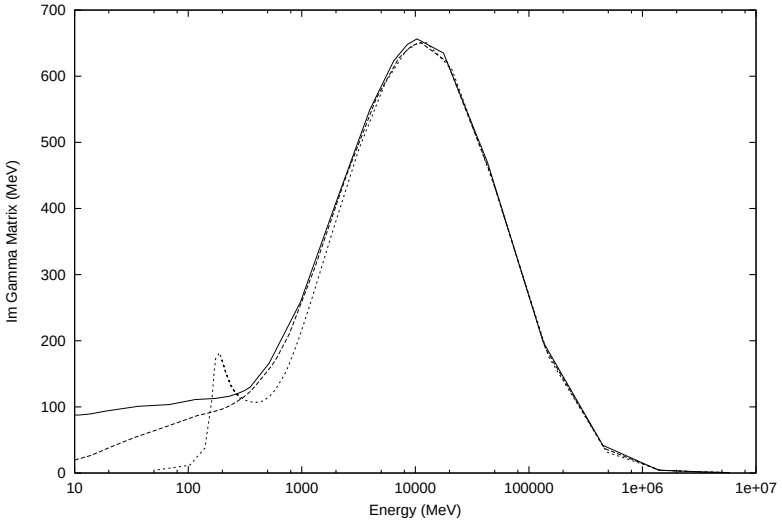

Figure 4.11: Diagonal elements of the imaginary part of the effective interaction as a function of $\Omega - 2\varepsilon_F$ at $q = 0.7$ fm^{-1} for $K = 0$ (solid), k_F (dashed), and 4.4 (dotted) fm^{-1} .

reflect phase space features at low energy, decreasing where ρ_f^{II} is restricted by Pauli effects near $2\varepsilon_F$. Due to the use of dressed propagators, there is no longer any lower limit below which the Im $\Gamma(K, q, \Omega)$ goes to zero. The dominant feature of the interaction is the pronounced peak at high energy, which occurs at 10 GeV for the Reid potential. Because this interaction can connect any sp momentum state to high-momentum states, which contribute strongly at high energies, there is little momentum dependence of this feature.

Figure 4.12 illustrates of the effect of each partial wave on the diagonal elements of the imaginary part of the effective interaction as a function of q for $K = 0$ and $\Omega = 2\varepsilon_F$. Once again, S waves provide a dominant effect at low momentum and high momentum, but near $q = 2$ fm^{-1}, the P contributions are of greatest magnitude. Self-consistent solution of the S waves has some effect on the matrix elements, comparing these results with those of Ref. [41]. The inclusion of the P waves as shown is not self-consistent. One may expect that self-consistency at this level will be important where they dominate, and the greatest contributions of the P waves occurs at the minimum

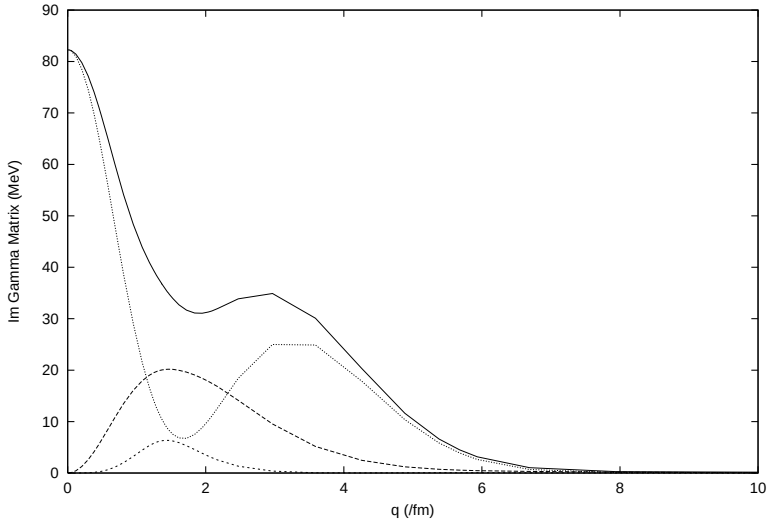

Figure 4.12: The contributions of the imaginary part of the effective interaction shown with all waves included (solid line), S waves (dotted), P wave (dashed), and D waves (short-dashed).

of the S contribution. Because the contributions of S and P waves appear in different regions, the extension of this work to include P and D waves self-consistently will require an additional gaussian at the self-energy level.

4.3 Self-Energy

Figure 4.13 illustrates the self-consistent solutions of the imaginary part of the self-energy including only S waves for energies below and above the Fermi energy for several different momenta. While the high-energy regime is not significantly different from a calculation using mean-field propagators, there are some important differences that come from using dressed propagators. Near the Fermi energy, there is an overall decrease of the imaginary part of the self energy as shown in Fig. 4.8. The effect of these low-lying states is therefore overestimated when mean-field propagators are used. At large negative energy, we assert that Im Σ becomes non-negligible but requires several iterations to achieve self-consistency.

In Fig. 4.14, the self-energy including only S waves is illustrated by the solid line and the self-energy including all partial waves is shown by the dashed line for $k = k_F$. Above the Fermi energy, the self-energy is dominated by the S wave contribution, but there is an important contribution below the high-energy peak from the other partial waves. Below the Fermi energy, the shape is not changed by the inclusion of higher waves, but the overall magnitude is increased by $\sim 20\%$ near the peak. These differences combine to generate a substantial contribution to the binding and sp spectrum as discussed in Section 4.1.

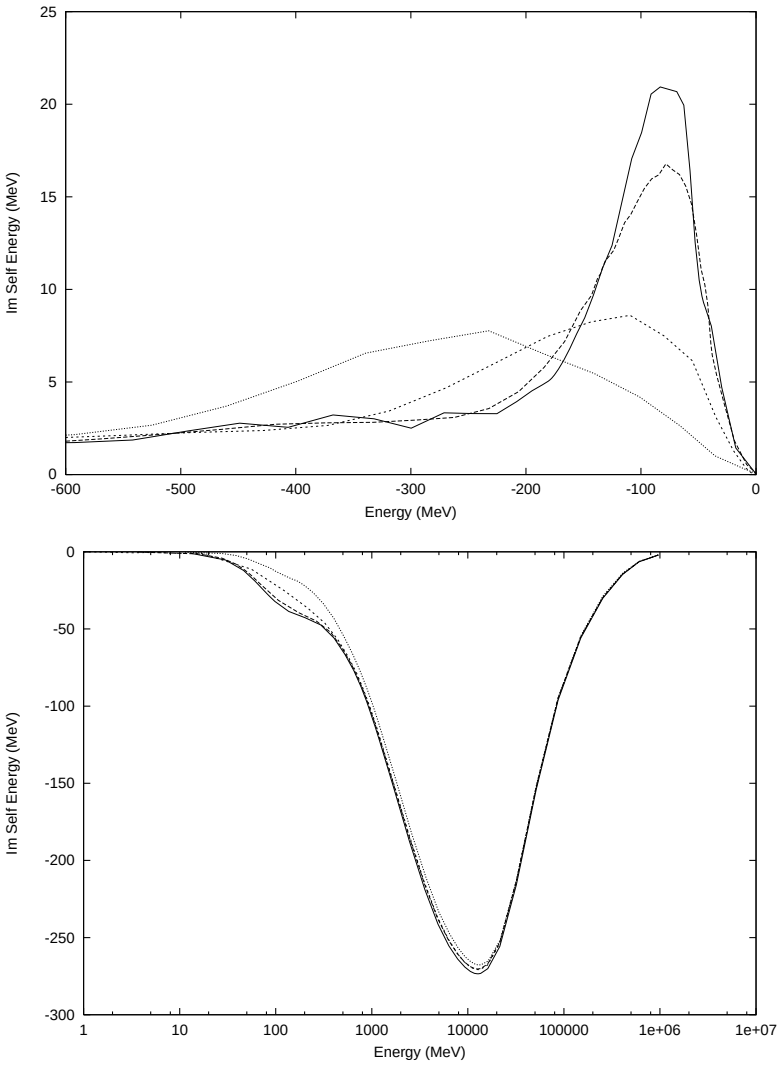

Figure 4.13: The imaginary part of the self-consistent self-energy including S waves only as a function of $\omega - \varepsilon_F$ for $k = 0$ (full line), 0.5 fm^{-1} (dashed), k_F (short $-$ dashed), and 2.1 fm^{-1} (dotted).

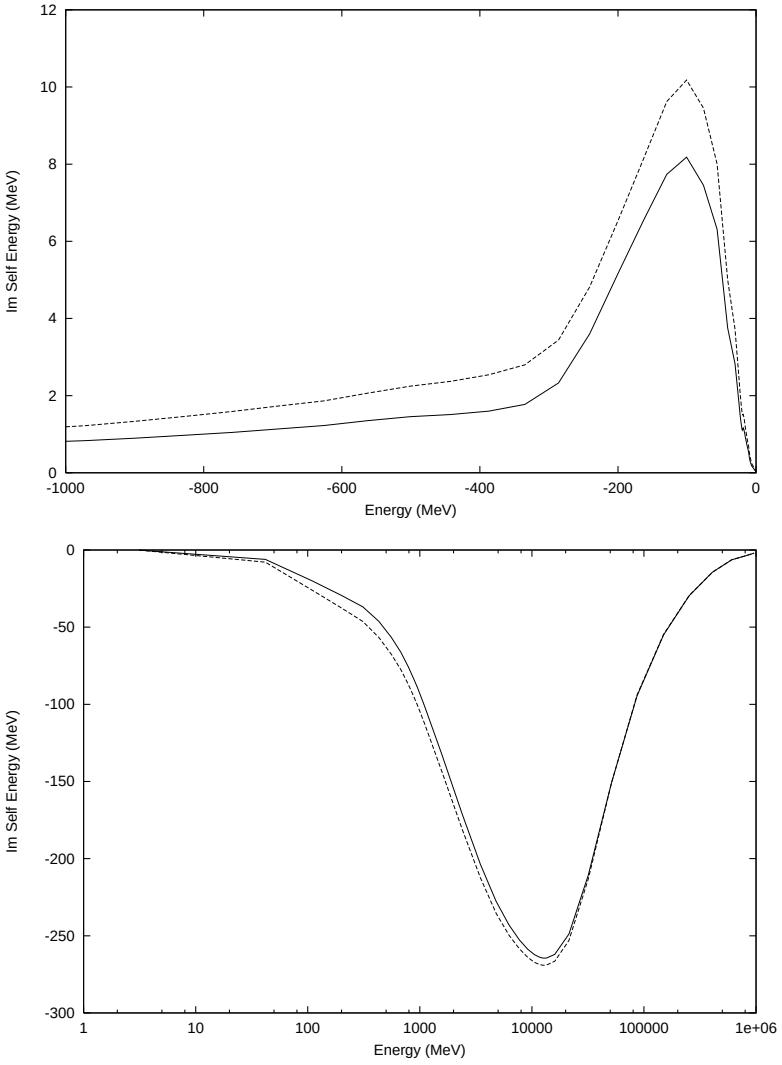

Figure 4.14: The imaginary part of the self-consistent self-energy as a function of $\omega - \varepsilon_F$ for $k = k_F$ including S waves only (solid) and with all partial waves (dashed).

4.4 Resulting Single-Particle Propagator

In Fig. 4.15, the self-consistent spectral functions including only S waves are shown for $k = \{0.5 \text{ fm}^{-1}, k_F, 2.1 \text{ fm}^{-1}\}$. In the upper part of the figure, the low-energy part of the spectral functions are displayed. The momentum dependence of the quasi-particle peaks is apparent, with the width of the peak vanishing for $k = k_F$ at the corresponding qp energy. Near the Fermi energy, the background contribution on both the hole and particle sides are enhanced near qp energies. The spectral function at high energy, also displayed in the bottom part of the figure on a logarithmic scale, exhibits very little momentum dependence, as first shown in Ref. [40]. A surprising momentum independence of the spectral function also arises at large negative energies in the self-consistent result. Such a tail is not obtained in spectral functions calculated from the mean-field as a starting point.

Integrating the spectral functions up to the Fermi energy yields the momentum distribution. In the top part of Fig. 4.16, the complete momentum distribution is shown on a linear scale. The occupation for momenta less than the Fermi momentum is about 4% higher than results that start with the mean-field [40], which agrees with the notion that such a treatment overestimates correlation effects. The self-consistent qp strength at the Fermi momentum is also higher by about 8%. In the bottom part of Fig. 4.16, the high-momentum tail is plotted on a logarithmic scale. The exponential decrease observed in results using the Paris potential [76] is confirmed by the self-consistent results presented here using the Reid potential.

The momentum distribution at high k originates from large negative energy contributions. Figure 4.17 illustrates the momentum content for low energies, corresponding to $\omega = \{-425\ , -250, -125, -75 \text{ MeV}\}$. A comparison with corresponding results starting from the mean-field [41] shows that the k-dependence at low energy is less pronounced with self-consistent results. This confirms the previous observation, related to Fig. 4.15, that low-energy spectral functions have little momentum

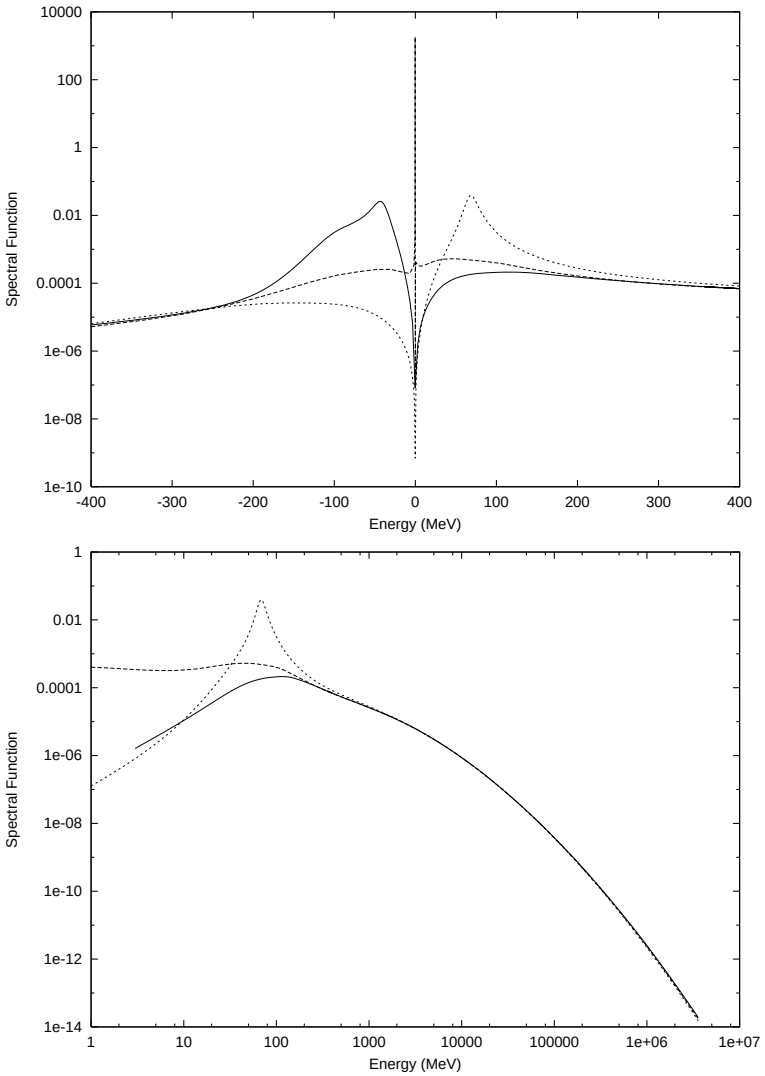

Figure 4.15: The spectral function, $S(k,\omega)$ as a function of $\omega - \varepsilon_F$, for sp momenta $k = 0$ (solid), k_F (dashed), and 2.1 fm^{-1}(dotted).

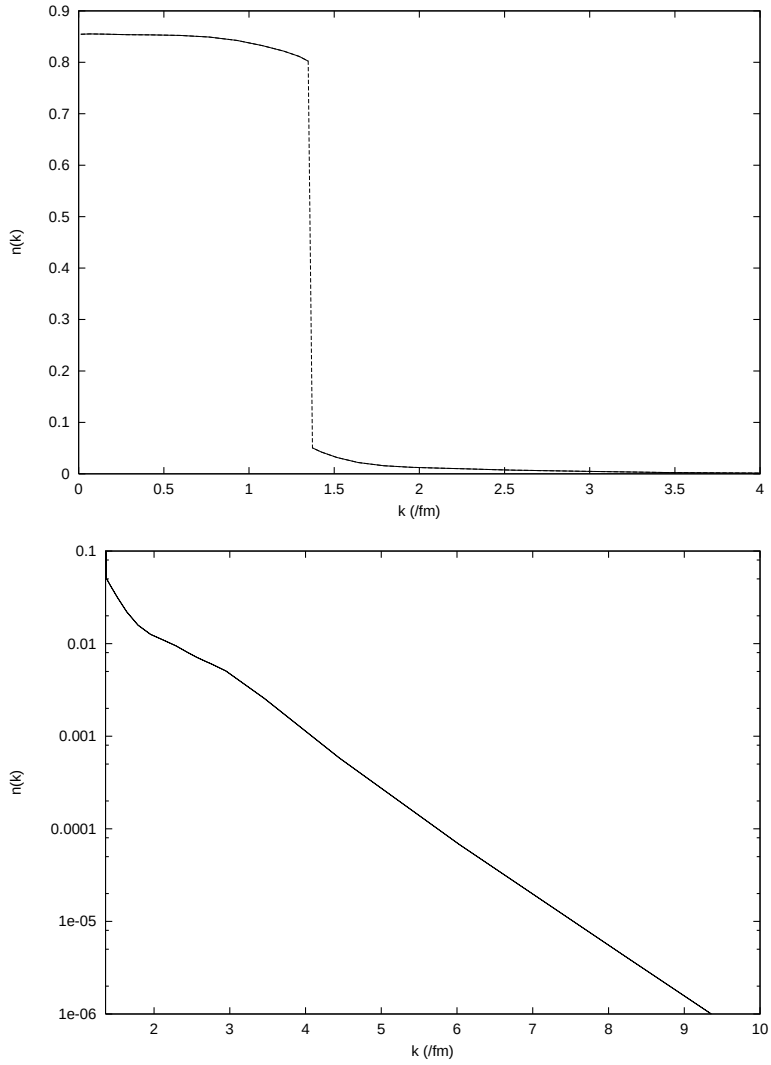

Figure 4.16: The momentum distribution on a linear scale (top half) and for momenta above k_F on a logarithmic scale (bottom half).

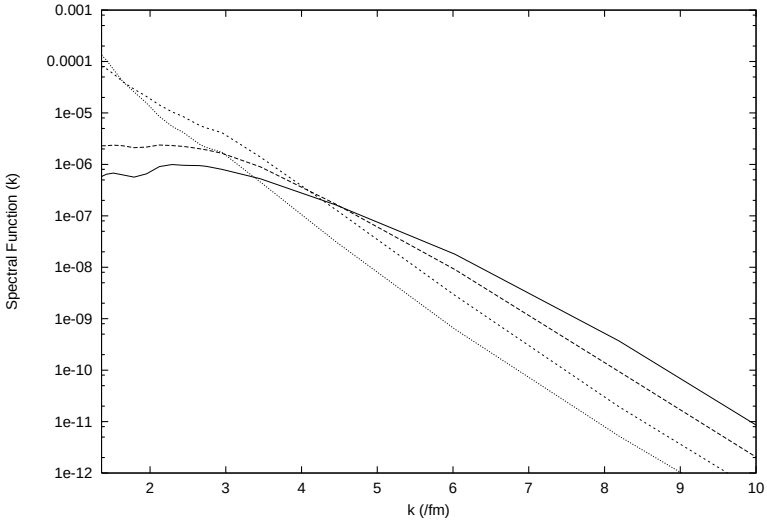

Figure 4.17: High-momentum components of the spectral function, $S(k,\omega)$, for $\omega = \{-425$ MeV (solid), -250 MeV (dashed), -125 MeV (short $-$ dashed), and -75 MeV (dotted) showing the low-energy high-momentum behavior.

dependence, which originates from the inclusion in the self-consistent results of low-energy states not reached in calculations starting with mean-field propagators. In the mean-field case, there is a k-dependent threshold energy below which 2h1p excitations do not occur. The spreading of the sp strength in the self-consistent calculation leads to the corresponding spreading of these more complicated states, yielding less k-dependence of these terms and the disappearance of the energy threshold.

For completeness, the resulting spectral functions are shown as a function of energy and momentum in Fig. 4.18. The figure can be compared with Figure 1 in Ref. [77] representing spectral functions calculated from the mean-field. In this type of plot, differences are difficult to distinguish. The general features of the spectral function and the behavior of its peak are similar in both calculations.

The sp wave function in coordinate space can be obtained from a Fourier-Bessel transform of the spectral function, as follows

$$S_\ell(r,r',\omega) = \frac{2}{\pi}\int dk\, k^2\, j_\ell(kr)\, j_\ell(kr')\, S(k,\omega) \tag{4.2}$$

At fixed $r' = 0$ for $\ell = 0$, the resulting wave function at energy, $\omega = -58$ MeV, is

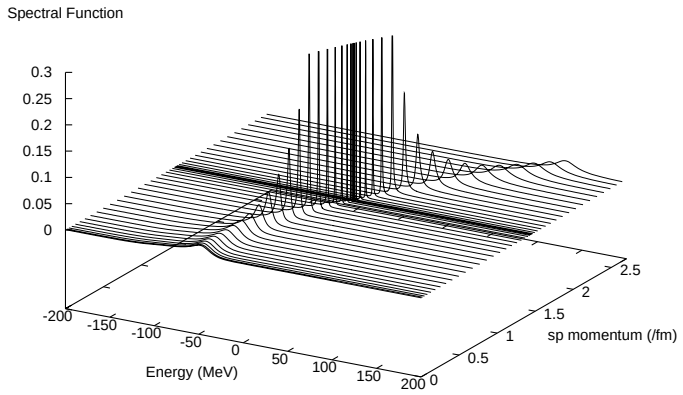

Figure 4.18: The momentum and energy dependence of the self-consistent sp spectral function for infinite nuclear matter at $k_F = 1.36$ fm^{-1}.

presented in Fig. 4.19. In this figure, the wavefunction is multiplied by r, so that one obtains a sin-wave for the mean-field case with a magnitude determined by the qp strength. For energies near ε_F, correlated wave functions are similar to the mean-field wave function, as the quasiparticle peak becomes a delta function at k_F. However, at low energy, wave functions do not resemble momentum eigenstates, but appear more localized. This is due to two features of the low-energy spectral function as a function of momentum. First, the quasiparticle peak is spread in momentum which creates damping of the wave function with increasing r, leading to a mean-free path at the corresponding energy. Second, the background is a smooth function sampling all momenta, and this produces an enhancement at small r. The resulting wave function appears localized in coordinate space, which is different from the mean-field model of these states. A similar localization is observed for natural orbits in $^{16}0$ including SRC [69].

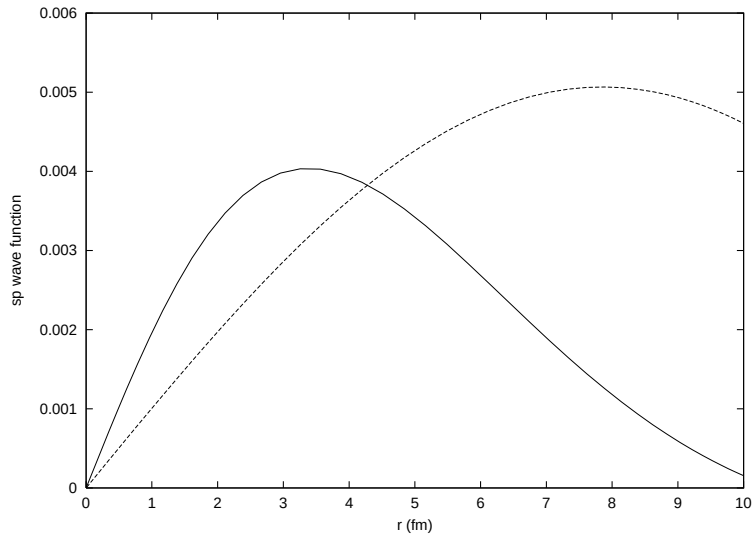

Figure 4.19: The sp wavefunction in coordinate space for an energy of -58 MeV (solid) as compared to the mean-field case (dashed).

4.5 Saturation Properties

The momentum distribution at high k is due to contributions at large negative energy, as illustrated in Fig. 4.17. These contributions are therefore also an important source of binding in the present calculation and reflect the influence of SRC. Referring to Table 4.1, the energy expectation values for self-consistent results at $k_F = 1.36$ fm^{-1} are determined including all the partial waves on top of a self-consistent S-wave calculation as discussed in Section 4.1. In this case, the relevant energies are

$$\begin{aligned} \mathrm{E}/A &= -14.76 \text{ MeV} \\ \mathrm{PE}/A &= -68.67 \text{ MeV} \\ \mathrm{KE}/A &= 53.91 \text{ MeV}. \end{aligned}$$

The kinetic energy can be compared with the results of Vonderfecht [40]. The self-consistent calculation yields about 7.5 MeV more kinetic energy.

In Table 4.2, self-consistent results for a higher density corresponding to $k_F = 1.45$ fm^{-1} are displayed. The first four lines contain results for the last iterations

iteration	ε_F	E/A	KE/A	PE/A	$\rho(\mathrm{fm}^{-3})$
4	-7.25	-9.10	60.19	-69.29	.203
5	-7.03	-8.80	60.96	-69.77	.203
6	-3.56	-7.88	60.01	-67.89	.202
7 S waves	-2.36	-7.18	60.07	-67.25	.203
all waves	-4.64	-12.30	67.83	-80.13	.207
average result	-7.32	-10.78	63.14	-73.92	.204

Table 4.2: The Fermi energy, energy per particle, kinetic energy, potential energy and particle density calculated for the last four iterations at $k_F = 1.45$ fm^{-1}.

including only S waves. The next line includes the calculation of the higher waves on top of the self-consistent S wave solution. Finally, the last line contains an approximation to the complete self-consistent result including all waves with an averaging procedure discussed in Section 4.1 for $k_F = 1.36$ fm^{-1}. As in Table 4.1, the particle numbers calculated for the self-consistent results agree with the exact particle number corresponding to 0.169 fm^{-3} for $k_F = 1.36$ fm^{-1} and 0.204 fm^{-3} for $k_F = 1.45$ fm^{-1}. This result is expected for any self-consistent solution as first shown in Ref. [60]. The results of this study have better than 1% agreement with this condition, suggesting satisfactory numerical accuracy of the present calculation.

The present results including only S waves have an uncertainty between iterations of about 1 MeV in kinetic and potential energies. Because the changes in these values tend to cancel almost completely, one may expect the resulting binding energy to have less uncertainty. The addition of higher waves on top of these self-consistent results can yield an estimate of the self-consistent solution including all waves but with greater uncertainty. Including only S waves, the energy per particle at $k_F = 1.45$ fm^{-1} is about 4.0 MeV higher than that obtained for the empirical saturation density. This result indicates that the saturation density of a self-consistent calculation must be near the empirical value since results at lower density are mostly in agreement. Furthermore, the value of the binding energy at the saturation density is expected to be about 15 MeV based on the results of Table 4.1. Both the saturation density and binding energy appear therefore consistent with empirical saturation properties. This

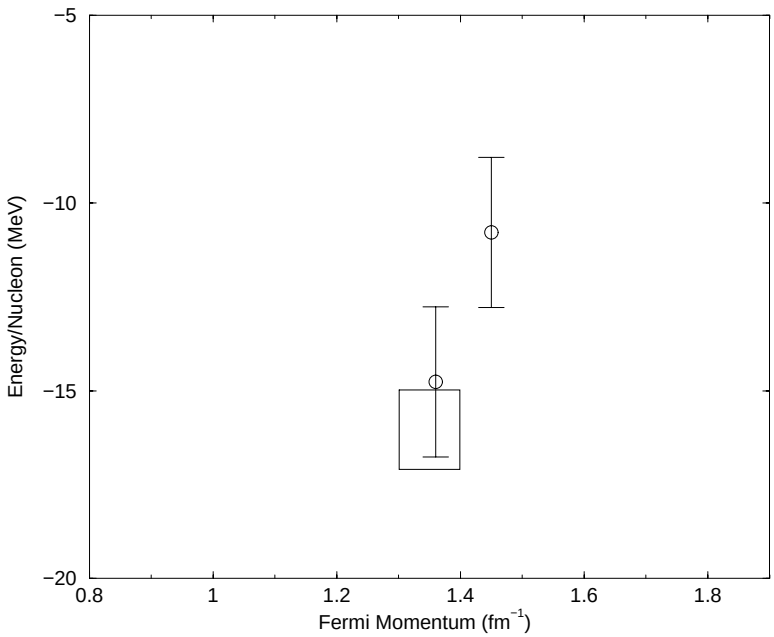

Figure 4.20: The energy per particle calculated at two densities corresponding to $k_F = 1.36$ fm^{-1} and $k_F = 1.45$ fm^{-1}. The saturation density calculated in the SCGF scheme with the Reid potential will occur at $k_F < 1.45$ fm^{-1}, possibly in agreement with empirical saturation properties.

is illustrated in Fig. 4.20, where the two points represent the self-consistent values of the energy per particle presented in Table 4.1 and Table 4.2 including an average treatment of the higher partial waves. The error bars represent the uncertainty resulting from this inclusion and are determined by the difference between the last two lines in these tables. The box in the figure represents the possible values of the empirical saturation properties.

The increase in kinetic energy present for the higher density system is substantially greater than that expected for the Fermi gas [68]. This increase must be due to SRC, and to study this effect one may consider high-momentum contributions to the binding energy. In Fig. (4.21) the contribution to the binding energy as a function of sp momentum is plotted for the densities corresponding to $k_F = 1.36$ fm^{-1}and $k_F = 1.45$ fm^{-1}. This figure illustrates that this increase in the kinetic energy due to high-momentum components cancels the potential energy between 3 and 5 fm^{-1}

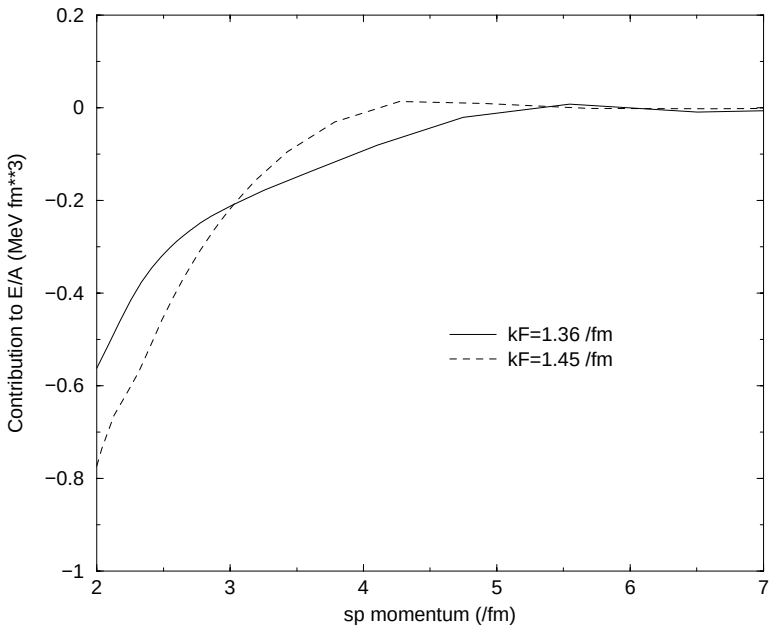

Figure 4.21: The high-momentum contribution to the energy per particle for $k_F = 1.36$ fm^{-1} (solid) and 1.45 fm^{-1} (dashed). This illustrates the source of saturation when SRC are considered self-consistently.

for $k_F = 1.45$ fm^{-1}. For the empirical saturation density, these momenta contribute substantially to binding. The loss of these high momentum terms in the energy per particle corresponds to the decrease in binding. This appears to be the mechanism by which the SRC provides saturation.

These results draw a different conclusion about saturation from that of previous work including three hole-line contributions in the BBG method. The saturation properties calculated with such a method [21] correspond to $k_F = 1.565$ fm^{-1} and $E/A = -16.18$ MeV suggesting the need for three-body forces to explain saturation. The present work focuses on the inclusion of SRC self-consistently, including the full energy-dependence of the nucleon propagator in the medium. This calculation does not include contributions from long-range correlations, whereas the three hole-line calculations of Ref. [21] include the third-order ring diagram. Ring-diagram contributions provide increasing attraction as a function of density [23], resulting in increased binding energy and therefore higher saturation density. The relevance of

such terms to finite nuclei has been questioned in Ref. [78]. Since infinite nuclear matter has been constructed to represent the interior of heavy nuclei, it is useful to note that long-range correlations can have only little effect on the value of the central density. The measured charge density at the origin for ^{208}Pb is dominated by 1s, 2s, and 3s proton shells. The depletion of the 1s and 2s must originate from SRC, while the 3s may be marginally affected by long-range correlations. One must therefore be able to explain saturation of heavy nuclei by including only SRC. It appears that the present scheme confirms these observations and may produce saturation properties in agreement with empirical values.

Chapter 5

Finite-Temperature Formalism

An introduction to a treatment which includes SRC self-consistently in the sp propagator of infinite nuclear matter at finite temperature, is presented in this chapter. More detailed discussions of the basic formalism can be found in Refs. [50],[52]-[54],[79], and [82]. Section 5.1 provides some background information about many-body systems at finite temperature. In Section 5.2, the case of the Green's function in a many-body setting is studied. The derivation of a similar diagrammatic expansion to the zero-temperature case is sketched in Section 5.3, and its implementation for the present study is developed in Section 5.4.

5.1 Background

At finite temperature, a system will be statistically distributed over all possible states, and a ground state expectation value is replaced by an average over the expectation values of an ensemble of states weighted by a statistical operator. To study such an ensemble average, we will choose the grand canonical distribution, characterized by the density operator,

$$\hat{\rho} = e^{-\beta(\hat{H}-\hat{N}\mu)}, \tag{5.1}$$

where $\beta = \frac{1}{kT}$ and μ is the chemical potential of the many-body system.

To determine the properties of a many-body system of interacting particles, we will use the Hamiltonian from Eq. (2.21) so

$$\hat{H} \mid \Psi_n^N \rangle = E_n \mid \Psi_n^N \rangle \tag{5.2}$$

and

$$\hat{N} \mid \Psi_n^N\rangle = \sum_k a_k^\dagger a_k \mid \Psi_n^N\rangle = N \mid \Psi_n^N\rangle, \tag{5.3}$$

where k includes spin and isospin quantities. The probability of the system being in state $\mid \Psi_n^N\rangle$, with energy E_n and N particles, is determined by the corresponding expectation value of the grand distribution operator and the grand partition function. Whereas in the zero-temperature case, expectation values of operators were evaluated with respect to the ground state with fixed N, any expectation value calculated at finite-temperature will now be calculated over the entire ensemble of all many-body states in the following way,

$$\langle \hat{O} \rangle = \frac{1}{Z} \sum_{nN} e^{-\beta(E_n - \mu N)} \langle \Psi_n^N \mid \hat{O} \mid \Psi_n^N \rangle \tag{5.4}$$

using

$$Z = \sum_{nN} e^{-\beta(E_n - \mu N)}, \tag{5.5}$$

where Z is the aforementioned grand partition function. One may rewrite the sum over states for the ensemble average in the following way,

$$\langle \hat{O} \rangle = \frac{tr(\hat{\rho}\hat{O})}{tr(\hat{\rho})}, \tag{5.6}$$

which can be evaluated in any basis. This illustrates that the density matrix yields any relevant ensemble average and completely determines the properties of the system.

5.2 Finite-Temperature Green's Functions

The sp propagator at finite temperature is defined by

$$g^T(k, k'; t - t') = -i\langle T[a_k(t) a_k^\dagger(t')] \rangle, \tag{5.7}$$

where the field operators are Heisenberg operators with time evolution governed by $\hat{H}$. Rewriting the propagator in the basis of good particle number and energy, one obtains

$$g^T(k, k'; t - t') = -i \sum_n e^{-\beta(E_n - \mu N)} \left\langle \Psi_n^N \middle| T[a_k(t) a_{k'}^\dagger(t')] \middle| \Psi_n^N \right\rangle . \tag{5.8}$$

To determine the dynamics of the system, one would like to be able to expand in a perturbation series for g^T, as was done for zero temperature. This is not possible with the above form. The diagrammatic expansion for g, and therefore its analysis by partial summation, stemmed from the differential form of the propagator as a solution to the Schrödinger wave equation. One may regard the density operator as governing propagation in imaginary time. Thus, it is useful to consider imaginary times, $\tau = it$, where t is real. The distribution operator, then, is a time evolution operator in imaginary time of $\Delta\tau = -\beta$. Solving for the properties of the system comes down to being able to evolve a state in imaginary time by $-\beta$. We will see that herein lies the key to solving for the sp propagator at finite temperature using the same tools as at zero temperature.

Applying this idea, one may consider the sp propagator of nuclear matter, for which $k = k'$, for $\tau > 0$,

$$\begin{aligned} g^<(k,\tau) &= -\frac{1}{Z}\sum_i \langle\Psi_i|\hat{\rho}a_k^\dagger(\tau)a_k(0)|\Psi_i\rangle \\ &= -\frac{1}{Z}\sum_i \langle\Psi_i|e^{-\beta(\hat{H}-\mu\hat{N})}e^{\tau(\hat{H}-\mu\hat{N})}a_k^\dagger e^{-\tau(\hat{H}-\mu\hat{N})}a_k|\Psi_i\rangle \\ &= -\frac{1}{Z}\sum_{ij} e^{(-\beta+\tau)(E_i-\mu N_i)}\langle\Psi_i|a_k^\dagger|\Psi_j\rangle e^{-\tau(E_j-\mu N_j)}\langle\Psi_j|a_k|\Psi_i\rangle, \end{aligned} \tag{5.9}$$

where Heisenberg field operators are evolved in imaginary time and i includes both particle number and energy. Since the energies in the exponents can be arbitrarily large, in order for the sum to converge each term must be finite, and the exponents must be negative in the case of large energies. From the first factor, this means that $\tau < \beta$, and from the second exponential factor one obtains $\tau > 0$. Likewise, for the $\tau < 0$ case,

$$g^>(k,\tau) = -\frac{1}{Z}\sum_{ij} e^{(-\beta-\tau)(E_i-\mu N_i)}\langle\Psi_i|a_k|\Psi_j\rangle e^{\tau(E_j-\mu N_j)}\langle\Psi_j|a_k^\dagger|\Psi_i\rangle \tag{5.10}$$

convergence conditions can be found to be $-\beta < \tau < 0$. The complete propagator g^T consists of the difference of $g^<$ and $g^>$. In considering the imaginary-time Green's

function of the noninteracting system one obtains

$$\begin{aligned} g_0^T(k,\tau_2-\tau_1) &= i\langle T[a_k(\tau_2)a_k^\dagger(\tau_1)]\rangle \\ &= i[\langle a_k(\tau_2)a_k^\dagger(\tau_1)\rangle - \langle a_k^\dagger(\tau_1)a_k(\tau_2)\rangle] \\ &= i[\theta(\tau_2-\tau_1)\frac{1}{1+e^{-\beta(\varepsilon(k)-\mu)}} \\ &- \theta(\tau_1-\tau_2)\frac{1}{1+e^{\beta(\varepsilon(k)-\mu)}}]e^{(\varepsilon(k)-\mu)(\tau_2-\tau_1)}. \end{aligned} \tag{5.11}$$

In this expression, the operators are time-evolved with $\hat{H}_0$ and the time-ordering operator is extended for imaginary times. The ensemble average of the density operator (the number of particles in state k) and the corresponding partition function can be evaluated explicitly, yielding the Fermi distribution functions in the expression above. Notice that for all momenta, both terms will contribute due to the nonzero value of the statistical factors for all k, and it is therefore possible to have both hole and particle contributions at the same momentum and corresponding energy. The value $\tau_2 - \tau_1$ is restricted to the $(-\beta, \beta)$ interval in which g^T is guaranteed to converge. Since the propagation depends only on the imaginary-time difference, one can choose to evolve the state from 0 to τ. Recalling that $tr[AB] = tr[BA]$, the Green's function can be expressed in the following equivalent forms, dropping the superscript T,

$$\begin{aligned} g(k,\tau) &= \frac{1}{Z}tr[\rho a_k^\dagger(\tau)a_k(0)] \\ &= \frac{1}{Z}tr[a_k(0)\rho a_k^\dagger(\tau)] \\ &= \frac{1}{Z}tr[a_k(0)a_k^\dagger(\tau-\beta)\rho] \\ &= g(k,\beta-\tau) \\ &= -g(k,\tau-\beta). \end{aligned} \tag{5.12}$$

This shows that the Kubo-Martin-Schwinger [59],[83] relation is obeyed,

$$g(k,\tau) = -g(k,\tau-\beta). \tag{5.13}$$

Restricting τ to the $(-\beta, \beta)$ interval, as is required to define time ordering of imaginary times, causes trouble when transforming to (k, ω) space, since the Fourier transform

requires an integral over all time. While the Green's function is only defined on this interval, it can be extended beyond this boundary in accordance with the quasiperiodic boundary condition that the KMS relation allows. The Fourier transform therefore becomes a Fourier series, where

$$g(k, i\omega_n) = \frac{1}{2}\int_{-\beta}^{\beta} d\tau e^{i\omega_n \tau} g(k, \tau). \tag{5.14}$$

The resulting Green's function has quantized values of ω_n which are known as the Matsubara frequencies [**?**]:

$$\omega_n = \frac{\pi}{\beta} n \tag{5.15}$$

where n is odd for the case of fermions.

As the Lehmann representation was useful in the zero-temperature case, we may now be interested in deriving a corresponding representation of $g(k, \omega_n)$ first obtained by Landau [**?**]. Inserting Eq. (5.7) in Eq. (5.14), one obtains

$$g(k, i\omega_n) = \frac{1}{2}\int_{-\beta}^{0} d\tau e^{-i\omega_n \tau} \langle a_k^\dagger(\tau) a_k(0)\rangle - \frac{1}{2}\int_{0}^{\beta} d\tau e^{i\omega_n \tau} \langle a_k(\tau) a_k^\dagger(0)\rangle. \tag{5.16}$$

Inserting complete sets of many-body states chosen as eigenvectors of the density operator and restoring the particle-number and energy representation, $\{|E_n, N\rangle\} = \{|\Psi_n^N\rangle\}$, one obtains the following result:

$$\begin{aligned}
\langle a_k(\tau) a_k^\dagger(0)\rangle &= \frac{1}{Z} tr\{\rho a_k(\tau) a_k^\dagger(0)\} \\
&= \frac{1}{Z}\sum_{m,N} \langle \Psi_n^N | e^{-\beta(H-\mu N)} e^{\tau(H-\mu N)} a_k e^{-\tau(H-\mu N)} a_k^\dagger | \Psi_n^N\rangle \\
&= \frac{1}{Z}\sum_{m,n,N} \langle \Psi_n^N | a_k | \Psi_n^{N+1}\rangle \langle \Psi_n^{N+1} | a_k^\dagger | \Psi_n^N\rangle e^{-\beta(E_m - \mu N)} e^{\tau(E_m - E_n + \mu)}
\end{aligned} \tag{5.17}$$

Using such expressions in $g(k, \tau)$, Fourier transformation yields a useful representation of the $g(k, i\omega_n)$ with the same spectral information as Eq. (2.7), with the notable exception that it is restricted to describing imaginary times and frequencies:

$$g(k, i\omega_n) = \frac{1}{Z}\sum_{m,n,N} e^{-\beta(E_m^N - \mu N)} \{ \frac{|\langle \Psi_n^{N+1} | a_k^\dagger | \Psi_m^N\rangle|^2}{i\omega_n - E_n^{N+1} + E_m^N + \mu} + \frac{|\langle \Psi_n^{N-1} | a_k | \Psi_m^N\rangle|^2}{i\omega_n - E_m^N + E_n^{N-1} + \mu} \}. \tag{5.18}$$

A finite-temperature spectral function can be defined as follows,

$$S(k,\omega) = \sum_{nmN} \langle \Psi_m^{N-1} | a_k^\dagger | \Psi_n^N \rangle \langle \Psi_n^N | a_k | \Psi_m^{N-1} \rangle \delta(E_n - E_m - \mu - \omega). \tag{5.19}$$

Defining the distribution function,

$$f(\omega) = \frac{1}{1 + e^{\beta(\omega - \mu)}}, \tag{5.20}$$

one can express Eq. (5.18) using (5.19) and (5.20), producing the following form,

$$g(k, i\omega_n) = \int d\omega' S(k,\omega') \{ \frac{f(\omega')}{i\omega_n - \omega'} + \frac{1 - f(\omega')}{i\omega_n - \omega'} \}. \tag{5.21}$$

With this form, $g^>$ and $g^<$ are expressed as follows,

$$\text{Im } g^>(k,\omega) = (1 - f(\omega)) S(k,\omega) \tag{5.22}$$

$$\text{Im } g^<(k,\omega) = f(\omega) S(k,\omega). \tag{5.23}$$

Using these expressions, the imaginary-energy propagator obeys

$$g(k, i\omega_n) = \int d\omega' \frac{\text{Im } g(k,\omega')}{i\omega_n - \omega'}. \tag{5.24}$$

While dealing with imaginary time is sensible for the purpose of calculating the density matrix and partition function, one must discuss issues like the sp excitation spectrum in terms of real energies. To lift the imaginary-time/imaginary-energy restriction, it is fruitful to consider the analytic continuation $i\omega_n \to \omega$, where ω includes all complex values. This step yields the Landau representation of the finite temperature Green's function [**?**]:

$$g(k,\omega) = \int d\omega' S(k,\omega') \{ \frac{f(\omega')}{\omega - \omega' - i\eta} + \frac{1 - f(\omega')}{\omega - \omega' + i\eta} \} \tag{5.25}$$

The new $g(k,\omega)$ is clearly identical to the old one at its infinite set of defined points along the imaginary-ω axis, $\{i\omega_n\}$. Carlemann's theorem [84] asserts that there is only one function which can be identical to Eq. (5.18) at its defined points, $\{i\omega_n\}$,

analytic everywhere with the possible exception of the real axis, and tending to zero at infinite distance from the origin. The new function $g(k,\omega)$, Eq. (5.25), will therefore have these properties. If we determine $g(k,i\omega_n)$ from diagrammatical methods, we can obtain the propagator for real times and energies with the spectral function common to both Eq. (5.21) and Eq. (5.25). The resulting $g(k,\omega)$ has a branch cut at the real axis with the discontinuity $g^{>}(k,\omega) - g^{<}(k,\omega) = S(k,\omega)$. We can also note that $g(k,\omega)$ can be Fourier transformed to find real-time Green's functions. Therefore, real-time evolution and real-energy excitations can be explored by solving for imaginary-time evolution.

5.3 Finite-Temperature Dynamics

In order to illustrate the value of the imaginary-time propagator in finite-temperature Green's function theory, one should recall the form of the density operator. Differentiating Eq. (5.1) with respect to β, yields the Bloch equation [85],

$$\frac{\partial\hat{\rho}(\beta)}{\partial\beta} = -(\hat{H} - \mu\hat{N})\hat{\rho}(\beta). \tag{5.26}$$

Just as the Schrödinger wave equation determines the time evolution of a wave function, the Bloch equation determines evolution of the system in imaginary time. The Bloch equation is in a form that can be analyzed at finite temperature in the same way as the Schrödinger wave equation in the zero-temperature case.

We define the operator $\widetilde{U}(\beta)$ such that

$$\hat{\rho}(\beta) = e^{-\beta(\hat{H}_0 - \mu\hat{N})}\widetilde{U}(\beta). \tag{5.27}$$

The imaginary-time evolution operator in the interaction picture obeys the following differential equation

$$\frac{\partial\widetilde{U}(\beta)}{\partial\beta} = -\hat{H}_1(\beta)\widetilde{U}(\beta), \tag{5.28}$$

which makes it particularly suitable for iterative solution. This introduces a finite-temperature analog to the interaction picture. Operators in this picture will be

evolved in imaginary time with the noninteracting Hamiltonian. The corresponding $\hat{H}_1(\tau)$ can then be defined by

$$\hat{H}_1(\tau) = e^{(\hat{H}_0 - \mu\hat{N})\tau} \hat{H}_1 e^{-(\hat{H}_0 - \mu\hat{N})\tau}. \tag{5.29}$$

Integrating the differential equation, Eq. (5.28) yields

$$\begin{aligned} \tilde{U}(\beta) &= 1 - \int_0^\beta dt_1 \hat{H}_1(\tau_1)\tilde{U}(\tau_1) \\ &= 1 - \int_0^\beta d\tau_1 \hat{H}_1(\tau_1) + \int_0^\beta d\tau_1 \int_0^{\tau_1} d\tau_2 \hat{H}_1(\tau_1)\hat{H}_1(\tau_2) - \cdots \\ &= \sum_{n=0}^{\infty} \frac{(-1)^n}{n!} \int_0^\beta d\tau_1 \cdots \int_0^\beta d\tau_n T[\hat{H}_1(\tau_1)\cdots\hat{H}_1(\tau_n)] \end{aligned} \tag{5.30}$$

This illustrates that the imaginary-time evolution in the interaction picture can be evaluated using Dyson's expansion, in analogy to the zero-temperature case. Substituting the second-quantized Hamiltonian into this expression and taking the ensemble average [52] yields a sum that can be treated diagrammatically. This diagrammatic expansion consists of interactions connected by all possible contracted field operators, or imaginary-time Green's functions, which is expressed diagrammatically as in the zero-temperature case by Fig. 2.1.

Using a similar argument as in the zero-temperature case, one expects the infinite sum of ladder diagrams to be the relevant set of diagrams to consider in the effective interaction. Therefore, the same diagrams will be considered in the finite-temperature case as in the zero-temperature case. As a result, we can explore a similar self-consistency scheme between the ladder equation for the effective interaction and the Dyson equation for the sp propagator as at zero-temperature. A new dictionary will not be required for analyzing the diagrams, but the new character of $g_0(k, i\omega_n)$ including Fermi distributions and omitting the Fermi energy restriction of hole and particle propagation, will alter the analytic expression of the corresponding terms.

The physical interpretation of the results is also somewhat different from the zero-temperature case. Considering the propagator along the imaginary time or energy axis only, the solution to the self-consistent scheme yields the one-body density matrix

at the chosen temperature. The partition function at this level of approximation is also obtained, and therefore all bulk and thermodynamic properties of the system in thermal equilibrium can be determined. Since the imaginary time propagator of the system can be analytically continued to the real axis, one is able to obtain similar information as in the zero-temperature case, such as the sp excitation spectrum and spectral functions. For the finite-temperature case, self-consistency of the sp Green's function will be the goal of the iteration scheme as in the zero-temperature case.

Since Dyson's equation has a similar diagrammatic expansion as in the $T = 0$ case, one obtains

$$\begin{aligned} g(k, i\omega_n) &= g_0(k, i\omega_n) + g_0(k, i\omega_n)\Sigma(k, i\omega_n)g(k, i\omega_n) \\ &= \frac{1}{g_0(k, i\omega_n)^{-1} - \Sigma(k, i\omega_n)} \\ &= \frac{1}{i\omega_n - \epsilon(k) + \mu - \Sigma(k, i\omega_n)} \end{aligned} \tag{5.31}$$

as a means of determining the imaginary-time propagator in terms of an imaginary-energy self-energy. Therefore, finding the effective potential, or self-energy, from diagrammatic methods will yield the corresponding sp Green's function.

Although Dyson's equation, Eq. (5.31), and the self-energy are only defined for $\{i\omega_n\}$, $\Sigma(k, i\omega_n)$ can be analytically continued to all complex ω because it also has a Landau representation just like the propagator, Eq. (5.25). Likewise, a similar analytic continuation for 2p energies exists for the effective interaction, Γ. While the solution along the imaginary axis is the key to using the diagrammatic methods for these studied quantities, we will no longer use the discrete Matsubara energies in their evaluation, but instead we employ continuous real energies.

5.4 Self-Consistent Solution at Finite-Temperature

We will briefly repeat the steps in the iteration scheme needed to solve for the self-consistent Greens' function at finite temperature, which was presented for the zero-temperature case in Section 2.5.

1. The effective interaction will again be solved in a partial-wave expansion just as in the zero-temperature case (See Fig. 2.5):

$$\begin{aligned}\langle k_r|\Gamma^{JST}_{LL'}(P,\Omega)|k'_r\rangle &= \langle k_r|V^{JST}_{LL'}|k'_r\rangle \\ &+ \frac{1}{2}\frac{1}{(2\pi)^3}\sum_{L''}\int dq\, q^2\langle k_r|V^{JST}_{LL''}|q\rangle g^{II}_{f,T}(q,P,\Omega)\langle q|\Gamma^{JST}_{L''L'}(P,\Omega)|k'_r\rangle,\end{aligned} \tag{5.32}$$

where the dressed but noninteracting 2p propagator at finite temperature, $g^{II}_{f,T}$, is given by

$$\begin{aligned}g^{II}_{f,T}(q,P,\Omega) &= \frac{1}{2\pi}\langle\int d\omega\, g(\overrightarrow{P}+\overrightarrow{q},\frac{\Omega}{2}+\omega)g(\overrightarrow{P}-\overrightarrow{q},\frac{\Omega}{2}-\omega)\rangle_\theta \\ &= \langle\int d\omega\int d\omega'\,(1-f(\omega)-f(\omega'))\frac{S(\overrightarrow{P}+\overrightarrow{q},\omega)S(\overrightarrow{P}-\overrightarrow{q},\omega')}{\omega+\omega'-\Omega}\rangle_\theta.\end{aligned} \tag{5.33}$$

To obtain the final equality, a Matsubara summation must be performed as discussed in Appendix A of Ref. [86]. Note that the angle averaging represented by the notation, $\langle\,\rangle_\theta$, is required for the use of the partial-wave basis, just as in the zero-temperature case.

2. The diagonal elements of the effective interaction are used to calculate the imaginary part of the self-energy at finite temperature (See Fig. 2.6):

$$\text{Im }\Sigma(k,\omega)=\frac{1}{(2\pi)^4}\int d^3q\int d\omega'\,S(q,\omega')[f(\omega')+g(\omega+\omega')]\,\text{Im }\langle k,q|\Gamma(P,\Omega)|k,q\rangle. \tag{5.34}$$

The two statistical factors, f and g, arise from a partial fractions treatment of the energy denominators in order to perform the Matsubara sum as presented in Appendix A of Ref. [86]. The factor f corresponds to the Fermi statistical function, defined in Eq. (5.20), and the factor g represents the Bose statistical function of a 2p energy, where the boson distribution function is

$$g(\Omega)=\frac{1}{e^{\beta(\Omega-2\mu)}-1}. \tag{5.35}$$

The structure of the Bose function includes a pole at twice the chemical potential which is canceled by a corresponding numerator in the effective interaction [47].

3. Finally, the form of the sp propagator, after the appropriate analytic continuation, is unchanged from the zero-temperature case (See Fig. 2.7):

$$g(k,\omega) = g_0(k,\omega) + g_0(k,\omega)\Sigma(k,\omega)g(k,\omega) \tag{5.36}$$

$$= \frac{1}{\omega - \frac{k^2}{2m} - \Sigma(k,\omega)} \tag{5.37}$$

The start of the iteration process requires a sp propagator ansatz. As a first choice, we will study a temperature of 5 MeV. Considering the self-energies presented in Ref. [86], it appears that the zero-temperature solution at normal density may be a good starting point of the iteration scheme. At this temperature, we will see in Chapter 6 that the finite-temperature effects are mild but noteworthy.

Chapter 6

Results and Applications at Finite Temperature

Finite-temperature calculations of the self-energy have been performed by several groups [86],[87]-[91], and [64] with the goal of gaining insight into heavy ion-collision experiments which sample a large range of temperatures and densities. These theoretical studies explore the equilibrium properties of finite-temperature nuclear matter while Ref. [91] includes nonequilibrium effects by applying transport methods in the Boltzmann-Uehling-Uhlenbeck scheme. Again, the need to go beyond the mean-field description is motivated by electron scattering experiments for the low temperature limit near saturation density. Quasiparticle properties at saturation density display a strong temperature dependence [90]. A Brueckner study in nuclear matter at $T = 10$ MeV [88] finds an increase in qp energy spectrum and an expected additional depletion of the momentum distribution below the Fermi momentum. Also, a general decrease in the effect of SRC is observed with respect to the zero-temperature case corresponding to the reduced effect of the Pauli principle at finite temperature. An attempt to solve for the characteristics of nuclear matter at finite temperature self-consistently is presented in Ref. [64] for a semi-realistic separable interaction. At lower density, the effect of pairing correlations must be included in calculations using Green's function methods [91].

For a noninteracting Fermi gas of nucleons finite temperature effects are going to dominate above the Fermi temperature, given by

$$\frac{\hbar^2 k_F^2}{2m} = k_B T_F. \tag{6.1}$$

At normal density this corresponds to a Fermi temperature of $T_F = 4.3 * 10^{11}$K, or 37 MeV. Accordingly, an atomic nucleus may be approximated as a highly degenerate

Fermi gas with a temperature small compared to the Fermi temperature. Finite-temperature effects must be considered if one is interested in nuclei in hot plasmas and inside stars. In this study, a temperature of 5 MeV is chosen to study self-consistency aspects of sp properties. This temperature is sufficiently far from the Fermi temperature that quantum effects are still relevant.

In this chapter, the results of the SCGF iteration are presented for $k_F = 1.36$ fm^{-1} at $T = 5$ MeV. The starting point for this self-consistent calculation is provided by the results of Vonderfecht using mean-field propagators [40] as in the zero-temperature case. Section 6.1 will illustrate the convergence of important single-particle properties, and the following sections will contain converged results for the effective interaction (Section 6.2), the self-energy (Section 6.3), and the sp spectral function (Section 6.4).

6.1 Self-Consistency at Finite Temperature

This section illustrates the convergence properties of the self-energy parameters and related quantities. Figure (6.1) contains the peak values of G_2 and G_3 for various iteration steps. These gaussians describe the imaginary part of the self-energy in the particle and hole domain near μ (See Section 3.1 for the zero-temperature equivalent). The convergence was not pursued as far as in the zero-temperature study, but the extension to a more complete self-consistency is straightforward. It will be seen that not all parameters differ greatly from the zero-temperature case. The high energy peak for instance is not noticeably altered (See Section 6.3).

The sign of the peak values shown in Fig. 6.1 of the representative gaussians is altered with respect to the zero-temperature case for $\omega > \mu$. The finite-temperature Im Σ is positive at all energies because finite-temperature methods are implemented using only forward going propagation in the effective interaction using the Baym-Kadanoff boundary condition [53]. At zero temperature, 2h propagation is treated as two particles propagating backward in time in the Galitskii-Feynman approach. The only time-ordering necessary for a finite-temperature study is the retarded case, and

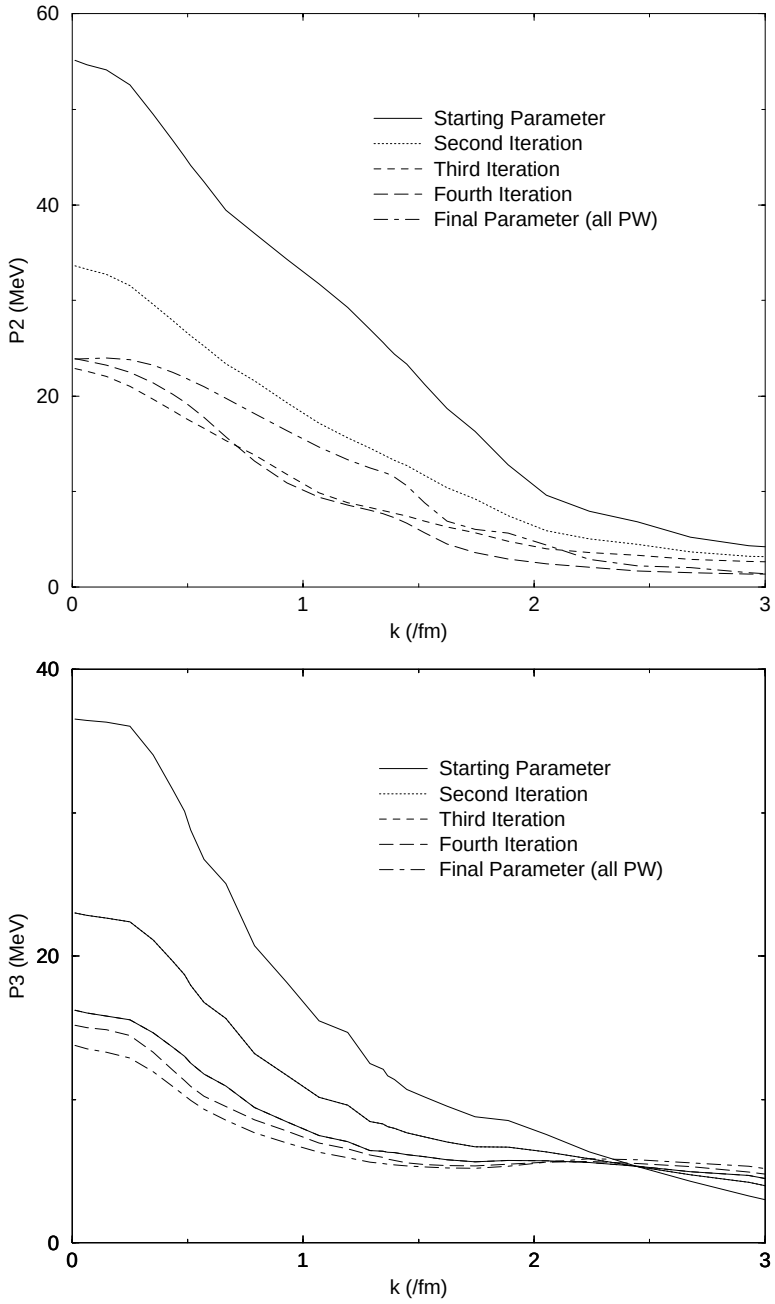

Figure 6.1: Parameters for the peak value of G_2 (above) and G_3 (below), which describe the imaginary part of the self-energy near the chemical potential in the particle and hole domains, respectively.

the resulting imaginary part of the self-energy is positive everywhere [86].

The greatest difference between the zero- and finite-temperature solution for Im Σ is in the values of G_2 and G_3 shown in Fig. 6.1, which decrease by as much as 40% with respect to the zero-temperature solution. This result can be compared with that of the Rostock group using a mean-field starting point and calculating the effective interaction with a separable version of the Paris potential [92]. While differences between the results of Ref. [92] and those of the present work exist due to the use of different potentials, the Rostock group also finds a decrease of contributions to the self-energy near the chemical potential with increasing temperature. As in Ref. [92], we find that for energies greater than 600 MeV, the imaginary part of the self energy has no substantial difference from the zero-temperature case. A notable difference between the two sets of results occurs in the particle domain near the chemical potential. The Rostock group finds that the contribution in this region forms a dramatic, pole-like peak structure at low temperature. This temperature corresponds to the critical temperature, $T_c \sim 3$ MeV, signalling the onset of superfluidity in this calculation. This structure is absent in the present results. This absence is no surprise since such a pairing instability is not evident even at zero-temperature when dressed propagators are used.

The particle density for the Fermi momentum considered is reproduced precisely for all iterations. The particle density is given by

$$\rho = \frac{4}{(2\pi)^3} \int d^3k \int d\omega \, S(k,\omega) f(\omega). \tag{6.2}$$

This expression is used as a condition which is used to determine the chemical potential, μ, at finite temperature. Therefore, satisfying particle number conservation is not a measure of the level of self-consistency of the calculation.

The behavior for various iteration steps of the sp potential and the imaginary part of the self-energy at the qp energy, are shown in Figs. 6.2 and 6.3. The sp potential determines the qp spectrum, identifying the location of the peak of the spectral function. This peak is determined in the same way as in the zero-temperature case,

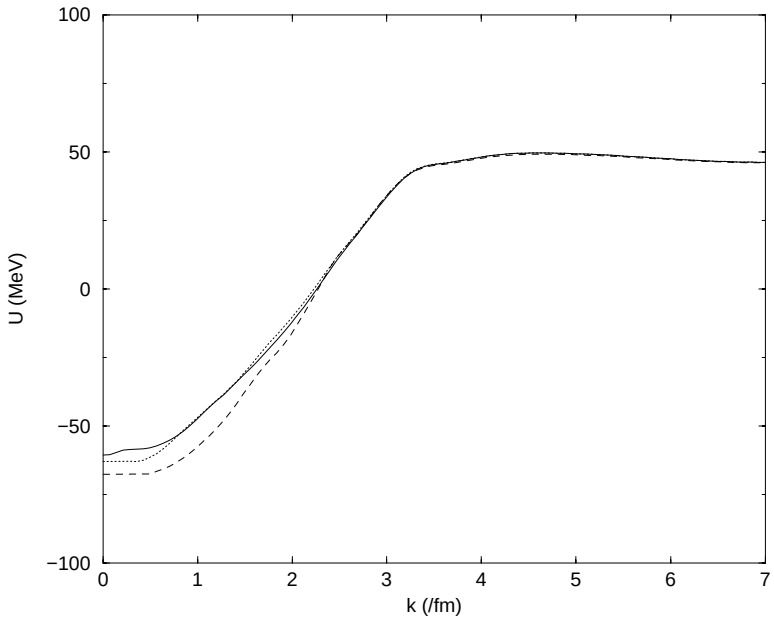

Figure 6.2: The single-particle potential as a function of momentum is shown for the third iteration (solid), fourth iteration (dotted), and last iteration (dashed).

given by Eq. (3.5). Figure 6.2 illustrates the sp potential when all partial waves are included in the calculation. This result can be compared with the final result in Fig. 4.5 at $T = 0$ and the same density. One observes that the difference between the zero-temperature and finite-temperature result are minor at this temperature. This observation is also made in Ref. [86]. The imaginary part of the self-energy at the qp energy, displayed in Fig. 6.3, is reduced with respect to the zero-temperature case with the exception of momenta very near the Fermi momentum ($k \simeq k_F$). The nonzero value of the on-shell value of the imaginary part of the self-energy, $I(k_F)$, is also of numerical importance. This implies that all spectral functions have a finite width and therefore can easily be represented numerically for all momenta.

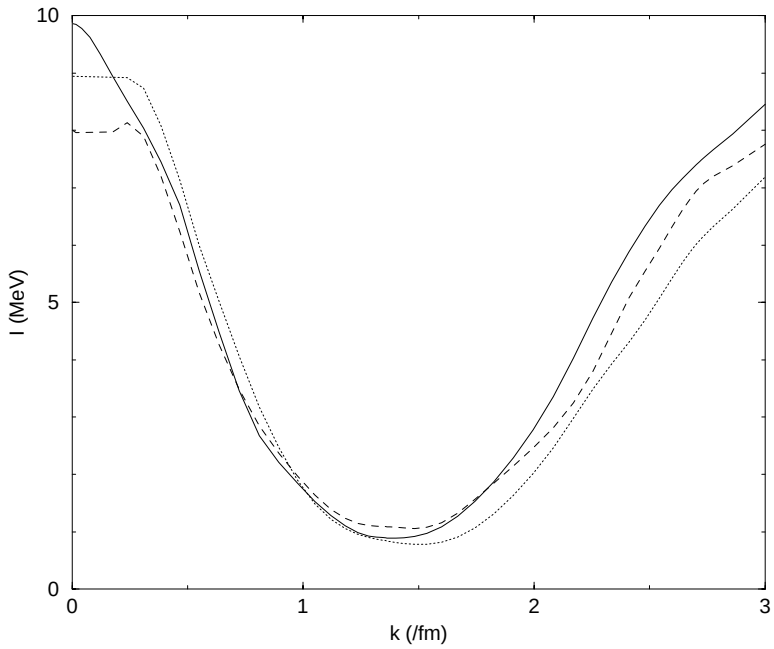

Figure 6.3: The on-shell value of Im $\Sigma(k,\omega)$ as a function of momentum is shown for the third iteration (solid), fourth iteration (dotted), and last iteration (dashed).

6.2 The Effective Two-Body Interaction at T=5 MeV

The most notable difference for the effective interaction between the zero and the finite temperature case occurs at low center of mass momentum. For zero center of mass momentum, there is no Pauli-blocking effect in the noninteracting 2p density of states for the zero-temperature case. However, for finite temperature, there is always some statistical factor which affects the noninteracting 2p density of states and, consequently, weakens the effective interaction. In Fig. 6.4, the noninteracting 2p density of states ($\rho^{II}_{f,T}$), as defined in Eq. (5.33), for zero center of mass momentum is shown for temperatures of 0 and 5 MeV. The statistical factor responsible for the vanishing of $\rho^{II}_{f,T}$ and Im Γ (shown in Fig.6.5) at 2μ mimics the Pauli blocking of the zero-temperature case for finite total momenta. Consider the following form of the 2p statistical factor near 2μ in the case of zero center of mass momentum in the

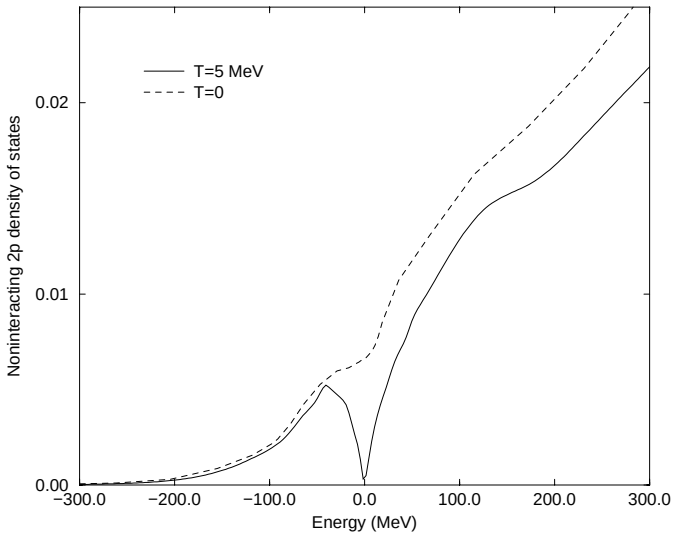

Figure 6.4: The noninteracting two-particle density of states in MeV^{-1} as a function of $\Omega - 2\mu$ is shown for solutions at 0 and 5 MeV.

free-particle approximation:

$$\begin{aligned} 1 - f(\omega_1 - \mu) - f(\omega_2 - \mu) &= 1 - \frac{1}{1 + \exp(\frac{\omega_1 - \mu}{T})} - \frac{1}{1 + \exp(\frac{\omega_2 - \mu}{T})} \\ &\propto k_F^2 - m k_B T - q^2, \end{aligned} \tag{6.3}$$

in the limit of $\omega_1 \to \mu$ and $\omega_2 \to \mu$. In obtaining this result, the first order in the Taylor expansion of the exponential was retained, and the sp energies of $\frac{q^2}{2m}$, for the free-particle case, were used. In the zero total momentum case, it is useful to note that q corresponds to both the sp momentum and the relative momentum of the particles. The source of the behavior near 2μ is clear, since this is the region where the preceding approximation is most valid. Recalling the well-known form [52] of the Pauli factor

$$Q = k_F^2 - (\frac{K}{2})^2 - q^2 \tag{6.4}$$

for $\frac{K}{2} < k_F$ and $k_F - \frac{K}{2} < q < \sqrt{k_F^2 - \frac{K^2}{4}}$, one sees that the statistical effect of finite-temperature on these 2p properties in the important case of zero center of mass

momentum and Ω near 2μ is similar to the Pauli blocking effect at zero temperature and $(\frac{K}{2})^2 \sim mk_BT$. This effect contributes to the weakening of the imaginary part of the effective interaction near 2μ, as illustrated in Fig. 6.5. This figure displays the diagonal elements of the imaginary part of the resulting finite temperature effective interaction for zero center of mass momentum. The figure includes all partial waves which results in a q-independent high-Ω peak. This in turn is responsible for the k-independent high-energy behavior of the self energy. The decrease in over-all magnitude of the imaginary part of the effective interaction with respect to the zero-temperature case at low energies will yield a corresponding decrease of the imaginary part of the self-energy. This effect is illustrated in fig. 6.6. A direct comparison with Fig. 4.12 of Im Γ would be trivial, since the quantity vanishes at $\Omega = 2\mu$ at finite temperature. For comparison, an energy is chosen far from 2μ with respect to the temperature. The general decrease in magnitude of the finite temperature case is apparent. The top part of Fig. 6.6 shows that the main part of the difference does not occur in the S wave contribution. In the bottom half of the figure, one notices that after the inclusion of the higher waves, the general reduction becomes visible.

6.3 Self-Energy

The change to finite temperature has a significant overall effect on the imaginary part of the self-energy. With increasing temperature, the imaginary part of the self-energy is generally more washed-out than in the zero-temperature case, as documented in Ref. [86]. This is evident in the non-zero value of the the imaginary part of the self-energy at the chemical potential and the decrease in magnitude of the neighboring low-energy peaks, shown in Fig. 6.7. This is a reflection of the decrease in magnitude of the imaginary part of the effective interaction documented in the previous section.

Even for a temperature of 5 MeV, the greater smoothness of the self-energy will have important consequences for the sp spectral functions. For instance, we can

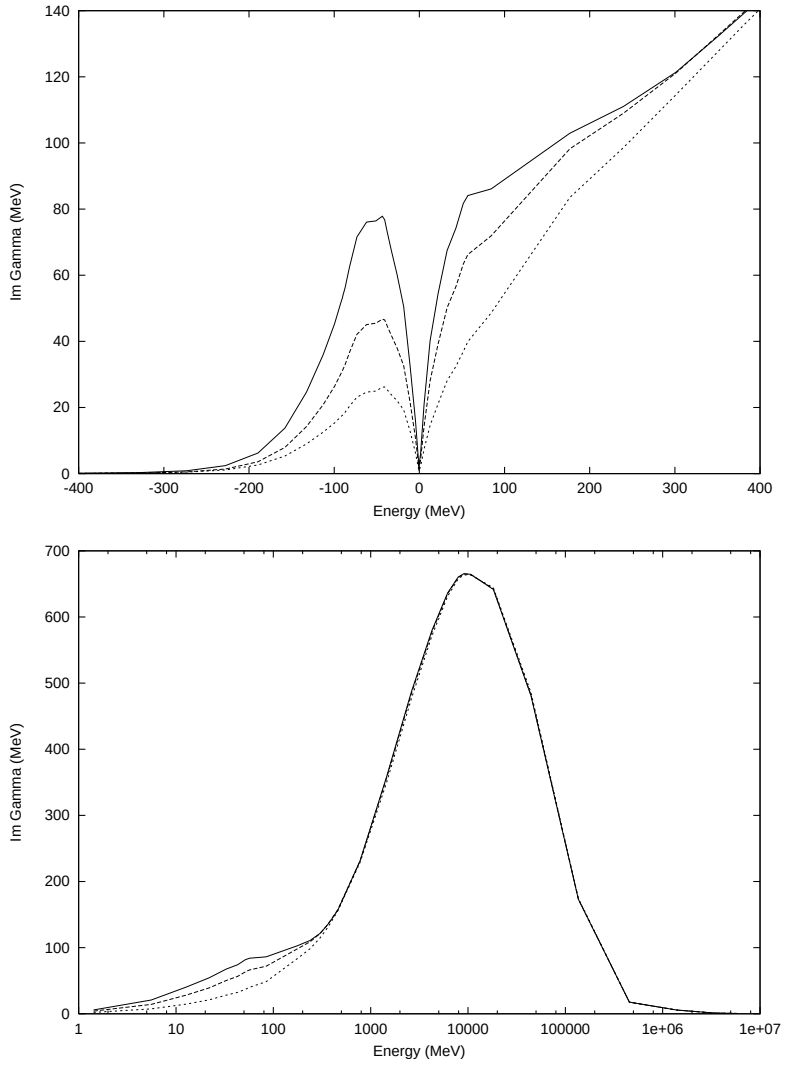

Figure 6.5: Imaginary part of the effective interaction, $\mathrm{Im}\,\Gamma(\Omega - 2\mu)$, is shown as a function of energy for total momentum, $K = 0$, and relative momentum, $q = \{0, 0.7, 1.36\ \mathrm{fm}^{-1}\}$.

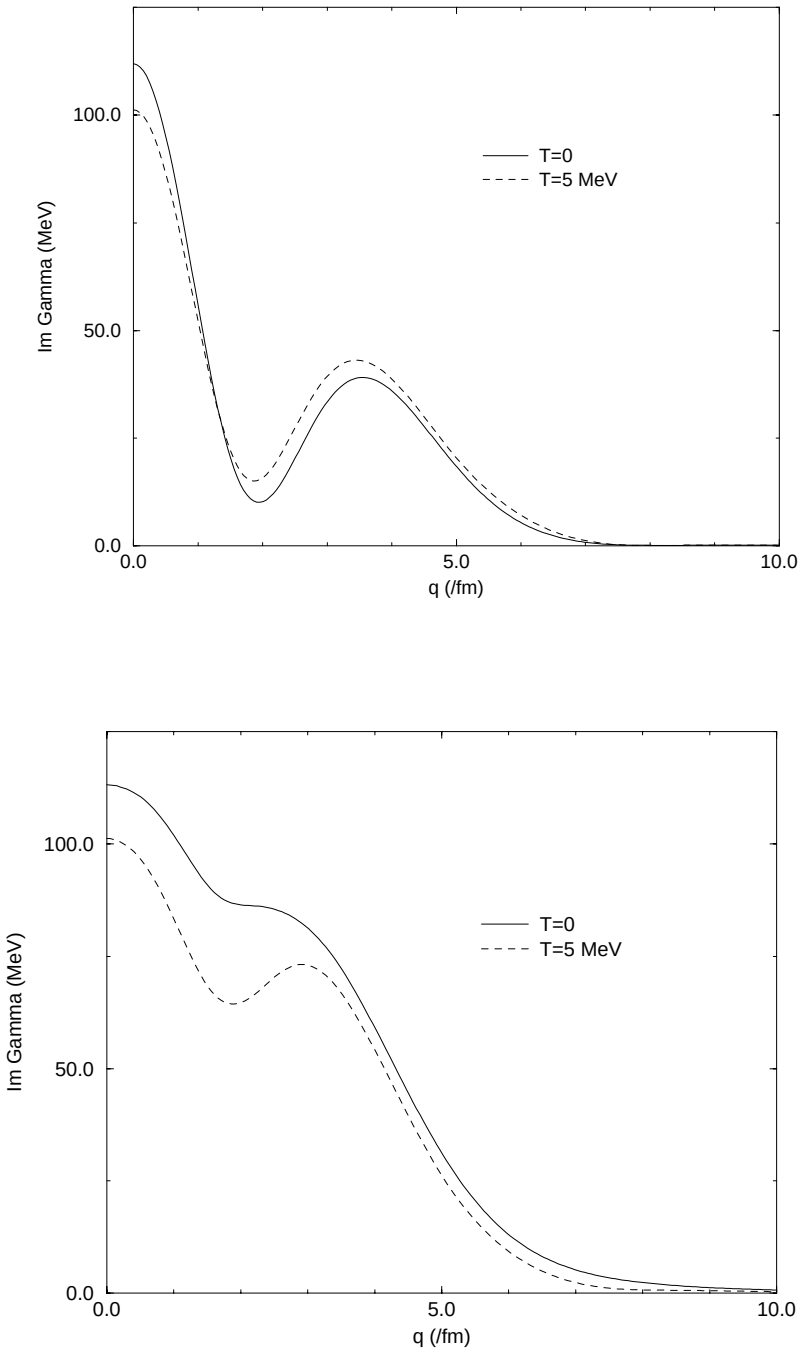

Figure 6.6: Comparison of $\mathrm{Im}\,\Gamma(q)$ for $K = 0$ and $\Omega = (2\mu + 75\ \mathrm{MeV})$, where the first plot includes only S waves and the second plot includes all partial waves.

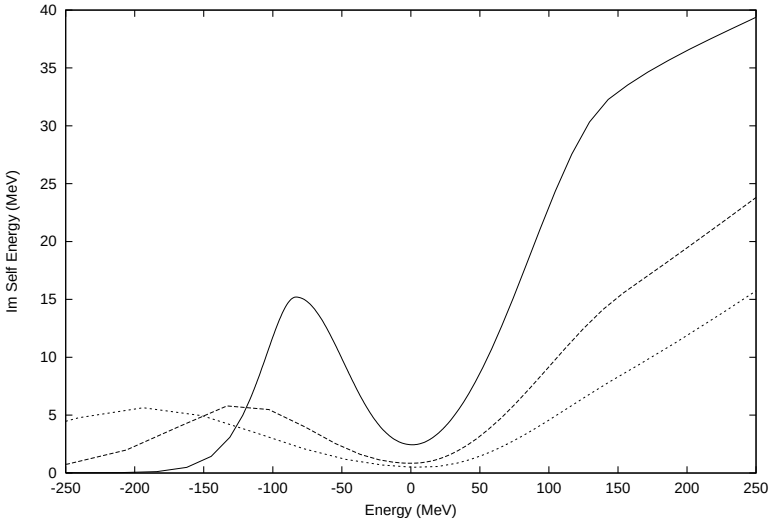

Figure 6.7: Im $\Sigma(\omega - \mu)$ is shown as a function of energy for selected single-particle momenta, $k = \{0$ (solid),1.36 (dashed), and 2.1 (dotted) fm$^{-1}\}$.

consider the characteristics of the quasiparticle peak as determined from the self-energy. The spectrum shown in Fig. 6.2 is little altered with respect to the zero-temperature case. The general decrease in the imaginary part of the self-energy will cause a corresponding decrease in the on-shell imaginary part (I), resulting in sharper quasiparticle peaks. The increased smoothness of the imaginary part of the self-energy will also result in less structure in Re Σ. Finally, the quasiparticle strength, z, related to the derivative of the real part of the self-energy becomes closer to 1.

These considerations suggest that the effect of the interaction is somewhat less important at finite temperatures. However, the spectral function contains a low-energy tail which develops in the self-consistent solution similar to the zero-temperature case. Again, the behavior of this tail at high momenta is a reflection the effect of SRC, as discussed in Chapter 4.

6.4 Spectral Function

Using the self-energy discussed above, sp properties can most easily be illustrated in the spectral function, which is shown for several sp momenta in Fig. 6.8. In the top part of this figure, the results near the chemical potential confirm the intuitive expectation that increasing the temperature will decrease the effect of the interaction on the spectral function. For instance, comparing 6.7 with the zero-temperature case, the decreased Im Σ near the chemical potential results in less spreading of the qp peaks. This decreased width of the qp peaks does not include the Fermi momentum, since the Im Σ is nonzero at the chemical potential, unlike the zero-temperature case. The resulting propagator is therefore more mean-field-like, with more sp strength located in a narrower peak. For example, for $k = k_F$, $z = 0.85$ in the finite-temperature case as compared with 0.80 at zero temperature. Averaging over the ensemble of states results in this change, since the statistical factor decreases the non-interacting 2p density of states. This, in turn, leads to the decreased imaginary part of the self-energy and decreased width of sp momentum states. The bottom part of the figure shows that the high-energy tail remains unaltered and shows no momentum or temperature independence.

As shown in Fig. 6.9, the non-zero value of the imaginary part of the self-energy at the chemical potential and its smoother behavior as a function of energy with respect to the zero-temperature case generate a spectral function that can be well described numerically for all momenta and energies. This implies that the value of the spectral function at any energy and momentum can be found with great accuracy upon interpolation. This contrasts with the zero-temperature case in which the spectral function has divergent peaks for momenta near k_F and sharp zeros at ε_F for all momenta, making finite-temperature calculations, even at $T = 5$ MeV, much less numerically demanding than at $T = 0$.

Finally, the occupation of momentum states is presented in Fig. 6.10 for comparison with the zero-temperature case (See Fig. 4.3) and with other finite-temperature

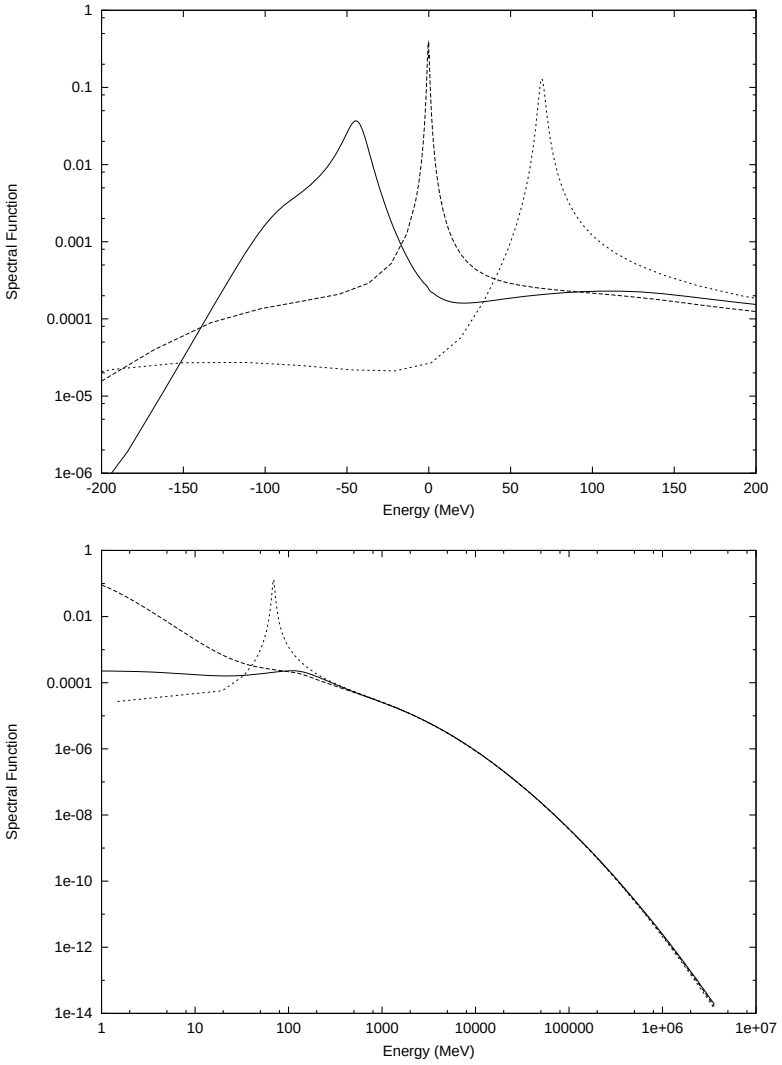

Figure 6.8: Single-particle spectral functions as a function of $\omega - \mu$ at low energy (top) and high energy (bottom) for $k = \{0$ (solid), 1.36 (dashed), 2.1 fm^{-1} (short$-$dashed)$\}$ for $k_F = 1.36$ fm^{-1} and $T = 5$ MeV.

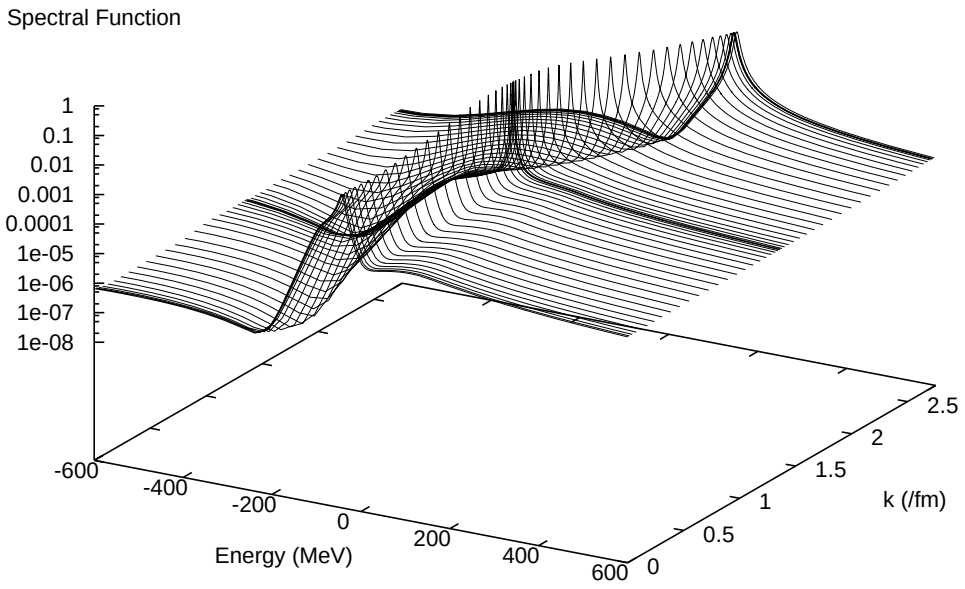

Figure 6.9: Single-particle spectral function, $S(k, \omega - \mu)$. Shown for comparison with zero-temperature case, Fig. 4.18.

work. The present result basically agrees with the results of Ref. [86], employing a separable version of the Paris potential. Such a similarity was also observed by Vonderfecht for the zero-temperature case [39]. This similarity is obtained despite the fact that different interactions are used which result in large differences at the Hartree-Fock level.

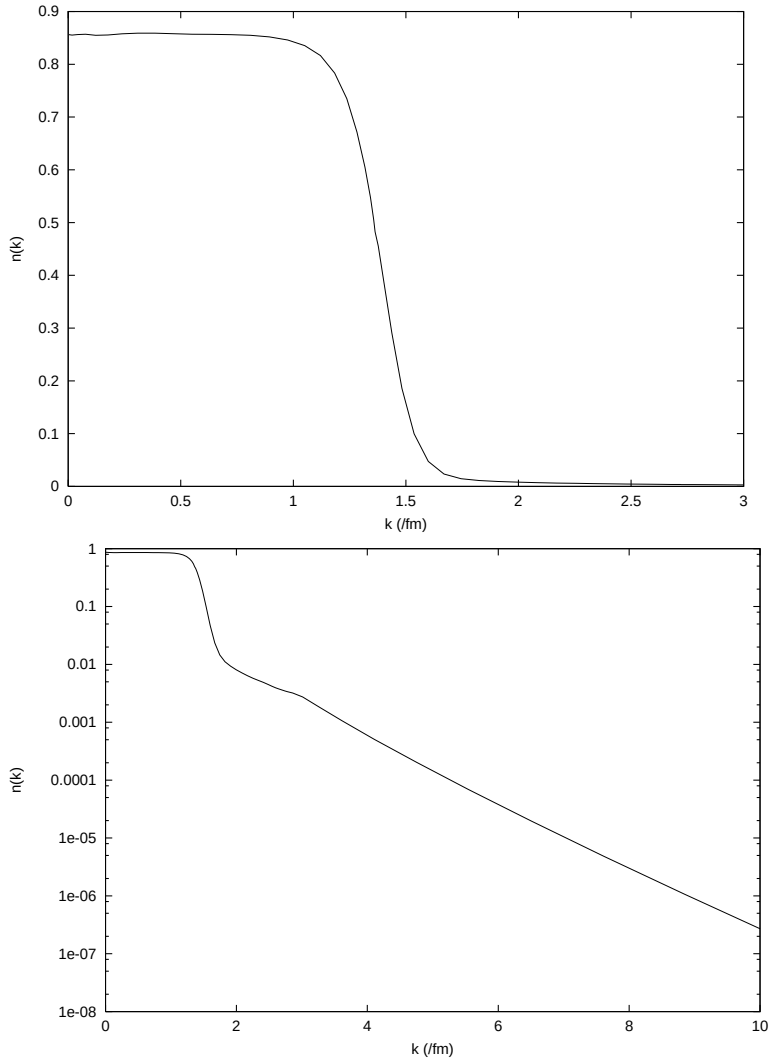

Figure 6.10: The self-consistent momentum distribution for low momenta (top) and for higher momenta on a logarithmic scale (bottom) at $k_F = 1.36$ fm^{-1} and $T = 5$ MeV.

Chapter 7

Conclusions and Outlook

Experimental evidence from (e,e′p) reactions clearly documents that sp states in nuclei exhibit fragmentation and partial occupation. To describe these results theoretically, an extension of the sp description from the independent-particle model is required. In most previous work, one describes this correlated sp strength distribution by calculating effects of excitations on a sea of mean-field particles. The aim of this work has been to use a Green's function many-body method to describe the propagation of a nucleon in infinite nuclear matter self-consistently including a realistic two-body interaction.

The sp Green's function yields sp expectation values, including the kinetic energy, and, in the case of a two-body interaction, the potential energy. Given a physically relevant approximation to the self-energy, the sp propagator must be solved self-consistently. To study the influence of this self-consistency on nuclear saturation, infinite nuclear matter is chosen. A realistic NN interaction contains a strong short-range repulsion, which is considered to be a primary source of the observed fragmentation and depletion of sp strength. To include the effect of SRC, the Brueckner ladder approximation must be applied to describe the effective interaction in the medium. In all previous work, mean-field sp propagators have been employed to describe 2p propagation between successive interactions. In this work, correlated sp propagators, including complete off-shell energy-dependence, are used to solve the ladder approximation, as first performed by Gearhart. In this thesis, for the first time, self-consistency of the sp propagator has been achieved via successive solution of the ladder equation and the corresponding Dyson equation at $k_F = 1.36$ fm^{-1} and 1.45 fm^{-1}, using the Reid soft-core interaction.

Additionally, one can intuitively expect that a description of single-particle states which includes the effects of SRC self-consistently may affect calculated sp properties. The iteration to self-consistency is required to obtain the low-energy contributions which arise at $k > k_F$. These contributions differ from those calculated from a mean-field starting point and play a crucial role in saturation (See Chapter 4).

A goal of this thesis has been to compare self-consistent propagators including SRC with their counterparts calculated from the mean-field approximation. To study the effect of the self-consistent inclusion of SRCs on sp propagation, one can consider the resulting spectral functions. In general, the structure of the self-consistent spectral function is not drastically different from one obtained with mean-field propagators. The region exhibiting the greatest difference corresponds to low momentum and large negative energy. The spectral function vanishes in this region when mean-field phase-space considerations are included. In the self-consistent case, the spectral function in this region forms a weakly k-dependent low energy tail, not unlike the high-energy behavior which displays no momentum dependence. This result is a reflection of the coupling of the nucleon to 2h-1p states that are themselves spread in the self-consistent treatment. This low-energy tail of the self-consistent spectral function is also of crucial importance in determining the saturation properties. Differences in the spectral function for the self-consistent and mean-field treatments in this region are subtle but have an important influence on saturation properties. For this reason, it is necessary to consider self-consistent propagators in calculating the effect of SRC on saturation.

We have found that the impact of self-consistency of sp propagators is profound for saturation properties. This project has resulted in a theoretical prediction of nuclear saturation properties which do not lie on the Coester band and are moved close to empirical values. This increased binding at lower density arises from the low-energy tail resulting from multiple iteration of the propagator. These components serve as an important source of binding for momenta as high as 5 fm^{-1}. Therefore, including the short-range NN interaction self-consistently, an accurate description of

nuclear saturation properties can be attained including only two-body interaction terms. The present result is not inconsistent with recent three hole-line calculations if one is willing to exclude the contributions of long-range correlations. It has been suggested in Chapter 4 that the long-range correlations determined in nuclear matter, especially those including pion-exchange terms, may not be necessary to describe atomic nuclei.

In order to study neutron matter, however, the ladder approximation may not provide a complete description since the effect of collective excitations is not included. A practical method to include such diagrams self-consistently remains to be developed.

The next development for this project will be to extend self-consistency beyond the S wave level. Including higher waves self-consistently requires some development of the numerical treatment of the iteration scheme, but no change in the theoretical formulation of the problem will be required. This extension is necessary before a final statement about self-consistent results in nuclear matter and saturation can be made.

In applying self-consistent propagators to describe other properties which may be compared with experiment, there are many important avenues to pursue:

1. Applying SCGF solutions as a function of density to be used in the calculation hadron tensors used in conjunction with the local density approximation to describe knockout experiments.

2. The study of two-body density matrices in interacting systems for use in calculating 2p expectation values, including inclusive scattering and exclusive cross-sections for triple coincidence experiments.

3. An extension to different potentials on the market. This extension should pose little additional difficulty since the more modern potentials [93]-[97] have softer cores than the Reid potential used in this work.

These calculations can be extended to determine thermodynamic characteristics of nuclear matter with different potentials. Utilizing the SCGF equations for various temperatures, properties of hot nuclear matter due to SRC can be studied. These results have application to transport studies of heavy ion collisions. Another topic of

interest is the effect of treating SRC self-consistently on phase changes. Since dressed propagators including the SRCs drastically alter the appearance of the superfluid phase transition at saturation density [43], the presence and onset of the liquid-gas phase transition may also be affected. Included in this thesis is the ground work and a pilot calculation applying SCGF methodology in finite-temperature nuclear matter. This serves as a starting point for the study of the temperature and density dependence of the sp SCGF spectral function.

Bibliography

[1] H.A. Bethe, Phys. Rev. 103 (1956) 1353.

[2] C.F. von Weizsacker, Z. Phys. 96 (1935) 431.

[3] A. Bohr and B.R. Mottelson, Nuclear Structure, Vol. I (W.A. Benjamin, New York,1969).

[4] B. Frois et al, Phys. Rev. Lett. 38 (1977) 152.

[5] V.M. Galitskii and A.B. Migdal, Sov. Phys. -JETP, 7 (1958) 96.

[6] A. Akmal, V.R. Pandharipande, and D.G. Ravenhall, Phys. Rev. C 58 (1998) 1668.

[7] K.A. Brueckner, C.A. Levinson and H.M. Mahmoud, Phys. Rev. 95 (1954) 217.

[8] K.A. Brueckner and C.A. Levinson, Phys. Rev. 97 (1955) 1344.

[9] K.A. Brueckner, Phys. Rev. 97 (1955) 1353.

[10] K.A. Brueckner, Phys. Rev. 103 (1956) 172.

[11] H. Kummel, K.H. Luhrmann and J.G. Zabolitzky, Phys. Rep. C 36 (1978) 1.

[12] J.W. Clark, Nucl. Phys. A 328 (1979) 587.

[13] F. Coester, S. Cohen, B. Day and C.M. Vincent, Phys. Rev. C1 (1970) 769.

[14] B.D. Day, Phys. Rev. C 24 (1981) 1203.

[15] B.D. Day and R.B. Wiringa, Phys. Rev. C 32 (1985) 1057.

[16] J. Carlson, V.R. Pandharipande and R.B. Wiringa, Nucl. Phys. A401 (1983) 59.

[17] C.J. Horowitz and B.D. Serot, Phys. Lett. B138 (1984) 287.

[18] R. Brockman and R. Machleidt, Phys. Rev. C 42 (1990) 1965.

[19] S.C. Pieper and V.R. Pandharipande, Phys. Rev. Lett. 70 (1993) 2541.

[20] J.P. Jeukenne, A. Lejeunne, and C. Mahaux, Phys. Rep. 25 C (1976) 83.

[21] H.Q. Song, M. Baldo, G. Giansiracusa, and U. Lombardo, Phys. Rev. Lett. 81 (1998) 1584.

[22] H.Q. Song, M. Baldo, G. Giansiracusa, and U. Lombardo, Phys. Lett. B 411 (1997) 237.

[23] W.H. Dickhoff, A. Faessler, and H. Müther, Nucl. Phys. A 389 (1982) 492.

[24] E.N.M. Quint et al., Phys. Rev. Lett. 58 (1987) 1088.

[25] C. Cioffi degli Atti, in The Nuclear Many-Body Problem III, eds. F. Calogero and C. Ciofi degli Atti (Editrice Compositori, Bologna,1972) 365.

[26] A. Ramos, A. Polls and W.H. Dickhoff, Nucl. Phys. A503 (1989) 1.

[27] W.H. Dickhoff, Phys. Lett. B210 (1988) 15.

[28] P.K.A. de Witt Huberts, J. Phys. G: Nuc. Part. Phys. 16 (1990) 507.

[29] A.E.L. Dieperink and P.K.A. de Witt Huberts, Ann. Rev. Nucl. Part. Sci. 40 (1990) 239.

[30] L.D. Landau, Soviet Phys. 3 (1957) 920.

[31] L.D. Landau, Soviet Phys. 5 (1957) 101.

[32] L.D. Landau, Soviet Phys. 8 (1958) 70.

[33] A.B. Migdal, Nuclear Theory: The Quasiparticle Method (Benjamin, New York, 1968).

[34] O. Benhar and A. Fabrocini, and S. Fantoni, Nucl. Phys. A 505 (1989) 267.

[35] H.S. Köhler, Nucl. Phys. A537 (1992) 64.

[36] M. Baldo, I. Bombaci, G. Giansiracusa, U. Lombardo, C. Mahaux and R. Sartor, Nucl. Phys. A545 (1992) 741.

[37] L.P. Kadanoff and G. Baym, Quantum Statistical Mechanics (Benjamin, Menlo Park, 1962)

[38] A. Ramos, Ph.D. Thesis, 1988, University of Barcelona (unpublished).

[39] B.E. Vonderfecht, W.H. Dickhoff, A. Polls, and A. Ramos, Phys. Rev. C 44 (1991) R1265.

[40] B.E. Vonderfecht, Ph.D. Thesis, 1991, Washington University (unpublished).

[41] C.C. Gearhart, Ph.D. Thesis, 1994, Washington University (unpublished).

[42] C.C. Gearhart, W.H. Dickhoff, A. Polls, and A. Ramos, Int. J. Mod. Phys. E 5 (1996) 461.

[43] W.H. Dickhoff, C.C. Gearhart, E.P. Roth, A. Polls, and A. Ramos, Phys. Rev. C 60 (1999) 064319.

[44] A. Polls, A. Ramos, J. Ventura, S. Amari, and W. H. Dickhoff, Phys. Rev. C 49 (1994) 3050.

[45] R. Starink, et al, Phys. Lett. B 474 (2000) 33.

[46] O. Benhar, A. Fabrocini and S. Fantoni, Nucl. Phys. A505 (1989) 267.

[47] W. Kraeft, D. Kremp, W. Ebeling and G. Röpke, Quantum Statistics of Charged Particle Systems (Plenum Press, 1986).

[48] A. Schnell, T. Alm, and G. Röpke, Phys. Lett. B387 (1996) 443

[49] R.V. Reid, Ann. Phys. 50 (1968) 411.

[50] A.A. Abrikosov, L.P. Gorkov and I.E. Dzyaloshinski, *Methods in Quantum Field Theory and Statistical Physics* (Dover, 1975).

[51] G.E. Brown, Many-Body Problems (North Holland, Amsterdam, 1972).

[52] A.L. Fetter and J.D. Walecka, Quantum Theory of Many-Particle Systems (McGraw-Hill, 1971).

[53] L.P. Kadanoff and G. Baym, Quantum Statistical Mechanics (Benjamin, New York, 1962).

[54] R. D. Mattuck, A Guide to Feynman Diagrams in the Many-Body Problem (Dover, 1992).

[55] H. Lehmann, Nuovo Cimento 11 (1954) 342.

[56] D.S. Koltun, Phys. Rev. Lett. 28 (1972) 182.

[57] D.S. Koltun, Phys. Rev C9 (1974) 484.

[58] F.J. Dyson, Phys. Rev. 75 (1949) 486.

[59] P.C. Martin and J. Schwinger, Phys. Rev. 115 (1959) 1342.

[60] G. Baym and L.P. Kadanoff, Phys. Rev. 124 (1961) 287.

[61] J. J. Sakurai, *Modern Quantum Mechanics* (Addison-Wesley, 1994).

[62] V.M. Galitskii, Sov. Phys. JETP 7 (1958) 104.

[63] Y. Dewulf, thesis University of Gent, 2000.

[64] P. Bożek, Nucl. Phys. A657 (1999) 187.

[65] F. de Jong and H. Lenske, Phys. Rev. C56 (1997) 2619.

[66] J. Lehr, et al, Phys. Lett. B 483 (2000) 324.

[67] C. Cioffi degli Atti, S. Liuti, and S. Simula, Phys. Rev. C 49 (1990) R2474.

[68] M.I. Haftel and F. Tabakin, Nucl. Phys. A158 (1970) 1.

[69] A. Polls, H. Müther, and W.H. Dickhoff, Nucl. Phys. A 594 (1995) 117.

[70] K.A. Brueckner and J.L. Gammel, Phys. Rev. 117 (1960) 207.

[71] E. Schiller, H. Müther, and C. Czerski, Phys. Rev. C 59 (1999) 2934, Phys. Rev. C 60 (1999) 059901.

[72] K. Suzuki, R. Okamoto, M. Kohno, S. Nagata, Nucl. Phys. A 665 (2000) 92.

[73] F. Sammarruca, X. Meng, and E.J. Stephenson, Phys. Rev. C 62 (2000) 014614.

[74] B.E. Vonderfecht, C.C. Gearhart, W.H. Dickhoff, A. Polls, A. Ramos, Phys. Lett. B 253 (1991) 1.

[75] N.M. Hugenholtz and L. Van Hove, Physica 24 (1958) 363.

[76] M. Baldo, I. Bombaci, G. Giansiracusa, and U. Lombardo, Phys. Rev. C 41 (1990) 1748.

[77] C.C. Gearhart, W.H. Dickhoff, A. Polls, and A. Ramos, J. of Mod. Phys. E 5 (1996) 461.

[78] P. Czerski, W.H. Dickhhoff, A. Faessler, and H. Müther, Phys. Rev. C 33 (1986) 1753.

[79] W. Kraeft, D. Kremp, W. Ebeling and G. Röpke, Quantum Statistics of Charged Particle Systems (Plenum Press, 1986).

[80] W.E. Parry, The Many-Body Problem (Clarendon Press, 1973).

[81] R. Kubo, J. Phys. Soc. Japan 12 (1957) 570.

[82] T. Matsubara, Prog. Theoret. Phys. 14 (1955) 351.

[83] L.D. Landau, Sov. Phys. JETP 7 (1958) 182.

[84] Michel Le Bellac, Thermal Field Theory (Cambridge, 1996)

[85] F. Bloch, Z. Physik, 74 (1932) 295.

[86] A. Schnell, Ph.D. Thesis, 1996, University of Rostock (unpublished).

[87] G. Röpke, L. Münchow, and H. Schulz, Nucl. Phys. A379 (1982) 536.

[88] A. Lejeune, P. Grange, M. Martzolff, and J. Cugnon, Nucl. Phys. A453 (1986) 189.

[89] P. Grange, J. Cugnon, and A. Lejeune, Nucl. Phys. A473 (1987) 365.

[90] H.S. Köhler, Nucl. Phys. A 537 (1992) 64.

[91] M. Schmidt, G. Röpke, H. Schultz, Ann. Phys. 202 (1990) 57.

[92] T. Alm, G. Röpke, A. Schnell, N.H. Kwong, and H.S. Kohler, Phys. Rev. C 53 (1996) 2181.

[93] R.K. Su, S.D. Yang, and T.T.S. Kuo, Phys. Rev. C 35 (1987) 1539. A.D. Panagiotou, M.V. Curtin, H. Toki, D.K. Scott, and P.J. Siemens, Phys. Rev. Lett. 52 (1984) 496.

[94] R. B. Wiringa, V. G. J. Stoks, and R. Schiavilla, Phys. Rev. C 51 (1995) 38.

[95] V. G. J. Stoks, R. A. M. Klomp, C. P. F. Terhaggen, and J. J. de Swart, Phys. Rev. C 49 (1994) 2950.

[96] R. Machleidt, K. Holinde, and Ch. Elster, Phys. Rep. 149 (1987) 1.

[97] M. Lacombe, B. Loiseau, J.M. Richard, R. Vinh Mau, J. Pires, and R. Tourreil, Phys. Rev. C 21 (1980) 861.